


1-1-2017

Development Of A Finite Element Pelvis And Lower Extremity Model With Growth Plates For Pediatric Pedestrian Protection

Ming Shen
Wayne State University,

Follow this and additional works at: http://digitalcommons.wayne.edu/oa_dissertations

 Part of the [Biomechanics Commons](#), [Biomedical Engineering and Bioengineering Commons](#), and the [Other Mechanical Engineering Commons](#)

Recommended Citation

Shen, Ming, "Development Of A Finite Element Pelvis And Lower Extremity Model With Growth Plates For Pediatric Pedestrian Protection" (2017). *Wayne State University Dissertations*. 1876.
http://digitalcommons.wayne.edu/oa_dissertations/1876

This Open Access Dissertation is brought to you for free and open access by DigitalCommons@WayneState. It has been accepted for inclusion in Wayne State University Dissertations by an authorized administrator of DigitalCommons@WayneState.

**DEVELOPMENT OF A FINITE ELEMENT PELVIS AND LOWER EXTREMITY MODEL
WITH GROWTH PLATES FOR PEDIATRIC PEDESTRIAN PROTECTION**

by

MING SHEN

DISSERTATION

Submitted to the Graduate School

of Wayne State University,

Detroit, Michigan

in partial fulfillment of the requirements

for the degree of

DOCTOR OF PHILOSOPHY

2017

MAJOR: BIOMEDICAL ENGINEERING

Approved By:

Advisor

Date

© COPYRIGHT BY

MING SHEN

2017

All Rights Reserved

DEDICATION

This dissertation is dedicated to

My wife, Ying Lian,

My Parents,

And

My kids, Mia and Ellie

For their inspirations,

and unconditional loves and supports

ACKNOWLEDGEMENTS

I am deeply grateful to my advisor, Dr. King H. Yang, for leading me into this interesting and challenging research field, and for his encouragement and guidance throughout my Ph.D. study. I do appreciate Dr. Clifford C. Chou for his continuous inspiration and support on my road to finish this dissertation. I also cordially thank Dr. Albert I. King for the various mentoring and support. I would like to express my gratitude to Drs. John M. Cavanaugh, and Jonathan D. Rupp for the valuable comments and suggestions they devoted to my dissertation.

Further, I sincerely appreciate Drs. Haojie Mao, Feng Zhu, and Xin Jin for the guidance and constructive advices during their postdoctoral fellowship in WSU. I heartily thank Drs. Shengxiong Liu and Paul C. Begeman for their assistances on the experiment conduction. I extend my appreciations to all the fellow Ph.D. students (especially Runzhou, Anil, Tal, Ke), and the visiting scholars (especially Binhui, Liqiang, Haiyan) for the valuable ideas from the academic collisions. My thanks also go to former master students involved in this study, namely Haonan, Nikhil, Yun, Zhengguang, Ian, Harikrishna, Vikas, and so on. Moreover, I must recognize the staff of the department of Biomedical Engineering, WSU.

I also express the warmest gratitude to Prof. Jinhuan Zhang (Tsinghua University) and Dr. Jingwen Hu (University of Michigan) for their guidance ever since the years in Tsinghua University. They have encouraged me to keep aiming higher.

I would like to acknowledge Toyota's Collaborative Safety Research Center, North America, for their funds towards the CHARM-10 models development, and the International Center for

Automotive Medicine, University of Michigan, for providing the anthropometric measurements and clinical images for this study.

Mostly importantly, I am so indebted to my family. They have contributed and sacrificed so much in these years and deserve to accept my dedication of the whole dissertation. They are my essential source of motivations to get here and move forward.

TABLE OF CONTENTS

DEDICATION	ii
ACKNOWLEDGEMENTS	iii
LIST OF TABLES	ix
LIST OF FIGURES	xi
CHAPTER 1. INTRODUCTIONS	1
CHAPTER 2. EPIDEMIOLOGIC REVIEW	7
2.1. Pediatric pedestrian accident.....	7
2.2. Growth plate traumatic injury	13
CHAPTER 3. RESEARCH TOOLS FOR PEDESTRIAN PROTECTION	18
CHAPTER 4. BASELINE PLEX FE MODEL DEVELOPMENT	23
4.1. Geometric and anthropometric study	23
4.2. Mesh generation and model Integration.....	26
4.3. PLEX baseline model validation.....	27
4.3.1. Validation overview	28
4.3.2. Scaling laws for model validation	30
4.3.3. Validation summary	34
4.3.4. Material properties of PLEX	42
4.4. Chapter summary	44
CHAPTER 5. LITERATURE REVIEW OF GROWTH PLATE	45

5.1.	Growth plate anatomy	45
5.2.	Growth plate experimental studies.....	50
5.2.1.	Tensile tests.....	50
5.2.2.	Shearing tests.....	52
5.2.3.	Compressive tests	55
5.2.4.	Summary of GP tests	57
5.3.	Growth plate FE modeling studies in literature	58
CHAPTER 6. GROWTH PLATE EXPERIMENTAL STUDY		61
6.1.	Methods.....	61
6.1.1.	Test subject selection	61
6.1.2.	Specimen preparation and measuring.....	63
6.1.3.	Experimental design	67
6.1.4.	Test setup and instrumentation	69
6.1.5.	Selection of stress – strain scales.....	74
6.1.6.	Data acquisition and processing	77
6.1.7.	Human-porcine GP correlation.....	79
6.1.8.	Statistical analysis.....	81
6.2.	Results.....	82
6.2.1.	Test results overview	82
6.2.2.	ANOVA results	85

6.3.	Human-Porcine GP correlation result	91
6.4.	Estimated 10 YO human GP properties	94
6.5.	Chapter discussions.....	96
6.5.1.	Loading rate selection.....	96
6.6.	Chapter summary	98
CHAPTER 7. HUMAN GROWTH PLATE MODELING AND PARAMETRIC STUDY....		
.....		101
7.1.	10 YO human GP material modeling	101
7.1.1.	Material model selection	101
7.1.2.	Material law and parameters.....	103
7.1.3.	Specimen tension and shearing simulation.....	105
7.1.4.	Optimization processes.....	107
7.1.5.	Material modeling results	113
7.2.	Modeling of proximal femur with GPs	116
7.2.1.	GP model generation	116
7.2.2.	Parametric study in shearing load.....	119
7.3.	Whole-body pedestrian model with GPs in the PLEX.....	124
7.3.1.	GP closure age examination	125
7.3.2.	PLEX model updated with GPs.....	125
7.3.3.	Pedestrian impact simulation results	129
7.4.	Chapter discussions.....	134

7.4.1. Mesh convergence of the specimen FE model	134
7.4.2. Material axis	136
7.4.3. Strain rates measured from whole-body pedestrian simulation.....	137
7.5. Chapter summary	139
CHAPTER 8. LIMITATION AND FUTURE WORK	141
8.1. Limitations	141
8.2. Future work.....	144
CHAPTER 9. CONCLUSIONS.....	148
REFERENCES.....	152
ABSTRACT	169
AUTOBIOGRAPHICAL STATEMENT	172

LIST OF TABLES

Table 2-1: Top ten priorities of pediatric pedestrian injury mitigation with social cost percentages compared with adults' (Fildes et al., 2004)	12
Table 2-2: The injury frequency distribution among GPs, later than 1970's (Peterson, 2007)	14
Table 2-3: The incidence rate of pelvic fractures and acetabular fracture for children and adults (Von Heyden et al., 2012)	17
Table 4-1: Anthropometric study summary.....	24
Table 4-2: Loading conditions and scaling methods for model validation	29
Table 4-3: Formulas for impact response transformation ratios (Irwin et al., 2002)	30
Table 4-4: Subjects information and scaling of test results, originally reported by Ouyang et al. (2003a)	34
Table 4-5: Scaling of adult results for 10 YO model validation	38
Table 4-6: Car-to-pedestrian impact simulations using MADYMO dummy model (scaled from adult pedestrian model to 10 YO), published as (Shen et al., 2015a)	41
Table 4-7: Main material properties of 10 YO PLEX FE model, with the relevant references given accordingly.....	43
Table 6-1: Calculations of various dimensions measured on each specimen	67
Table 6-2: The numbers of specimens tested in tension.....	68
Table 6-3: The numbers of specimens tested in shear loading.....	69
Table 6-4: actual strain rates in tensile and shearing tests	82
Table 6-5: P values calculated using the Randomized-block ANOVA on the three tensile and three shearing mechanical properties	85
Table 6-6: Mechanical properties of GPs in tensile and shearing tests at different strain rates....	86

Table 6-7: Mechanical properties of GPs in tensile and shearing tests at different anatomic regions	87
Table 6-8: Comparison of the human and porcine tensile properties on the femoral head GP	92
Table 6-9: Comparison of the loading speeds/rates of current study and literatures	96
Table 7-1: Loading conditions of generic FE model representing the corresponding experiments on the femoral head GP specimens	106
Table 7-2: Initial ranges of parameters in the 1 st stage of optimization for 10 YO femoral head GP	109
Table 7-3: Initial ranges of parameters in the 2 nd stage of optimization for the femoral head GP of a 10 YO Child	110
Table 7-4: Initial ranges of parameters in both 1 st and 2 nd stages of optimization for the knee GP of a 10 YO child	113
Table 7-5: MAT_92 parameters for the femoral head GP of a YO child	113
Table 7-6: MAT_92 parameters for the knee GP's of 10 a YO child.....	115
Table 7-7: Material properties of the major components in the upgraded proximal femur FE model of PLEX model	122
Table 7-8: Simulation results compared to the test results by Chung et al., 1976	123
Table 7-9: Closure ages of the GPs in the PLEX	125
Table 7-10: The maximum 1 st Principal strain rates at the GPs in the PLEX in SUV-to-pedestrian impact simulation (5.0 m/s)	138

LIST OF FIGURES

Figure 1-1: Pedestrian fatalities among children aged 14 and younger, by age group, 2002-2011 (NHTSA, 2013).....	2
Figure 1-2: The X-ray image of knee with GPs gaps between epiphysis and metaphysis, because non-ossified GPs are radiolucent in X-ray (by Danna 2011, obtained from https://thesebonesofmine.wordpress.com/category/femur).....	3
Figure 2-1: Age distribution of two pedestrian data analysis studies initiated by NHTSA (PICS and PCDS). Re-drawn from the original plot in Jarrett and Saul (1998).....	8
Figure 2-2: Pedestrian injury distribution based on PCDS database. (a) all injuries (Chidester and Isenberg, 2001); (b) injury for AIS \geq 2 (Kikuchi et al., 2006).....	9
Figure 2-3: Pedestrian injury distribution for children. (a) with at least one AIS 2+ injury; (b) with at least one AIS 3+ injury (Ivarsson et al., 2006). The injury percentages for spine (lumbar or thoracic) and neck (including cervical spine) did not exceed 2% for all age groups in two frequency investigations, therefore not shown in both figures	10
Figure 2-4: Distribution of pedestrian injuries (AIS 2+) at pelvis and lower extremity. (a) for all age groups (Kikuchi et al., 2006); (b) for children (Ivarsson et al., 2006)	10
Figure 2-5: Locations of bumper impacting on the lower limb and the head impacting on the hood or windshield for pedestrians with different ages (Serre et al., 2010)	12
Figure 2-6: Distribution of GP injuries drawn based on the data in Table 2-2 by Peterson (2007). (a) Overall distribution; (b) Distribution at three long bones of the lower extremities	15
Figure 2-7: Salter-Harris epiphyseal fracture classification (Salter and Harris, 1963).....	15
Figure 2-8: The fractions of fracture happening to different pelvic locations for immature (lighter bars) and mature (darker bars) pelvic groups (Silber and Flynn, 2002)	17
Figure 4-1: Dimension comparison between measurement and 10 YO model for femur (a) and tibia (b). "Proximal" refers to the cross section 20 mm distal/below the less trochanter. "2/3" refers to the cross section lower/distal from the tibia condyle by 2/3 of the bone length.....	25

Figure 4-2: Overview of the geometric data of 10 YO child. The CAD was extracted and segmented from clinical images by previous study represented as 3D surfaces. (a) Whole-body CAD with some skeleton exposed, (b) a closer view of the pelvic bones and cartilages (left half)..... 25

Figure 4-3: Mesh generation process: from clinical images to CAD surface, to blocks, to meshes (further refinement is not shown here)..... 26

Figure 4-4: Three key regions of the 10 YO PLEX FE model: (a) Knee region (capsule and part of flesh is hidden for better view); (b) Foot & ankle region; (c) Pelvis region (rear view with pelvic flesh and fat hidden)..... 27

Figure 4-5: The comparison of simulation results and prediction curve: (a) Ultimate bending force vs. cross-sectional dimension; (b) Ultimate bending force vs. span/sample length..... 33

Figure 4-6: Simulation results of 3-point bending tests on long bones, compared to scaled data from Ouyang et al. (2003a)..... 35

Figure 4-7: Pelvic ring lateral impact validation. (a) Simulation setup; (b) Simulation results compared with the experimental results originally from Guillemot et al. (1997)..... 36

Figure 4-8: MCL tensile test: (a) Simulation setup; (b) Corridor of adult MCL material property in a stress-strain plot, originally reported by Puso and Weiss (1998) 37

Figure 4-9: The validation thigh and shank: (a) & (b) Before loading; (c) & (d) After failure 38

Figure 4-10: Knee lateral-medial 4-point bending (a) Simulation setup; (b) Adult test results in bending moment - bending angle plot, originally from Bose et al. (2004)..... 39

Figure 4-11: Pelvis lateral impact (a) Simulation setup; (b) Corridor of experimental results of 5-12 YO children, originally from Ouyang et al. (2003b)..... 40

Figure 5-1: Growth plate anatomy. (a) Schematic diagram of distal femoral GP (Peterson, 2007); (b) Histological section picture of the femoral head from an 8 YO girl (Ogden, 2000)..... 46

Figure 5-2: Micro-graph of a 2 μm thick section of a rat proximal tibia GP (Villemure and Stokes, 2009) 47

Figure 5-3: Growth patterns of a typical long bone (A) the second ossification center (SCO) surrounded by a spherical physis, secondary physis (SP); (B) the second ossification center

expanded; (C) the second physis approached to primary physis and fuses to one (Peterson, 2007)	48
Figure 5-4: The closure ages of GPs in upper and lower extremities (Scheuer et al., 2000).....	48
Figure 5-5: GP at pelvis: Triradiate cartilage. (a) Schematic diagram (Peterson, 2007); (b) Detailed view of triradiate cartilage (fused with acetabular articular cartilage) (Bucholz et al., 1982).....	49
Figure 5-6: Tensile test setup examples. (a) Friction grips in Williams et al. (2001). (b) Complete setup in Cohen et al. (1992), including image tracking system	50
Figure 5-7: The Young's modulus of GP from tension tests. The references in order are (1) Cohen et al. (1992), (2) Williams et al. (2001), (3) Fujii et al. (2000).....	52
Figure 5-8: Ultimate tensile stress of GP. The references in order are: (1) Cohen et al. (1992), (2) Williams et al. (2001), (3) Fujii et al. (2000), (4) Guse et al. (1989), (5) Noble et al. (1982).....	52
Figure 5-9: Shearing test by Chung et al. (1976). (a) Experimental setup; (b) Failure patterns for different ages.....	53
Figure 5-10: Test set-up of shearing of bone-GP-bone unit from bovine proximal tibia (Williams et al., 1999)	55
Figure 5-11: Unconfined compression test of GP. (a) Test schematic. The specimen is a thin disc of only GP tissue bathed in Hank's balanced salt solution (HBSS); (b) Experimental stress relaxation time histories on the complete GP and 3 zones respectively. (Sergerie et al., 2009)...	56
Figure 6-1: Bone-GP-bone unit cutting descriptions. (a) Cutting equipment: a vertical band saw; (b) A schematic diagram of the fixture and guiding blocks used for cutting a distal femur into sagittal slices; (c) A schematic diagram showing how a parasagittal slice was held and cut; (d) A cut bone-GP-bone unit, i.e. a specimen	64
Figure 6-2: Specimen measurement: An anterior view of one specimen with a ruler positioned next to it	65
Figure 6-3: Porcine GP tensile test setup at the specimen aligning stage.....	70
Figure 6-4: Porcine GP shearing test setup. The right grip pair is adjustable along the long axis of the bone-GP-bone specimen to allow proper positioning of the test specimen; The left grip pair is rigidly mounted to the vertical actuator of the Instron.....	72

Figure 6-5: A typical engineering stress-strain curve from a GP tensile test. The calculation of the elastic modulus, ultimate stress, and ultimate strain were illustrated. Typically, there was a toe-in region followed by a larger linear segment. A decrease in slope, when the stress was approaching the ultimate point, was not always observed..... 78

Figure 6-6: GP thickness measurement results. A “*” marking indicates a significant difference ($p < 0.05$)..... 83

Figure 6-7: The effect of strain rate on tensile and shearing properties. The mean values are plotted as bars and the standard errors of the mean are also shown. A “ * ” marking indicates a significant difference 88

Figure 6-8: The effect of anatomic region on tensile and shearing properties. The mean values are plotted as bars and the standard errors of the mean are also showed. A “ * ” marking indicates a significant difference. (FMR HD: femoral head; Dist. FMR: distal femur; Prox. TBR: proximal tibia) 89

Figure 6-9: Relationship of the porcine femoral head GP engineering stress vs. finite strain. The average curve was derived using normalization, resampling, and averaging technique..... 91

Figure 6-10: The normalized root mean square error (NRMSE) considering tensile modulus, ultimate tensile stress, and ultimate tensile strain history. The conversion factor (X) was changed by an increment of 0.0001 to search the minimum NRMSE. The minimal NRMSE was found as 0.029, and the optimal conversion factor X_{opt} was 0.5234 93

Figure 6-11: The transferred porcine engineering stress-finite strain curve using the correlation factor X_{opt} . The optimal estimation of failure point based on the porcine test was plotted together with the failure point from human GP tests (William et al., 2001). The ranges of stress and strain at the failure points were indicated with plus/minus one standard deviation 93

Figure 6-12: The estimated 10 YO human femoral head GP tensile engineering stress- engineering strain relationship (a), and shearing engineering stress-strain relationship (b). The curves were transferred from 20 WO piglets’ mechanical properties of the same anatomic region. Three curves for the high, medium, and low strain rates were separately plotted for each loading condition. The curve portions beyond the failure points have been discarded 95

Figure 6-13: The estimated 10 YO human knee (distal femur and proximal tibia) GP tensile engineering stress - engineering strain relationship (a), and shearing engineering stress-strain relationship (b). The curves were transferred from 20 WO piglets’ mechanical properties of the same anatomic region. Three curves for the high, medium, and low strain rates were separately

plotted for each loading condition. The curve portions beyond the failure points have been discarded 96

Figure 7-1: Linear fitting for the initial portion of the tensile stress-strain and shearing stress-strain curves estimated for 10 YO child as shown previously in Figure 6-12. The Young's modulus and shear modulus were estimated to be: $E=3.29$ MPa, $G= 0.75$ MPa 102

Figure 7-2: Tension and shearing simulations using the generic FE model of a specimen. (a) Tension in the +Z direction; (b) shearing in the +X direction..... 106

Figure 7-3: The flow chart of the complete optimization process for human femoral head GP material properties. The left half is for the hyperelasticity associated parameters (bulk modulus, $C_1\sim C_6$) and the right half is for the viscosity associated parameters (S_i, T_i)..... 112

Figure 7-4: Engineering stress-strain curves of the femoral head GP of a 10 YO child, calculated by FE simulations with optimized GP material (market as "simu"), and estimated for 10 YO child from experimental study (market as "10 YO"). (a) tensile stress-strain curves comparison; (b) shearing stress-strain curves comparison 114

Figure 7-5: Verificatoin at medium rate. The red curves are calculated from the simulations of medium strain rates, using the parameter set determined from the optimization processes. The grey curves were the estimated curves for 10 YO child from Chapter 6 115

Figure 7-6: Optoimzation result of the knee GP for a 10 YO child. (a) tensile stress-strain curves comparison; (b) shear stress-strain curves comparison. The solid lines were from the simulations, while the solid-dot lines were from experimental study 116

Figure 7-7: 3D reconstruction of the proximal femur and femoral head GP based on CT scans of a 9.5 YO boy. (a) One slice of CT scan in the coronal plane in Mimics. The dense regions were colored in bright green, while the non-bony tissue or cavities were colored in grey in Mimics; (2) Extracted outer surfaces of the left proximal femur bone, and (c) The proximal surface of the left femoral head GP, meshed by triangular elements in Mimics..... 117

Figure 7-8: Reconstruction and modeling of the femoral head GP. (a) The proximal surface of GP extracted from the CT scans was scaled and located to the correct place in CHARM-10 proximal femur. 2D quadrilateral elements were used to reconstruct the GP proximal surface. A total of 72 elements (b) and 288 elements (c) were used to investigate which mesh density is better. The 3D plates of the femoral head GP were generated by dragging the 2D surface by 1.35 mm along the axial direction of the femoral neck 118

Figure 7-9: Details of the proximal femur FE sub-model with the GPs embedded the GPs. The lower mesh density model is shown here..... 119

Figure 7-10: The femoral head GP shearing test. (a) The FE model with a higher loading speed with the viscosity of the GP material disabled. (b) The setup of the shearing experiment carried out by Chung et al. (1976)..... 120

Figure 7-11: Force displacement histories for the updated femoral head models. The solid curves are from the model with perichondrial cartilage, and the dot curves are from the model without perichondrial cartilage. Both the higher and lower mesh density models were used for this analysis 123

Figure 7-12: GP embedding: (a) GPs at the knee joint (distal femur and proximal tibia) (b) Triradiate cartilage. The shape and morphological details of these GPs were approximate and not as accurate as the femoral head GP..... 126

Figure 7-13: The updated PLEX model of the 10 YO child with GPs embedded: (a) The pelvic region and (b) The knee region. Some soft tissues were hidden for better viewing. TC: triradiate cartilage, GT: greater trochanter, FH: femoral head, DF: distal femur, PT: proximal tibia 127

Figure 7-14: Simulation setup of the SUV-to-pedestrian impact..... 128

Figure 7-15: The Maximum Principal Strain (MPS) contours of the simulation using the baseline CHARM-10 model. The unit of the countour is GPa. The four cirtical regions are: (A) bottom of acetabulum, (B) ischiopubic ramus, (C) the medial side of femoral shaft, and (D) the medial side of tibia shaft. Only cortical bones are presented in these figures..... 129

Figure 7-16: The Maximum Principal Strain (MPS) contours of the simulation using the updated CHARM-10 model including the PLEX GPs..... 130

Figure 7-17: The MPS history comparisons between the baseline model (without GP) and updated model (with GPs), at four monitored locations. (a) at location A; (b) at location B; (c) at location C; (d) at location D..... 131

Figure 7-18: MPS distribution of (a) proximal femur GPs (FH and GT), (b) knee GPs (DF and PT). $t=22$ ms. The elements under arrows are the elements of interest, and are used for local deformation analysis..... 132

Figure 7-19: FE models of a specimen with different mesh densities. The numbers of elements for the GP only (shown as a layer of green elements in each model above) are (a) 25, (b) 675, (c) 4,500, and (d) 36,000, respectively 134

Figure 7-20: Simulation results of FE models with different mesh densities 135

Figure 7-21: Material axes for elements in GP using different methods: (a) by element nodes, (b) by a vector. The local orthotropic axis for each element is shown by letter A, B, and C, while C is indicating the fiber orientation. It is noted that in both method, the fiber orientation in one element will be updated in each time step of the simulation. (c) is showing the shearing force difference between two GP models using these methods, respectively 137

CHAPTER 1. INTRODUCTIONS

As reported by the Centers for Disease Control and Prevention (CDC), from 1999 to 2013, motor vehicle traffic related incident ranked first among all intentional and unintentional causes of injury-caused deaths for children aged 1-14 (CDC, 2015). Besides occupant impact in car crashes, motor vehicle to pedestrian impact is also a major cause of injuries and deaths to children. According to the 2011 data published by National Highway Traffic Safety Administration (NHTSA), for children aged 14 years or younger, 20% of the road traffic fatalities were caused by vehicle-to-pedestrian impacts (NHTSA, 2013). Worldwide, about 30% - 40% of children injured or killed in traffic are pedestrians, and this higher percentage is due to the inclusion of more low-income countries (WHO, 2008).

Among all pedestrian casualties, children should be paid more attention, especially for age of 8 to 12 years. Worldwide, around 35% of pedestrian deaths were children (Untaroiu et al., 2010). Wazana et al. (1997) reviewed earlier studies and stated that, pedestrians between the ages of 8 and 12 have the highest rate of injury (per unit time) compared to other children groups. In 2011, totally 4,432 pedestrian fatalities occurred in the US, 5.2% of which were children aged 14 years or younger; whereas the same age group accounted for 15.9% of all 69,000 injured pedestrians. The fatalities of age group 8 to 14 years were more than the summation of the other child age groups (NHTSA, 2013), as shown in Figure 1-1. More in-depth epidemiology studies will be reviewed in CHAPTER 2.

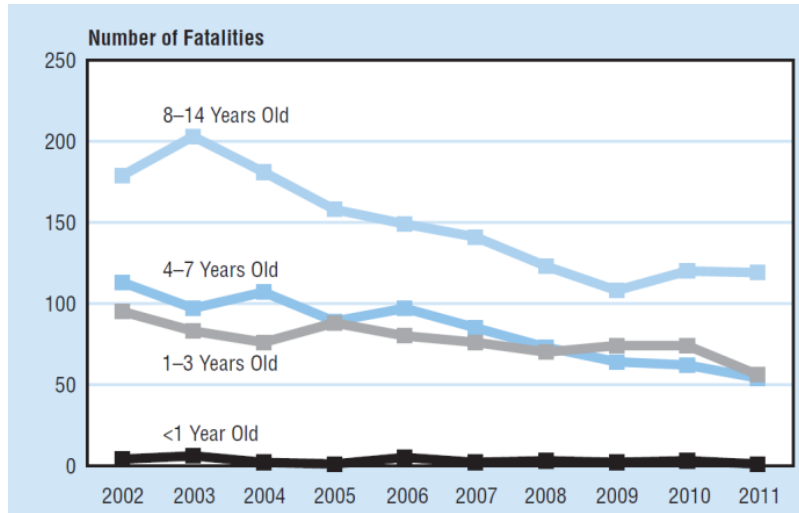


Figure 1-1: Pedestrian fatalities among children aged 14 and younger, by age group, 2002-2011 (NHTSA, 2013)

To investigate the pedestrian injury mechanisms and further protect the pedestrians better, some methodologies have been used. These could be divided into two categories: (1) physical tests using post mortem human subject (PMHS), volunteers, anthropomorphic test devices (ATDs) or animal surrogates; (2) numerical simulations using multi rigid-body models or finite element (FE) models. They all have some limitations to a certain extent, which are briefly summarized as follows. Due to ethnic and legal concerns, the quantity of pediatric PMHS studies is very small. Volunteer tests are conducted in unreal impact loadings with a lower intensity. ATDs are standardized and repeatable for industrial application, but the biofidelity could be further improved. Animal surrogates are usually implemented for body region or organ tests where the accessibility of human subjects is low. Multi-body modeling technique lacks detailed geometry of human body. Lastly, FE method is a commonly used technique for pedestrian impact research but the pervious modeling

efforts were scarce for children around 10 years old (YO). More details about current research methodologies will be reviewed in Chapter 3.

As a result, a whole-body FE model for a 10 YO child with high biofidelity was desired in order to better understand the injury mechanism of children impacted by vehicles. Since the pelvis and lower extremities (PLEX) are where the first contacts usually occur, and they also account for the largest portion of AIS 2+ injuries for pedestrians (Kikuchi et al., 2006, 2008), an accurate PLEX FE model for children around 10 YO is proposed in this dissertation study.

In terms of model biofidelity for a numerical model representing a child, some special tissues for child are critical for injury biomechanics, such as the epiphyseal growth plate. Epiphyseal growth plate (GP), also known as physis, is where growth occurs at the cellular level for immature bones.



Figure 1-2: The X-ray image of knee with GPs gaps between epiphysis and metaphysis, because non-ossified GPs are radiolucent in X-ray (by Danna 2011, obtained from <https://thesebonesofmine.wordpress.com/category/femur>)

Taking knee region as an example, shown as the dark gaps at the ends of distal femur and proximal tibia in Figure 1-2, the GP is the layer between the epiphysis and metaphysis (a transitional segment from epiphysis to diaphysis) and is responsible for the growth in length of the bone.

The GP is weaker than surrounding cortical or trabecular bones, and this mechanical weakening accounts for GP related fractures that occur to adolescents and younger children, and constitute 15% to 20% of all childhood fractures (Peterson, 2007). A GP on the epiphysis enables the longitudinal growth of long bone and GP damage may lead to a growth arrest and long-term disturbance (Caine et al., 2006; Peterson, 2007). The GP is vulnerable in shearing, which is perpendicular to the bone's longitudinal growth axis, a likely loading mode in a pedestrian impact. Hence, it is important to include GPs in the modeling of a pediatric pedestrian.

To model the GP, material property of GP needs to be investigated. Although some GPs have similar appearances like cartilages (Tschegg et al., 2012; Villemure and Stokes, 2009) or even termed as cartilage, it is not proper to treat it as a cartilage mechanically. For example, Cohen et al. (1992) found that, the tensile modulus of bovine GP was 35.0 MPa, which is much lower than the elastic moduli for articular cartilage and meniscus at 84 MPa and 200 MPa, respectively. In a word, the GP is a critical component in pediatric pedestrian computational modeling, and an investigation of its structure and material property is important and wanted.

Unfortunately, it was found that only very few experimental studies of human GP were available in the literature. A number of tests on animal GPs were found, however most of them

were limited to a single anatomic site (e.g. proximal tibia GP) and most of them were not associated with the loading condition of a car-to-pedestrian impact (high strain rate, lateral shearing).

Based on the literature reviews, the dissertation study was planned with three specific aims. They are shown as follows, with the research contents under each aim.

Specific Aim 1: Develop an average representative FE model for PLEX of a 10 YO child, as a baseline model for pedestrian protection study.

Anthropometric study and clinical images assured the external and internal dimensions. The baseline model was validated against available pediatric PMHS test data and additional scaled adult data, then the PLEX model was integrated to build a whole-body FE model representing a 10 YO pedestrian.

Specific Aim 2: Investigate the mechanical behaviors of the GPs by conducting experiments on the porcine GP specimens.

A series of tensile and shearing experiments on porcine bone-GP-bone units were carried out. The GPs from the femoral head, distal femur, and proximal tibia of 20-weeks-old piglets were tested, under different strain rates. Randomized block ANOVA was conducted to determine the effects of anatomic region and strain rate on the material properties of GPs. By comparing the porcine experimental data to the limited data obtained from tests on human subjects reported in the literature, an optimal conversion factor was derived to correlate the material properties of 20-week-old piglet GP and 10 YO child GP.

Specific Aim 3: Determine the material properties for GPs of a 10 YO child. Explore the FE modeling technique of GP in the whole-body human model.

A transversely isotropic hyperelastic material model (MAT_92 available in LS-DYNA) with added viscosity was adopted to mimic the GP tissues. After a series of optimization procedures, the material parameters needed for MAT_92 were determined to represent the GPs in different regions of a 10 YO child. Parametric studies were conducted by using the proximal sub-model to explore the GP modeling techniques. Subsequently, as a practical application, these techniques were implemented in a whole-body pediatric pedestrian model to assess the mechanical influences of the GPs to the pedestrian responses.

CHAPTER 2. EPIDEMIOLOGIC REVIEW

2.1. PEDIATRIC PEDESTRIAN ACCIDENT

Continued from the Introduction section, more pedestrian injury characteristics related to age and body region are further summarized in this section.

Back to 1980's, NHTSA conducted the Pedestrian Injury Causation Study (PICS), involving pedestrian accidents from 1977 to 1980. Later in 1995, NHTSA further initiated the Pedestrian Crash Data Study (PCDS) to investigate the detailed information related to pedestrian casualties (Jarrett and Saul, 1998). Altogether 521 pedestrian accidents were included by Dec. 31, 1998 (Chidester and Isenberg, 2001). In the age distribution study, 6-10 years of age had the highest incident rate reported in PICS, and this group was still the second highest group in PCDS, as shown in Figure 2-1. Based on PCDS, the impact orientations were examined and it was found that the most dominant (approximately 70%) impact direction was side impact (Jarrett and Saul, 1998). A statistics study conducted in New York City demonstrated that, the injury rate (per 100,000 populations) peaked for age 8 to 12 (DiMaggio and Durkin, 2002).

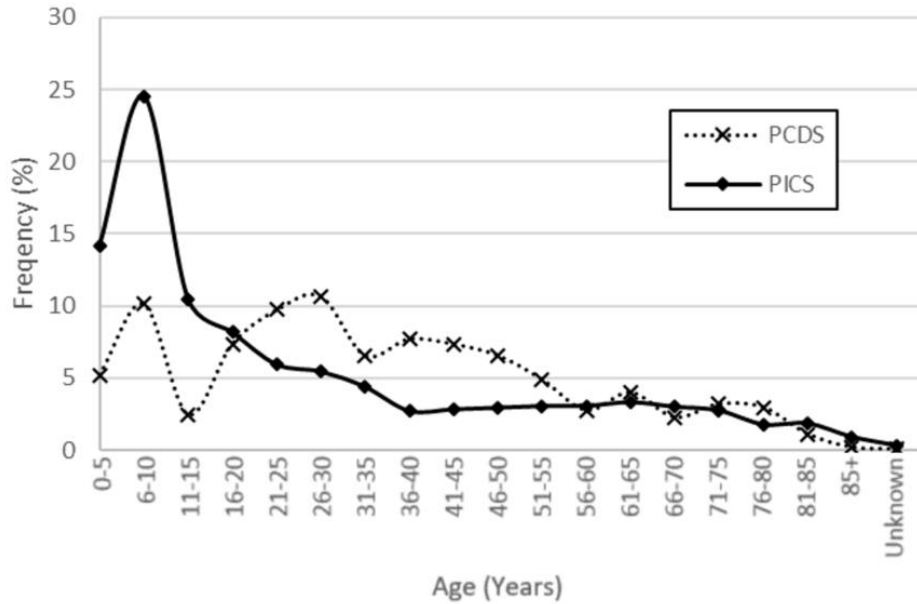


Figure 2-1: Age distribution of two pedestrian data analysis studies initiated by NHTSA (PICS and PCDS). Re-drawn from the original plot by Jarrett and Saul (1998)

The same trend was found in more recent field data. In year 2012, pedestrian injuries in children aged 10 to 15 were the highest among all age groups and accounted for 22% of fatalities and 9% of injuries (NHTSA, 2014). The above epidemiologic review demonstrated that, for children around 10 YO, car-to-pedestrian impact is a key cause of injury or death. Whereas for all pedestrian impacts, age group around 10 years has the highest injury risk.

The PCDS database was utilized by many researchers as the main source of data for in-depth injury pattern investigation. The injury pattern in terms of distribution on different body regions is reviewed and summarized below, focusing on the characteristics of the PLEX. For all injuries, lower extremity was the most frequent injured region as shown in Figure 2-2 (a) (Chidester and Isenberg, 2001). Given the slight injuries such as integumentary scratches may distort the distribution, further examination was made for different injury severities, in terms of Abbreviate

Injury Scale (AIS). The skin (integumentary) injuries (AIS 1) account for 64% of all pedestrian injuries. The body region distribution for $AIS \geq 2$ is shown in Figure 2-2 (b), and the lower extremity has the highest injury frequency, followed by head (Kikuchi et al., 2006).

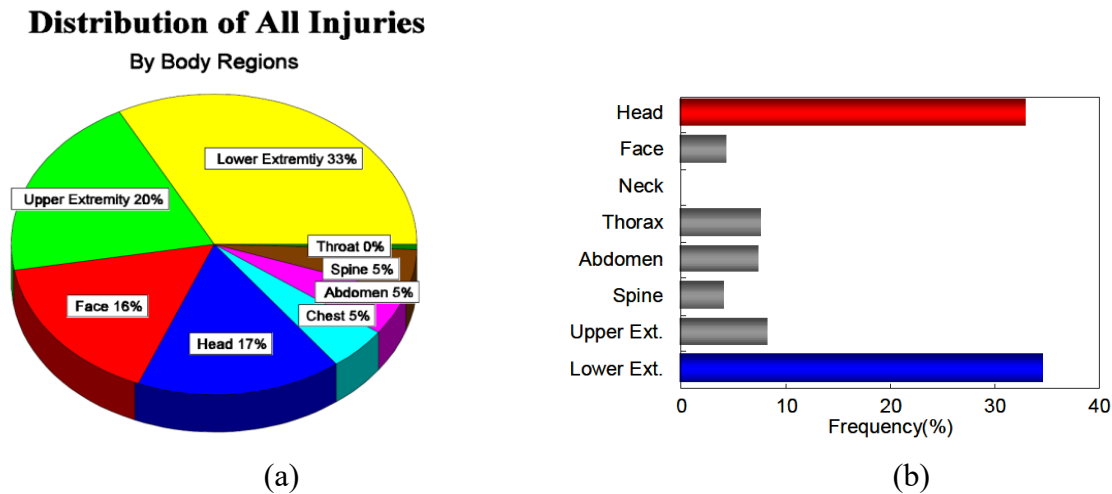


Figure 2-2: Pedestrian injury distribution based on PCDS database. (a) all injuries (Chidester and Isenberg, 2001); (b) injury for $AIS \geq 2$ (Kikuchi et al., 2006)

Ivarsson et al. (2006) grouped the ages and discussed the age related change on the injury pattern for $AIS \geq 2$ (Figure 2-3 a) and $AIS \geq 3$ (Figure 2-3 b) pedestrian injuries respectively, based on PCDS data (Ivarsson et al., 2006). It was observed that the lower extremities and head & face are the two most frequently injured regions for all five age groups. The proportion of casualties who sustained an $AIS 2+$ lower extremity injury was 18% in the youngest group of 1-3 YO, 40–50% in the other four age groups. For $AIS 3+$ lower extremities injuries, age group of 4-6 YO has the highest rate, followed by age group of 7-9 YO.

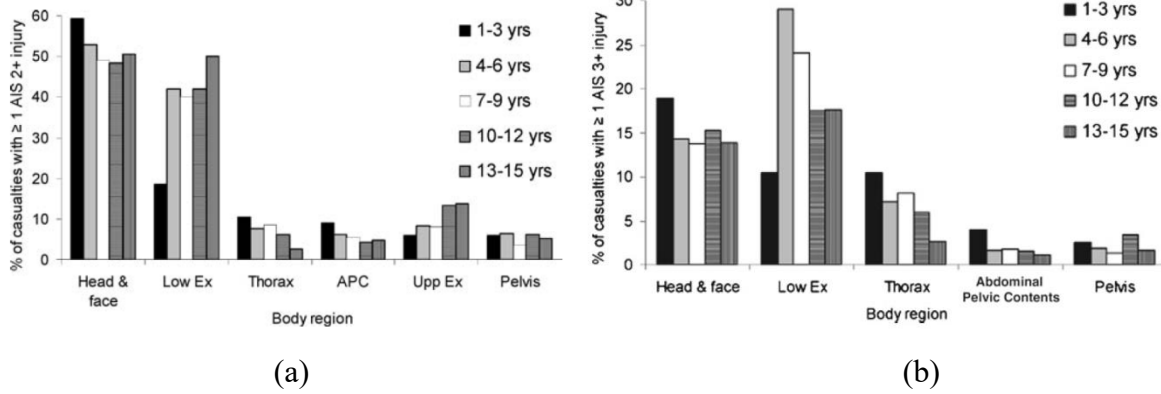


Figure 2-3: Pedestrian injury distribution for children. (a) with at least one AIS 2+ injury; (b) with at least one AIS 3+ injury (Ivarsson et al., 2006). The injury percentages for spine (lumbar or thoracic) and neck (including cervical spine) did not exceed 2% for all age groups in two frequency investigations, therefore not shown in both figures

Pedestrian PLEX injuries were further subdivided into several body segments. Kikuchi et al. (2006) did an overall study involving all age groups older than one year, as shown in Figure 2-4 (a). It consists of fractures to the pelvis, femur and tibia along with fractures at the knee joint and knee ligament rupture. The tibia/fibula had the highest percentage of PLEX injuries. Ivarsson et al. (2006) further studied the injury distributions in the lower limbs for different age groups. It was found that tibia/fibular injuries increased with age increased.

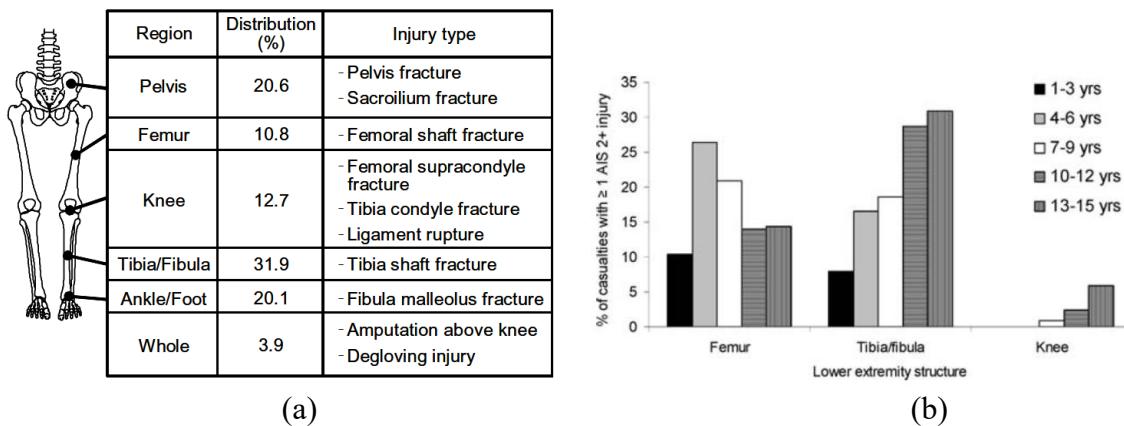


Figure 2-4: Distribution of pedestrian injuries (AIS 2+) at pelvis and lower extremity. (a) for all age groups (Kikuchi et al., 2006); (b) for children (Ivarsson et al., 2006)

Compared to the overall distribution, children with smaller body statures have higher injury incidence on upper femur and pelvis in pedestrian impacts (Mizuno and Ishikawa, 2005). Based on a 14-year-long review of pediatric pedestrian injuries at a Level I trauma center, Woods et al. (2003) revealed that femur injuries were more common in younger than in older children, but old children were more likely to suffer lower leg, ankle, and foot injuries. In a 10 years trauma registry study on pedestrian injuries in Los Angeles (Demetriades et al., 2004), several significant differences between children (≤ 14 YO) and the adults (55-65 for example) were found: Children had more femur injuries (15.5% vs. 8.3%) and less tibia injuries (15% vs. 34.8%); However, children had less pelvic fractures (6.3% vs. 16.2%).

The contact points between the pedestrian and the vehicle are critical for the injury outcomes, which were determined by the impact speed, the profile of vehicle front end and the pedestrian anthropometry (Mizuno and Ishikawa, 2005; Roudsari et al., 2005). It is illustrated in Figure 2-5, that the primary impact spot (bumper to the pelvis or lower extremity) and the secondary impact spot (the head to hood/windshield) were different among different ages (Serre et al., 2010). This significant difference between adult and child pedestrians suggested that the car design optimized for adult pedestrian impact may not be favorable for children. In-depth study on injury mechanisms of children is highly demanded.

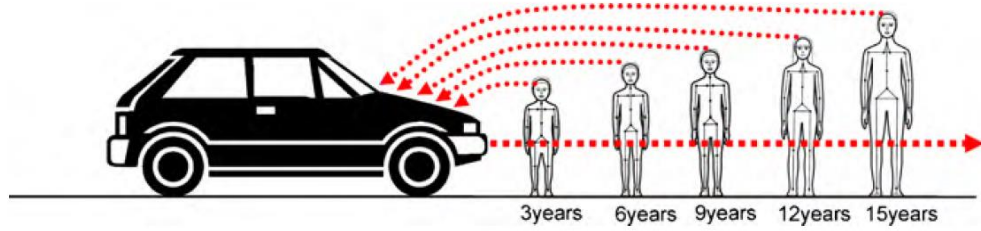


Figure 2-5: Locations of bumper impacting on the lower limb and the head impacting on the hood or windshield for pedestrians with different ages (Serre et al., 2010)

The average shapes and dimensions of vehicle front end were measured and standardized by Mizuno and Ishikawa (2005), and the average leading edge height (LEH) for light weight car is 702 mm, which is right at the greater trochanter region for an average 9 YO, however just above the middle of femur shaft for an adult (Serre et al., 2010). In a review of Australian and German pedestrian accidents, Fildes et al. (2004) measured the total societal cost and ranked the top ten injured body regions and associated impact modes. Some distinction between children and adults could be seen in Table 2-1. For example, "upper leg to bumper" injury was ranked as the third for children, which was not in the top ten for adults.

Table 2-1: Top ten priorities of pediatric pedestrian injury mitigation with social cost percentages compared with adults' (Fildes et al., 2004)

Top ten priorities for child pedestrian injury mitigation	Harm associated with child pedestrian injury (%)	Harm associated with adult pedestrian injury (%)
Head to hood	16	8
Head to ground	11	8
Leg above the knee to bumper	9	^b
Head to front area of vehicle ^a	9	^b
Leg below the knee to bumper	8	12
Head to A-pillar	6	7
Pelvis to front area of vehicle ^a	5	4
Head to windshield	4	21
Leg above the knee to front area of vehicle ^a	3	2
Chest to hood	3	4

The injuries at the PLEX are typically not life threatening, compared to the head and thoracic injuries. However, from the point view of long-term consequences and social costs, these injuries shall also draw attention of researchers. On the other hand, pelvis or lower extremities are the first body region where vehicle-to-pedestrian impact happens. The mechanical and kinematical responses of these lower body parts will determine the following overall behavior of pedestrian and the loading directions and energy levels from the vehicle or the ground upon to the upper torso and head. Therefore, a better model of the PLEX is critical to a study of whole-body human model for pedestrian protection.

Above brief epidemiologic reviews have revealed that for children around 10 YO, pedestrian crash is a key cause of injury or death. For all pedestrian accidents, age group around 10 years has the higher risk compared to other age groups of children. These explained the reason why age group of 10 YO was selected in this study. The detailed injury pattern among different body regions showed particular needs for pediatric pedestrian impact study, and the importance of developing a biofidelic PLEX model as well.

2.2. GROWTH PLATE TRAUMATIC INJURY

Traumatic injuries of the GP are reviewed here to emphasize the important role of GP played under mechanical loadings. They include all types of traumas rather than car-to-pedestrian impacts, since epidemiologic data for this specific tissue in this specific traffic mode was not available.

Peterson and Peterson (1972) reviewed epiphyseal GP injuries cases at Mayo Clinic of Minnesota (330 cases through 20 years). As shown in the first column of Table 2-2, the distal radius

was the location where GP injuries happen most frequently, followed by the phalanges and then the distal tibia. In contrast, proximal ends of long bones such as the tibia, femur, radius, ulna and fibula rarely had GP fractures. Later, Peterson (2007) did a comprehensive retrospective review including 4534 cases in 14 epidemiologic studies from 1915 to 1987 and discovered similar trends.

Focusing on the lower extremities GP injuries in Table 2-2, it can be seen that distal tibia is the most frequent injured site (15%, ranks behind distal radius and phalanges), followed by distal fibula (4.0%) and distal femur (3.1%). The proximal tibia has the highest incident proportion (2.5%) among the proximal ends of long bones (Figure 2-6).

Table 2-2: The injury frequency distribution among GPs, later than 1970's (Peterson, 2007)

Site ^b	1972 Peterson and Peterson [28]	1981 Ogden [25]	1987 Chadwick and Bentley [6]	1987 Mizuta et al. [22]	Total	Percent
1. Distal radius	98	114	26	100	338	28.1
2. Phalanges (fingers)	39	41	10	91	181	15.1
3. Distal tibia	59	60	28	33	180	15.0
4. Distal humerus	20	56	31	24	131	10.9
5. Proximal humerus	22	27	3	7	59	4.9
6. Phalanges (toes)	11	21	–	25	57	4.7
7. Distal fibula	21	15	–	12	48	4.0
8. Distal ulna	12	11	1	16	40	3.3
9. Distal femur	18	17	1	1	37	3.1
10. Metacarpals	10	8	–	15	33	2.7
11. Proximal tibia	6	20	–	4	30	2.5
12. Proximal radius	1	5	3	16	25	2.1
13. Proximal femur	7	9	–	–	16	1.3
14. Metatarsals	6	3	–	5	14	1.2
15. Proximal ulna	–	3	–	1	4	0.3
16. Clavicle, lateral	–	1	–	3	4	0.3
17. Clavicle, medial	–	3	–	–	3	0.2
18. Proximal fibula	–	2	–	–	2	0.2
TOTALS	330	416	103	353	1202	99.9

Generally speaking, the GPs at distal ends of long bones were injured much more frequently. Injuries of the proximal forearm and lower leg were infrequent. It does not mean that GPs at some specific anatomic sites are physiologically more vulnerable than other sites, but it is associated with the more exposure to trauma with higher kinematic energies.

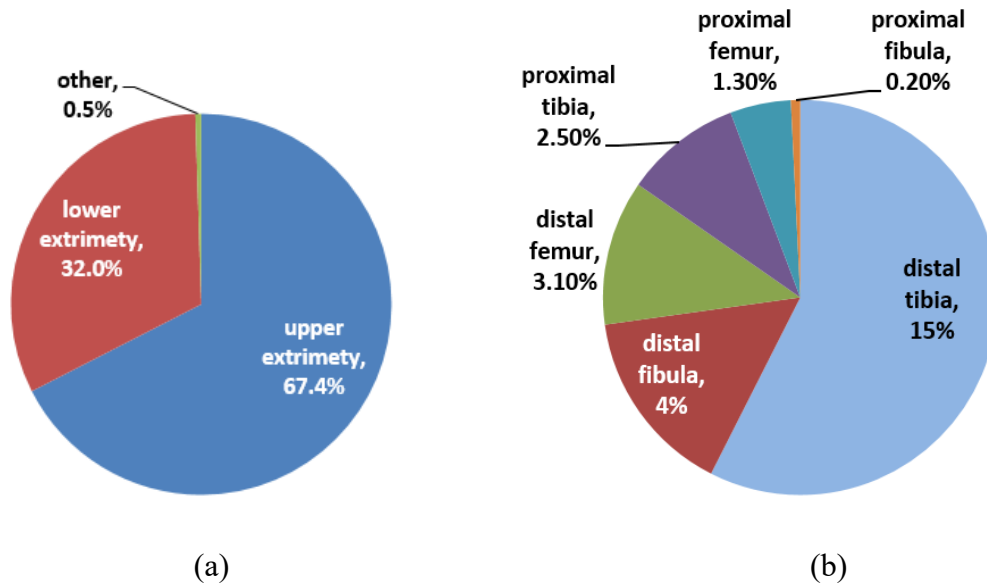


Figure 2-6: Distribution of GP injuries drawn based on the data in Table 2-2 by Peterson (2007). (a) Overall distribution; (b) Distribution at three long bones of the lower extremities

Fractures of GP are categorized in different ways. The most common classification was proposed by Salter and Harris in 1960s (Salter and Harris, 1963). Figure 2-7 shows the five major types of GP fractures.

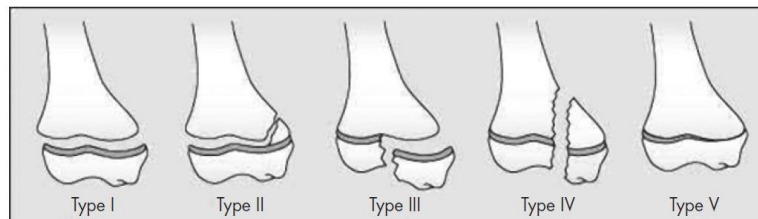


Figure 2-7: Salter-Harris epiphyseal fracture classification (Salter and Harris, 1963)

Type I: A transverse fracture through the GP. It accounts for 15.1% of all GP fracture incidences. Here, the percentages of fracture distribution by type were provided by Peterson (2007), considering epidemiologic studies from 1933 to 1994.

Type II: A fracture through part of the GP and part of the metaphysis, so that the epiphysis is separated. It accounts for 59.9% of all incidences. Usually it takes approximately 2–3 weeks to heal.

Type III: A fracture through part of GP and part of epiphysis, sparing a portion of epiphysis. It accounts for 10.3% of all incidences.

Type IV: A fracture through metaphysis, the GP and epiphysis. GP interface has no separation in this case. It accounts for 9.2% of all incidences.

Type V – A compression fracture of the GP (resulting in a decrease in the perceived space between the epiphysis and diaphysis on X-ray). It has an incidence ratio of 0.3%.

Another important type of GP is the one lying on the bottom of the acetabulum, which is also termed as triradiate cartilage (more anatomic details will be given in Section 5.1). Generally, the injury of triradiate cartilage is relatively rare, compared to the other GP in the PLEX. Up to 20% of children with major pelvic injuries would have injuries of the triradiate cartilage (Bucholz et al., 1982). Further case reviewing revealed that most of the triradiate cartilage fractures were caused by car-to-pedestrian collision (Bucholz et al., 1982; Heeg et al., 1988). In a study by Von Heyden et al. (2012), 15 children acetabulum fractures were observed, which accounted for 9.8% of all

pelvic fractures for children, as shown in Table 2-3. In contrast, the acetabular fractures accounted for 22.3% of all pelvic fractures for adults.

Table 2-3: The incidence rate of pelvic fractures and acetabular fracture for children and adults (Von Heyden et al., 2012)

	Number	Percentage	P*
Total pelvic fractures (period 1-3)	7360		
Paediatric pelvic fractures	153	2.1	
Pelvic fractures in adults	7207	97.9	< 0.0000001
Paediatric acetabular fractures	15/153	9.8	
Acetabular fractures in adults	1604/7207	22.3	0.0001073

In another trauma registry study over nine years involving 166 patients with pelvic fractures, it was found that children had fewer acetabular fractures compared with adults (6% vs. 44%), whereas they had more ramus and iliac wing fractures than adults (53% vs. 31% and 29% vs. 6%) (Silber and Flynn, 2002). Above epidemiologic data implied that the triradiate cartilage might increase the compliance of the pediatric pelvis, compared to an acetabulum with ossified GP from an adult. Very few FE modeling study has been directed to this immature structure. This Y-shaped GP was also modeled and included in the PLEX FE model to be described in later chapters.

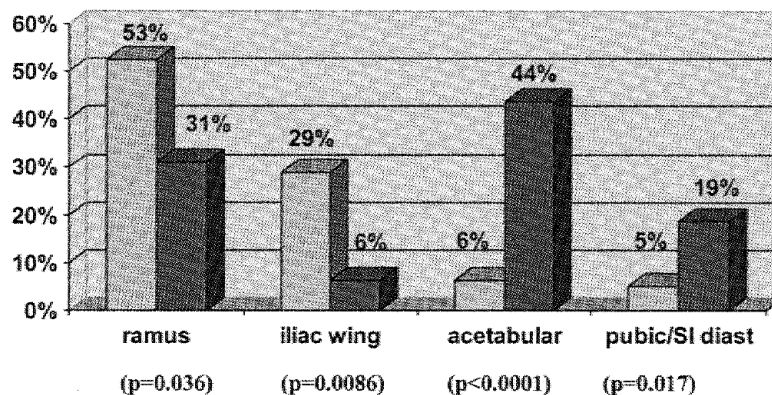


Figure 2-8: The fractions of fracture happening to different pelvic locations for immature (lighter bars) and mature (darker bars) pelvic groups (Silber and Flynn, 2002)

CHAPTER 3. RESEARCH TOOLS FOR PEDESTRIAN PROTECTION

Methodologies pertaining to human impact biomechanics include two categories: (1) physical tests using PMHS, volunteers, anthropomorphic test devices (ATDs) or animal surrogates; and (2) numerical modeling using multi rigid-body models or FE models.

PMHS biomechanics experiments have long been providing important fundamentals and golden standards for human computational modeling. However, pediatric PMHS experiments for computational model validations are extremely rare and this situation highly hampers the development of an accurate FE pediatric human model. In this study, pediatric test results from Ouyang group, (Ouyang et al., 2003a) and (Ouyang et al., 2003b) were used for validation of lower limb bones and pelvis sub-model. Those data are valuable and have already been used by several model validation publications (Ito et al., 2009; Ivarsson et al., 2004; Kim et al., 2009). Some early tests by Asang et al. (1969) and Asang et al. (1973) [cited by (Ivarsson et al., 2004)] reported two data points of ultimate bending moments of 12 YO children's tibiae, however the subject details were not available. Upon literature review, no additional experimental studies on PLEX of children from 8 to 12 YO were found, this study therefore mostly rely on test data of Ouyang group, and explore the scaling methodologies for implementation of adult PMHS test data.

Volunteer tests in related to pediatric responses were mainly whole-body kinematic studies. For example, Arbogast et al. (2009) conducted a series of sled deceleration tests to study the responses of belted volunteers in low speed frontal impact. They could provide vivid information regarding the real human motions before and during a minor crash event. Some advanced tests

measured the muscle activation levels using EMG (Choi et al., 2005). However, results from volunteer test usually cannot provide sufficient insights for the purpose of FE model validation, because the loading condition is much less severe than a real-world accident to protect the volunteers. Additionally, the activation of muscle may play a role in a volunteer test, which is a confounding factor when the results are adopted to validate a model without active muscles.

Humanetics (Plymouth, MI, US) developed a Hybrid III 10 YO dummy, where the geometric and material parameters were scaled from adult dummies (Irwin and Mertz, 1997; Irwin et al., 2002). The European project of enabling protection for older children (EPOCH) extended the Q-series dummy to include the Q10 dummy for the 10 YO group by basically scaling from other child dummies in 2010 (Humanetics, 2014). However, these dummies were not specifically designed for use in studying pedestrian protection of children. To reduce the injuries at lower limbs, some regional test devices were developed and standardized, such as headform and upper legform and legform impactors in ECE 127 Regulation (United Nations, 2012), originally proposed by the European Enhanced Vehicle-safety Committee (EEVC) Working Group 17 (EEVC, 1998). ATDs can be used in severe crash tests as standardized measuring tools. However, some studies have raised issues that the biofidelity of these regional impactors and the validity of the associated injury criteria still need further improvement (Konosu et al., 2001; Matsui et al., 1999; Takahashi and Kikuchi, 2001). Additionally, they were targeting the adults. To sum up, the structures of these ATDs cannot accurately mimic the muscles, ligaments and bones in the pediatric pedestrian body.

Other features such as GPs are missing in ATDs as well.

Animal surrogates have been implemented to study the biomechanical responses since cadaveric tests on children are difficult due to ethnic and legal concerns. After decades of studies, animal surrogates are usually for in-depth material property or injury mechanism study of a certain tissues/organs, which are difficult to obtain from human. For example, Jin (2009) used cow samples to estimate the material property of human pia-arachnoid complex; Mao and Yang (2011) used rat brain to investigate the contusion mechanism and threshold. For pediatric GP modeling in this study, animal surrogates were implemented to identify GP properties. Pig, cow, sheep, mouse, orangutan etc. are used previously in GP related experimental studies. Briefly, pig is one of species that are most frequently used for biomechanical study because of the comparable dimensions and easy accessibility.

MADYMO (TASS, Helmond, the Netherlands) is a multi-body modeling software commonly used to conduct multi-body system simulations of pedestrian impact. In 2002, Liu and Yang developed child pedestrian models for children with ages of 3, 6, 9 and 15 YO in the MADYMO by scaling a 50th percentile male pedestrian model (Liu and Yang, 2002). Van Rooij et al. developed a 6 YO multi-body pedestrian model by scaling down from a 50th percentile adult model (Van Rooij et al., 2003; Van Rooij et al., 2004). Yao et al. used MADYMO to reconstruct a collision involving a 7 YO pedestrian (Yao et al., 2006). Untaroiu et al. analyzed the kinematic responses of a 9 YO running pedestrian (Untaroiu et al., 2010). The rigid bodies, which represent human body segments, make this methodology favorable for straightforward kinematic and dynamic

analysis, but limit the biofidelity and capability to mimic the deformation and failure of human tissue/organs.

Finite Element (FE) models can well predict the injury responses with relatively accurate geometry and material representations. Much effort has been directed towards the development of adult human models for pedestrian and occupant safety studies (Kalra et al., 2016). Total Human Model for Safety (THUMS) and Global Human Body Models Consortium (GHBMC) are two well-known whole-body human models for adults (Maeno and Hasegawa, 2001; Untaroiu et al., 2013; Yue et al., 2011). In contrast, fewer pediatric FE models have been built, mainly because of the lack of child biomechanical experimental data. Such experimental data from child PMHS are limited due to regulatory and ethical concerns. For the same reason, TOYOTA developed a 6 YO THUMS model by scaling down the adult model, but they could not validate and officially distribute it (Iwamoto et al., 2007). A 3 YO and a 6 YO FE models were developed by Mizuno et al. (2005) and Okamoto et al. (2003), respectively. The 3 YO model was developed by scaling down the geometry from adults FE model. The lower limbs of the 6 YO model were based on magnetic resonance imaging (MRI) scans of children. By scaling up this 6 YO model, Ito et al. developed the lower limbs model for three pedestrians around 10 YO (Ito et al., 2009). Kim et al. developed a pelvis model using computed tomography (CT) scans from a 10 YO female and the material properties were identified by optimization approaches (Kim et al., 2013; Kim et al., 2009). Up to date, there is no 10 YO FE full pelvis and lower extremity (PLEX) model directly developed from pediatric anatomy of the same age, and the GP injuries were not well investigated, either.

Based on the above review, FE modeling was the reasonable research tool adopted in this dissertation to investigate the pediatric pedestrian injury biomechanics. An FE baseline model of the PLEX of a 10 YO child was developed. GP tissues were also modeling by FE approaches, and then embedded to the FE sub-model of proximal femur, and further the FE PLEX model of 10 YO.

CHAPTER 4. BASELINE PLEX FE MODEL DEVELOPMENT

Most of the contents included in this chapter have been published as Shen et al. (2015b). The relevant paragraphs, tables, and figures were reformatted for incorporation within this dissertation.

4.1. GEOMETRIC AND ANTHROPOMETRIC STUDY

The geometric dataset for the 10 YO PLEX model was originally taken from clinical CT scans of 10 ± 0.5 YO children at the Children's Hospital of Michigan (CHM), with the approval of the Institutional Review Board (IRB)/Human Investigation Committee (HIC) of Wayne State University (Mao et al., 2014). An external anthropometric investigation was performed based on the anthropometry study by Snyder et al. (1977) in which measurements were taken from 258 children aged 9.5-10.5 years. Combined with data for internal dimensions reported in the literature, these data were used to conduct minor adjustments of CT images, and the results are listed in Table 4-1. Additionally, several key dimensions were obtained in collaboration with the International Center of Automotive Medicine (ICAM) of University of Michigan, involving 56 subjects, labeled as "ICAM" in Table 4-1. The height and weight of the 10 YO whole-body FE model (Version 1.1) are 1401 mm and 35.0 kg respectively. Figure 4-1 shows the dimension comparisons between the 10 YO model and anthropometric measurements from the references. More data were summarized and published by Mao et al. (2014). An oblique view of the computer aided design (CAD) model is shown in Figure 4-2 (a).

Table 4-1: Anthropometric study summary

External measurement				
Items	Measured (mm), (\pm SD)	Model (mm)	Model error (%)	Reference
Hip breath at greater trochanter	242	236	-2.5%	Snyder et al. (1977)
Buttock height	692	690	-0.3%	Snyder et al. (1977)
Upper thigh circumference	421	419	-0.5%	Snyder et al. (1977)
Max. shank circumference	278	277	-0.4%	Snyder et al. (1977)
Foot length	216	216	0.0%	Snyder et al. (1977)
Femur length	345.0	345.5	+0.1%	Volgyi et al. (2010)
Tibia length	315	316	+0.3%	Volgyi et al. (2010)
Internal measurement (imaging based)				
Femur neck length	78.5 (\pm 5.5)	76.2	-2.9%	Goulding et al. (1996)
Femur neck width	24.4 (\pm 2.1)	24.0	-1.6%	Goulding et al. (1996)
Pelvis great width	203.9 (\pm 14.2)	205.0	+0.5%	ICAM
Ilium depth	98.5 (\pm 10)	100.0	+1.5%	ICAM
Pelvis height	160.3 (\pm 9.7)	160.4	+0.1%	ICAM
Pelvis inner width	91.3 (\pm 9.8)	85.9	-5.9%	ICAM

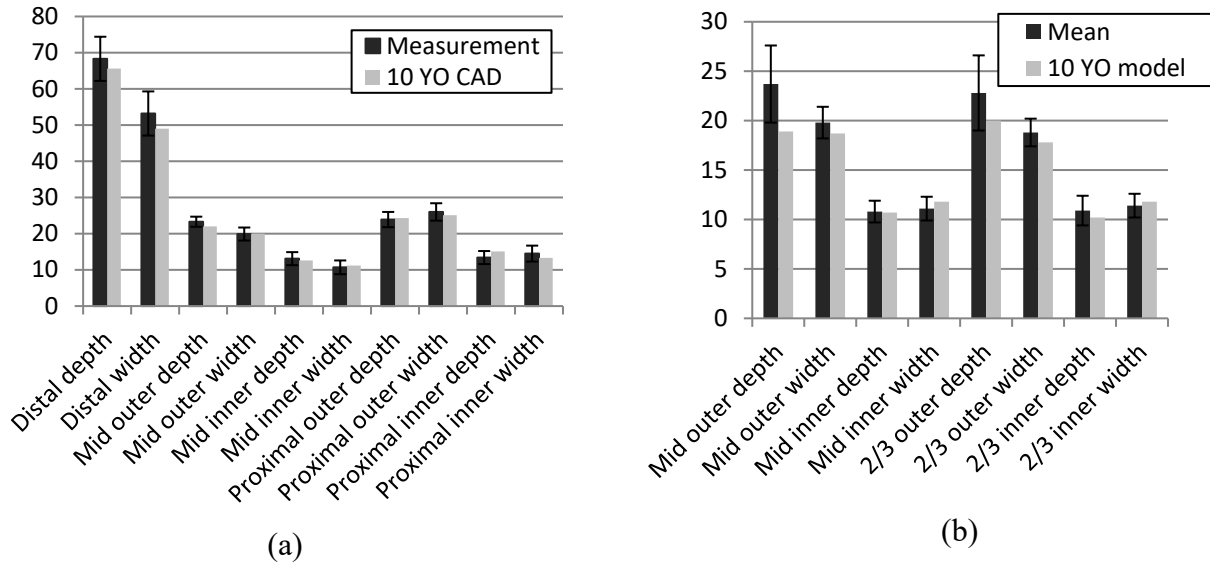


Figure 4-1: Dimension comparison between measurement and 10 YO model for femur (a) and tibia (b). "Proximal" refers to the cross section 20 mm distal/below the less trochanter. "2/3" refers to the cross section lower/distal from the tibia condyle by 2/3 of the bone length

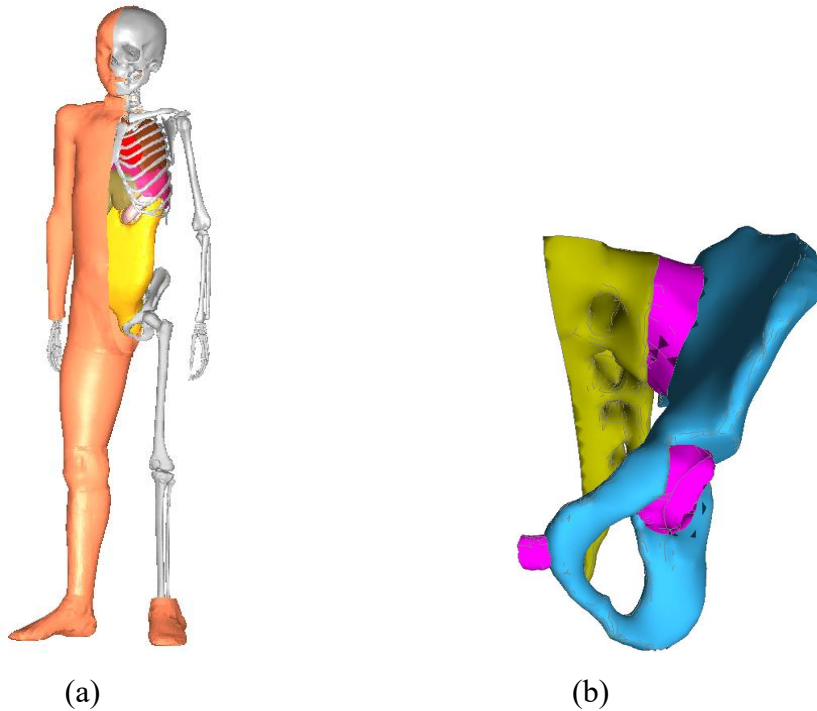


Figure 4-2: Overview of the geometric data of 10 YO child. The CAD was extracted and segmented from clinical images by previous study represented as 3D surfaces. (a) Whole-body CAD with some skeleton exposed, (b) a closer view of the pelvic bones and cartilages (left half)

4.2. MESH GENERATION AND MODEL INTEGRATION

The segmentation was performed using Mimics version 12.0 (Materialise, Leuven, Belgium). ANSYS ICEM CFD 12.1 (ANSYS, Canonsburg, PA) was used to create high quality hexahedral meshes. Some complex cavities of soft tissue were filled by Tetra-mesh tool in HyperMesh 10.0 (Altair, Troy, MI). The flow chart in Figure 4-3 shows the technical processes. Because the soft tissues connecting different anatomical structures such as cartilages, ligaments, and muscles (fleshes) are unclear in CT images, anatomy-related books were used to guide the modeling work (Moore et al., 2011; Ogden, 2000).

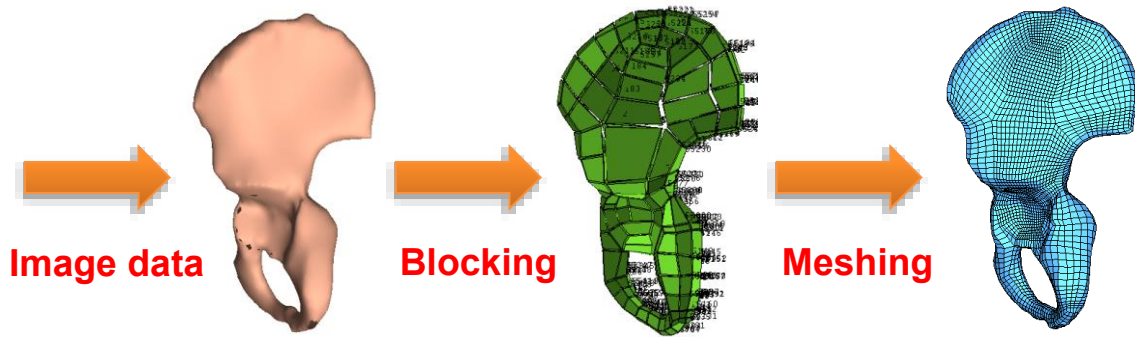


Figure 4-3: Mesh generation process: from clinical images to CAD surface, to blocks, to meshes (further refinement is not shown here)

Most of the bony structures, including cortical and trabecular bones, were modeled as hexahedral, tetrahedral or shell elements. The cortical layers at the pelvis and long bone proximal and distal ends were modeled as 3-node/4-node shell elements, with thickness scaled from adults. The fleshes in the thigh and shank were modeled as hexahedral elements. The fleshes around the pelvis, knee and ankle joints were built using tetrahedral elements. Major muscles of the lower limbs were modeled as 2-node cables, attached to the bones through tendons. Prescribed active

forces could be added in future study. The tendons and ligaments at the knee and ankle joints were modeled as membrane elements. The ligaments at the pelvic region were represented by cable elements, which only bear tensile loads. The sacroiliac (SI) joint, pubic symphysis (PS) cartilage, acetabulum cartilages and menisci were modeled using hexahedral elements. The articular cartilages at long bones were modeled as shell elements.

The criteria used to consider suitable model qualities are as follows: Jacobian larger than 0.3, aspect ratio less than 5.0 and warpage less than 50° . The minimal element size was 0.25 mm, which resulted in a time step of 6.2×10^{-5} ms. An overview of the baseline model is shown in Figure 4-4.

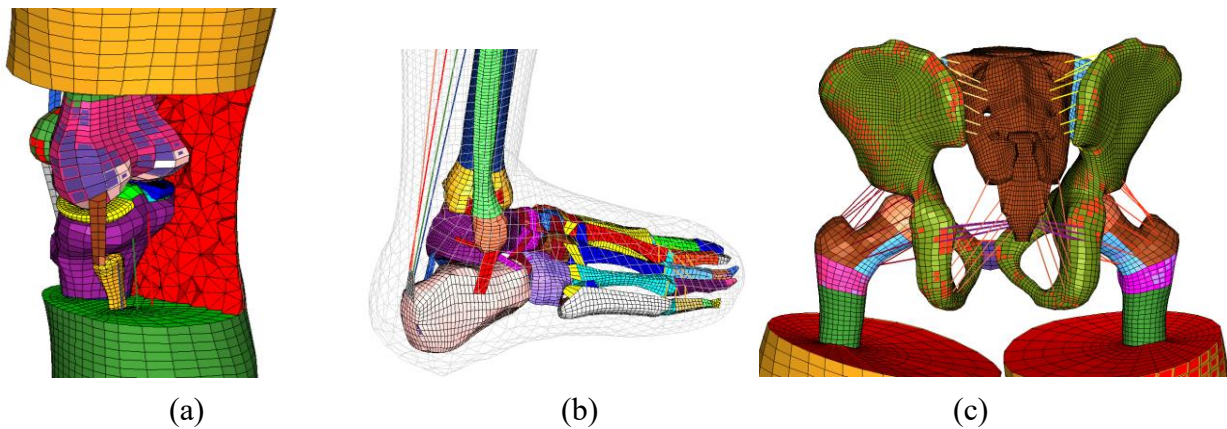


Figure 4-4: Three key regions of the 10 YO PLEX FE model: (a) Knee region (capsule and part of flesh is hidden for better view); (b) Foot & ankle region; (c) Pelvis region (rear view with pelvic flesh and fat hidden)

4.3. PLEX BASELINE MODEL VALIDATION

To assure the PLEX baseline model is a reasonable representation of 10 YO children, it needs to be generally validated and verified, so that the model would be appropriate for further upgrade (by embedding GPs) and other applications. The validations were done against the available

pediatric PMHS test data and the scaled results from some adult PMHS experimental studies. In following sections, the finished model validations are introduced briefly. In addition, the scaling law issue is addressed to transform the adult test results for the 10 YO modeling purpose.

4.3.1. Validation overview

Two levels of simulations were conducted using LS-DYNA (v.971, R 4.2, Livermore Software Technology Corporation, Livermore, CA) to validate the model. At the component level, the femur, tibia, fibula, pelvic ring and knee models were validated against data obtained from experiments under dynamic or quasi-static loading conditions. At the assembly level, the shank, thigh and pelvis-hip (sitting posture) and whole-body models, where flesh was included, were validated in lateral impacts. Experimentally available loading cases used for validations, as summarized in Table 4-2, are mainly in the lateral direction, constituting the largest portion of pedestrian impacts.

It should be noted that, for the validation cases against the results of pediatric subjects, the GP effects were assumed minor. This assumption might not be correct in the pelvis-plate impact (case 6). For the validation cases against adult data, the effect of GP was not considered since this type of structure is already calcified in an adult skeleton. As a result, the validations would be treated as preliminary ones to establish a reasonable baseline model and a good foundation for future upgrading. In the late stage of the dissertation study, the effects of the embedded GPs will be investigated in parametric studies.

Table 4-2: Loading conditions and scaling methods for model validation

No	Loading scenario	Loading direction	Loading speed	Subject	References	Scaling method
1.1	3-point bending @Femur/Tibia	A-P*	8.33 mm/s	6, 7.5, 12 YO	Ouyang et al. (2003a)	Scaling of the children experiments
1.2	3-point bending @Fibula	L-M	8.33 mm/s	6, 7.5, 12 YO	Ouyang et al. (2003a)	Scaling of the children experiments
2	Ball impact @Pelvic ring	L-M	4 m/s	Adults	Guillemot et al. (1997)	Enlarge the 10 YO geometry
3	Knee MCL** tension	Axial	0.1mm/s	Adults	Puso and Weiss (1998); Untaroiu et al. (2005)	Same material, same elongation ratio as adults
4	3-point bending @Thigh & Shank	L-M	1.5 m/s	Adults	Kerrigan et al. (2004)	Scaling of the adults experiments
5	4-point bending @Knee complex	L-M	1°/ms	Adults	Bose et al. (2004)	No scaling or new law to develop
6	Plate side impact @Pelvis-Hip	L-M	7.5 m/s	5 pediatric PHMS (5-12)	Ouyang et al. (2003b)	No scaling or new law to develop
7	Car to whole-body	L-M	10 m/s	10 YO MADYMO	New Multi-body simulation	MADYMO/Scale to generate 10 YO MADYMO model

*A-P direction adopted because there was no lateral bending test on pediatric PMHS

** MCL: medial collateral ligament

4.3.2. Scaling laws for model validation

Since the PMHS impact biomechanics tests for children are rare and not sufficient for model validation, some scaling techniques are needed to transform the existing adult cadaveric test data for indirect comparisons of the responses.

A number of scaling concepts currently exist. For example, geometric scaling (i.e. to enlarge or downsize the anthropometric dimensions), mechanical properties scaling (e.g. for cortical bone, the Young's modulus of 10 YO child is around 85.4% of an average adult's), test condition scaling (e.g. sled velocity, pendulum mass) and test response scaling (e.g. peak force, deflection history, and bending moment corridor). In this section, the scaling law for transforming the responses is the focus.

In the literature, some scaling laws had been developed to transform the mechanical and kinematic responses (e.g. force, deflection, acceleration) in specific loading conditions. For example, a human body moves to a fixed target (e.g. PMHS sled test) or a pendulum strikes an unconstrained body (Irwin and Mertz, 1997; Irwin et al., 2002). These two common loading conditions are of major interest in automotive industry. The scaling formulas for force, deflection, acceleration etc. are listed in Table 4-3.

Table 4-3: Formulas for impact response transformation ratios (Irwin et al., 2002)

	Sled and Drop Tests	Pendulum Tests
Force	Neck A-P Shear: $R_{F_x} = \lambda_v \sqrt{\lambda_{x \text{ neck}} \lambda_{m \text{ head}}}$ Neck Lat. Shear: $R_{F_y} = \lambda_v \sqrt{\lambda_{y \text{ neck}} \lambda_{m \text{ head}}}$ Neck Tension: $R_{F_z} = (\lambda_v)^2 \lambda_{m \text{ head}} / \lambda_{z \text{ neck}}$ Load Plates: $R_F = \lambda_v \sqrt{\lambda_{mt} \lambda_k}$	Torso Forces: $R_F = \lambda_v \sqrt{\lambda_{me} \lambda_k}$
Deflection	Torso Defl.: $R_d = \lambda_v \sqrt{\lambda_m / \lambda_k}$	Torso Defl.: $R_d = \lambda_v \sqrt{\lambda_{me} / \lambda_k}$
Acceleration	Head Impact: $R_{ah} = \lambda_v / \lambda_{k y \text{ head}}$ Head Lateral Non-impact: $R_{ahy} = \lambda_v \sqrt{\lambda_{k Mx} / \lambda_{m \text{ head}}}$ Head Vertical Non-impact: $R_{ahz} = (\lambda_v)^2 / \lambda_{z \text{ neck}}$ Torso: $R_{at} = \lambda_v \sqrt{\lambda_k / \lambda_{mt}}$	Torso Accel.: $R_{at} = \lambda_v \sqrt{\lambda_{me} \lambda_k} / \lambda_{mt}$
Time Period	Max. Head Excursion Period: $R_{th} = \sqrt{\lambda_{m \text{ head}} / \lambda_{k Mx}}$ Force-time Period: $R_t = \sqrt{\lambda_{mt} / \lambda_k}$	Torso Period: $R_t = \sqrt{\lambda_{me} / \lambda_k}$
Neck Moment	$R_{Mx} = \lambda_v \sqrt{\lambda_{y \text{ neck}} \lambda_{m \text{ head}}} \lambda_{z \text{ head}}$ $R_{My} = \lambda_v \sqrt{\lambda_{x \text{ neck}} \lambda_{m \text{ head}}} \lambda_{z \text{ head}}$ $R_{Mz} = \lambda_v \sqrt{(\lambda_{y \text{ neck}})^3 \lambda_{m \text{ head}}}$	$R_{Mtp} = (\lambda_{y \text{ neck}})^3$
Neck Angle	Flexion: $R_\theta = \lambda_v \sqrt{\lambda_{m \text{ head}} / \lambda_{k Mx}} / \lambda_{z \text{ neck}}$ Twist: $R_\theta = \lambda_v \sqrt{\lambda_{Iz} / \lambda_{k Mz}} / \lambda_{x \text{ head}}$	Lat. Flexion: $R_{\theta p} = \lambda_{z \text{ neck}} / \lambda_{y \text{ neck}}$
Head Excursion	See Figure 1 Chordal Disp.: $R_{\delta c} = \lambda_v \sqrt{\lambda_{m \text{ head}} / \lambda_{k Mx}}$ Chordal Angle: $R_{\theta c} = \lambda_v \sqrt{\lambda_{m \text{ head}} / \lambda_{k Mx}} / \lambda_{z \text{ neck}}$	

1. Velocity Scale Factor of the test condition, $\lambda_v = v_i / v_{\text{mid male}}$.
2. Equivalent Mass Scale Factor, λ_{me} , for pendulum tests is defined as,

$$\lambda_{me} = (\lambda_m \lambda_{mp}) / \lambda_{ms}$$

where λ_{mp} is the ratio of pendulum mass used
 λ_{ms} is the ratio of sums of masses

$$\text{for shoulder \& thorax: } \lambda_{ms} = \frac{(m_{ut} + m_p)_i}{(m_{ut} + m_p)_{50th}}$$

$$\text{for pelvis: } \lambda_{ms} = \frac{(m_{it} + m_{le} + m_p)_i}{(m_{it} + m_{le} + m_p)_{50th}}$$

Because the boundary conditions for validations in this study were not the same as those in

Table 4-3, the laws listed were not applicable. Therefore, new scaling strategy was developed in

this dissertation based on a long bone 3-point bending scenario. There were several assumptions: there is geometric similarity between human subjects with different age (e.g. 10 YO child vs. adult), the cross section of a long bone shaft is a circular ring, and the material is linear-elastic with a constant Young's modulus (E). Based on the formulas of deflection for a beam in 3-point bending and the cross-sectional moments of inertia of a tube (Young and Budynas, 2002), the equation for ultimate bending force (F_{max}) at small deflection for a slender circular tube can be expressed as below:

$$F_{max} = \frac{\pi}{16L} D^3 (1 - \alpha^4) \sigma_s \quad 4-1$$

Here L is the span of two roller bases, d and D is the inner and outer diameter of the cross section, α is the ratio of the two diameters (d/D) and σ_s is the ultimate tensile stress of the material. Accordingly, the ratios of these parameters are λ_L , λ_D and λ_{σ_s} . The ratios of inner/outer diameter are assumed to stay unchanged for different samples, because of geometric similarity. The derived scale factors for ultimate force (F_{max}) and moment (M_{max}) are labeled as λ_F and λ_M respectively.

$$\lambda_F = \lambda_{\sigma_s} \times \lambda_D^3 / \lambda_L \quad 4-2$$

For the bending moment, the ultimate value is proportional to $L \times F_{max}$. As a result,

$$\lambda_M = \lambda_{\sigma_s} \times \lambda_D^3 \quad 4-3$$

Strictly speaking, the loading conditions for thigh and shank bending cases are not identical to the above single bone bending, but with the absence of more robust scaling laws, Equations 4-1 to 4-3 were still applied. According to Mertz et al. (2001), the dimension ratios at anterior-

posterior (λ_x) and lateral-medial (λ_y) directions are the same for lower limbs, thus the cross-sectional dimension scale factors $\lambda_D = \lambda_x = \lambda_y$, and Equation 4-3 is changed to

$$\lambda_M = \lambda_{\sigma_s} \times \lambda_x^3 \quad 4-4$$

The scaling method developed in this study, as derived in Equations 4-1 to 4-3, had several assumptions. For practical long bone bending simulations, the validity of the scaling law needs to be checked. An auxiliary parametric study was performed on 3-point bending test on a femur to address this issue. The baseline FE model was from the current 10 YO PLEX model, and the loading was in anterior-posterior direction. Based on Equation 4-2, assuming $\lambda_{\sigma_s} = 1$, if the length stays the same, $\lambda_F = \lambda_D^3$; if the outer diameter stays the same: $\lambda_F = 1/\lambda_L$. The simulation results were plotted as scattered dots, which were found well matching the predicted curves, as shown in Figure 4-5 (a). Therefore, the validity of Equation 4-2 was verified in a certain range in the scenario of long bone 3-point bending.

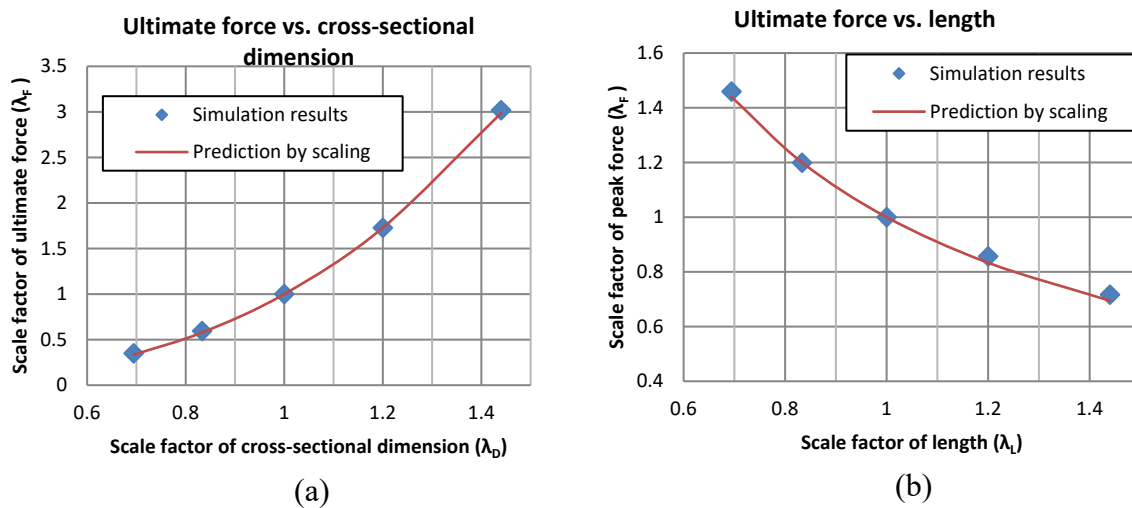


Figure 4-5: The comparison of simulation results and prediction curve: (a) Ultimate bending force vs. cross-sectional dimension; (b) Ultimate bending force vs. span/sample length

4.3.3. Validation summary

Long bone 3-point bending

In 2003, Ouyang et al. conducted a series of 3-point bending experiments on long bones from 11 child subjects aged from 2 to 12 years of age (Ouyang et al., 2003a). Three subjects (6, 7.5 and 12 YO) were closest in age, height and weight to the 10 YO model. Consequently, experimental data obtained from these specimens are selected for model validation. The higher loading rate of 8.33 mm/s is chosen. It was noticed that the sizes of the three subjects were different from an average 10 YO child, so the scaling law proposed in Equation 4-2 was applied. It was further assumed that, for subjects with close age, the bone strength stayed unchanged ($\lambda_{\sigma_s} = 1$) and the dimension ratios of the diameter (λ_D), length or span (λ_L) and standing height (λ_H) were all the same ($\lambda_D = \lambda_L = \lambda_H$), and could be calculated by dividing subject's height to the height of the current 10 YO model (1401 mm). The descriptions of subjects and the scaled test results are listed in Table 4-4.

Table 4-4: Subjects information and scaling of test results, originally reported by Ouyang et al. (2003a)

ID	Age (Years)	Height (mm)	Ultimate bending force F (N)					
			Test results			Scaled to 10 YO		
			Femur	Tibia	Fibula	Femur	Tibia	Fibula
2	7.5	1170	1109	951	171	1590	1364	245
11	6.0	1090	1459	1214	201	2410	2006	332
12	12.0	1400	1249	995	325	1251	996	325
Average						1750	1455	301
Standard Deviation						596	511	48

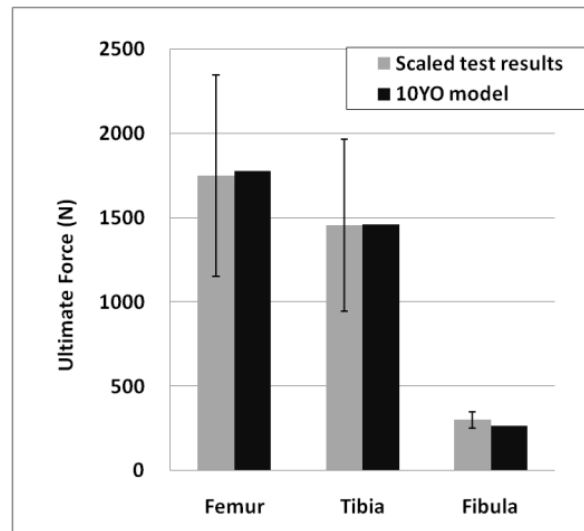


Figure 4-6: Simulation results of 3-point bending tests on long bones, compared to scaled data from Ouyang et al. (2003a)

The average ultimate forces for femur, tibia and fibula from scaled test data are respectively 1750 N, 1455 N, and 301 N. The validation results are shown in Figure 4-6 in a bar chart exhibiting a good agreement between the simulated results of this 10 YO model and scaled test results.

Pelvic ring lateral impact

Guillemot et al. (1997) conducted lateral impact tests on 12 adults' pelvic rings (impact at acetabulum). A literature search revealed that no similar test on 10 YO PMHS existed for a direct validation. Additionally, there was no simple scaling law to transform the corridor of adults to that of children, given a complex geometry like pelvis in a semi-constrained loading condition. Therefore, a strategy similar to the study by Jebaseelan et al. (2010) on pediatric lumbar spine was used. The pelvic bones with attached ligaments were scaled up to the adult size, using dimensional ratios of 1/0.723 at horizontal direction, 1/0.793 at vertical direction (Mertz et al., 2001).

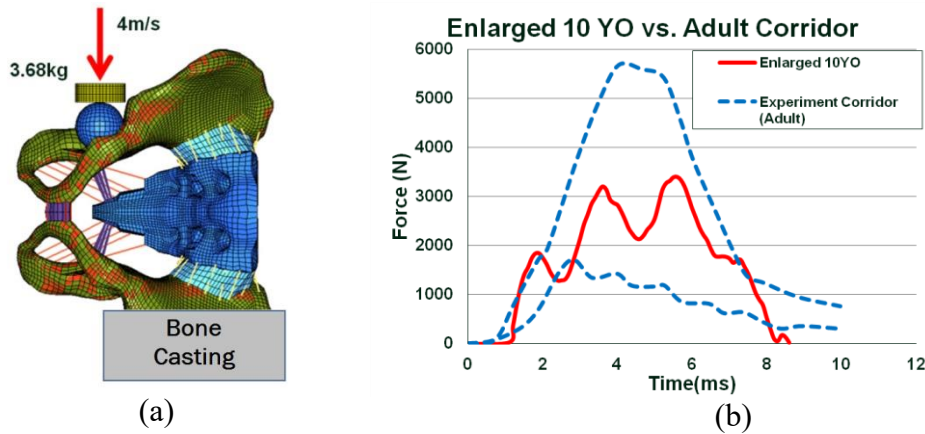


Figure 4-7: Pelvic ring lateral impact validation. (a) Simulation setup; (b) Simulation results compared with the experimental results originally from Guillemot et al. (1997)

Figure 4-7 (a) shows the enlarged 10 YO pelvic ring sub-model under the identical loading conditions as in Guillemot et al. (1997), where a 3.68 kg impactor hit the steel ball at a speed of 4 m/s. The ball was resting in the acetabulum for load distribution. A solid base was used to fix the collateral iliac wing and support the pelvic ring. Figure 4-7 (b) shows that, the simulated response of the enlarged 10 YO model falls within the corridor of adult data with a similar trend.

Knee MCL tension

Among the knee ligaments, the medial collateral ligament (MCL) gains the most attention in pedestrian impacts. A MCL unit tension simulation was conducted and the result was compared with the adult data to affirm the ligament behaves reasonably. The tensile experiment referred to Untaroiu et al. (2005) and the setup is shown in Figure 4-8 (a). The material property was assumed unchanged for the child MCL ligament as no further detailed age related information was available. The adult MCL ligament material property was referred to Puso and Weiss (1998), and the corridor of stress-strain curves was plotted in Figure 4-8 (b). In this model, the Young's modulus was 222

MPa. The failure point is 16.3% strain, or 36 MPa tension stress accordingly, marked in Figure 4-8

(b).

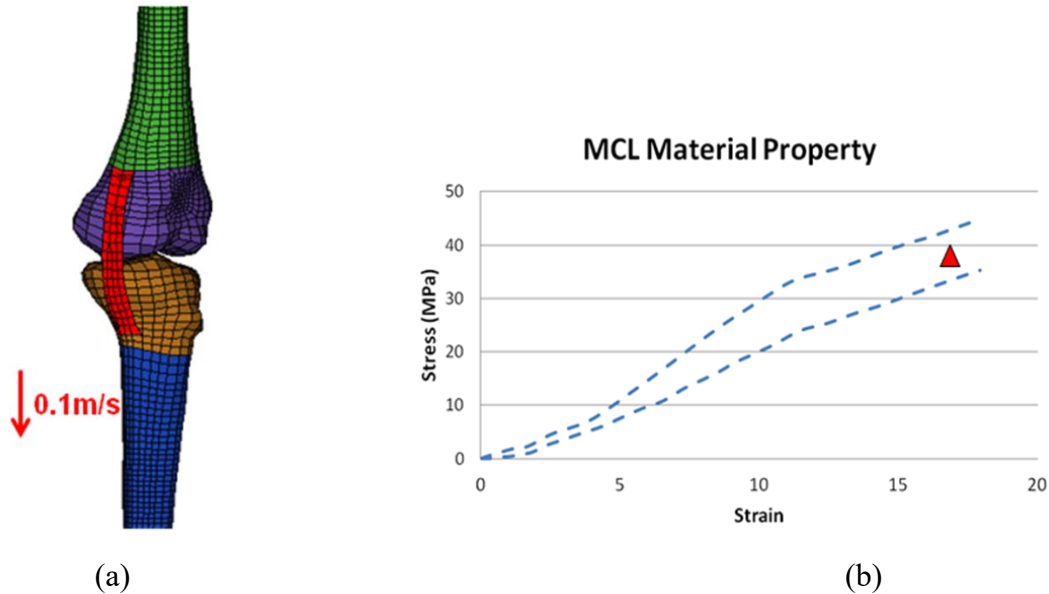


Figure 4-8: MCL tensile test: (a) Simulation setup; (b) Corridor of adult MCL material property in a stress-strain plot, originally reported by Puso and Weiss (1998)

Thigh and shank dynamic 3-point bending

The thigh and shank dynamic 3-point bending experiments were conducted on adult subjects by Kerrigan et al. (2004). The predicted failure moments at the mid-shaft sites of the thigh and the shank with 50% risk were, respectively, 447 Nm and 312 Nm, at the loading speed of 1.5 m/s. The simulation sub-models are shown in Figure 4-9.

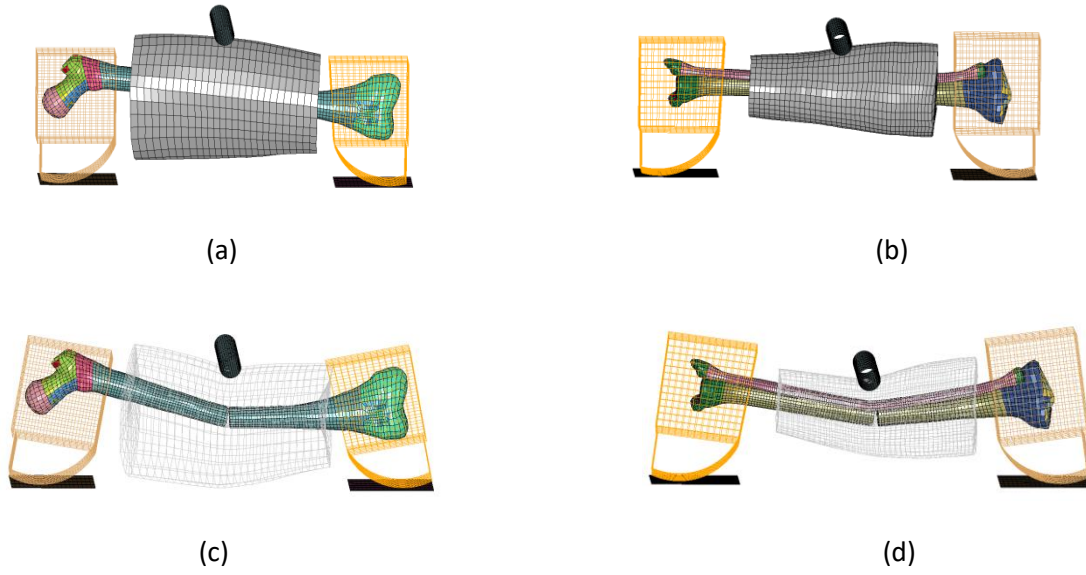


Figure 4-9: The validation thigh and shank: (a) & (b) Before loading; (c) & (d) After failure

Equation 4-4 was used to scale the adults' responses to those of 10 YO child. In the current 10 YO FE model, the elastic modulus for the long bone is 85.4% of that of adults' (Mertz et al., 2001). However, for a piecewise elastic-plastic material model, if the yield stress, tangent modulus (for plastic yielding) and ultimate strain stay the same, the difference of ultimate stress between the 10 YO model and adults is very small (i.e. $\lambda_{\sigma_s} \approx 1$). The validation results are shown in Table 4-5, demonstrating a good matching for the thigh, while acceptable for the shank. One possible explanation is the complex cross-sectional shape of the shank may weaken the accuracy of scaling law in Equation 4-4.

Table 4-5: Scaling of adult results for 10 YO model validation

Thigh (moment unit: Nm)					Shank (moment unit: Nm)				
Adult M_{\max}	λ_x	Scaled M_{\max}	10 YO Model simulation	Error	Adult M_{\max}	λ_x	Scaled M_{\max}	10 YO Model simulation	Error
447	0.703	155.3	148.8	-4.2%	312	0.657	88.5	108.3	+22.4%

Knee 4-point bending

The ligament rupture caused by lateral bending is a main mechanism of knee injury for pedestrians in car-to-pedestrian impacts. Thus the behavior of the knee joint of the 10 YO model in lateral dynamic bending was compared with the results of adult PMHS conducted by Bose et al. (2004). The test setup is shown in Figure 4-10 (a), where all the movements are restricted in the coronal plane. One pin joint is mounted at the proximal side with a longitudinal sliding degree of freedom, to achieve the simply-supported boundary conditions. The bending angular velocity is $1^\circ/\text{ms}$. The adult corridor of bending moment - bending angle curves is shown in Figure 4-10 (b). The average failure point for the adults is also marked, with a bending moment of 120 Nm and bending angle of 13.5° . The simulated failure point is reasonable qualitatively.

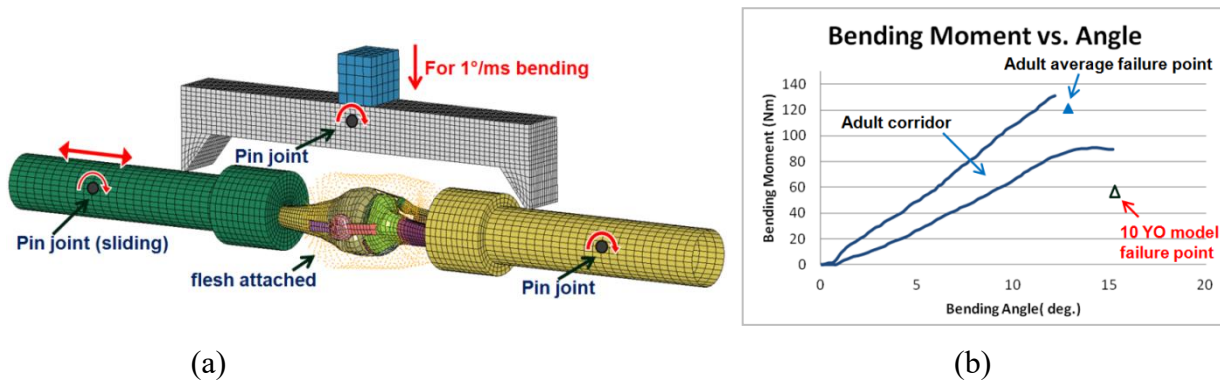


Figure 4-10: Knee lateral-medial 4-point bending (a) Simulation setup; (b) Adult test results in bending moment - bending angle plot, originally from Bose et al. (2004)

Pelvis lateral plate impact

Based on the same PMHS for the study of long bones used in Ouyang et al. (2003a), Ouyang et al. investigated the pelvis responses of subjects divided into younger (2-4 YO) and older (5-12

YO) groups under lateral plate impact (Ouyang et al., 2003b). The force-displacement response corridor of the older group was utilized to validate the 10 YO model. In the experiment, a cadaver was set in a sitting posture on a friction-free surface with the legs at a natural vertical position. The 10 YO model was accordingly positioned to a sitting posture. The simulation setup followed Ouyang's test, as illustrated in Figure 4-11 (a). The simulated curve fit the corridor well, as shown in Figure 4-11 (b). There was no fracture observed in the simulation, which is found to be consistent with the experimental results, thus achieving the 10 YO model validation target.

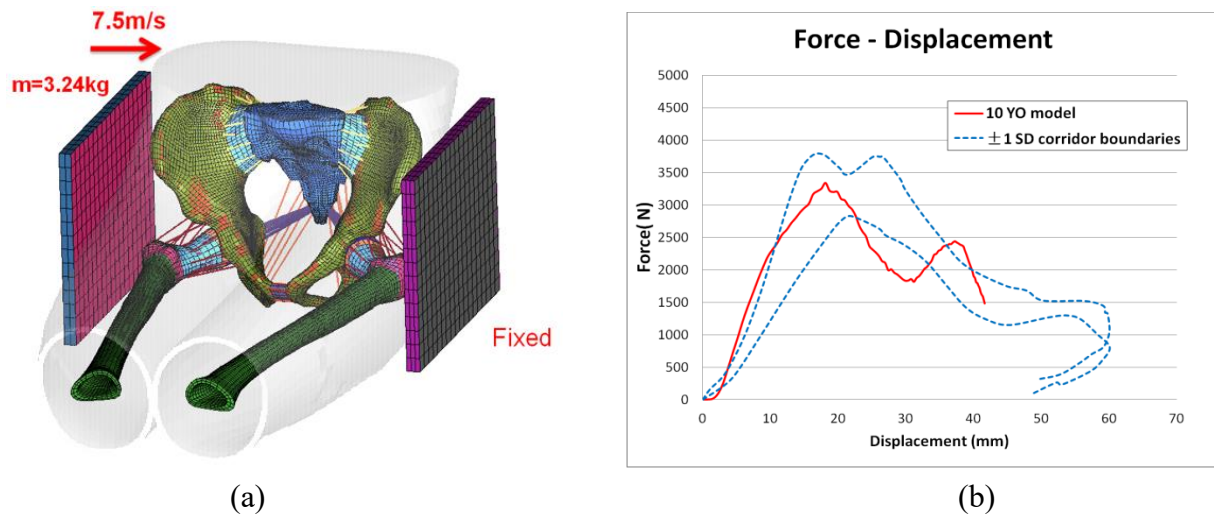














Figure 4-11: Pelvis lateral impact, (a) Simulation setup; (b) Simulation result compared to the corridor of experimental results of 5-12 YO children, originally from Ouyang et al. (2003b)

Whole-body model simulation

The PLEX FE model was integrated with the previously developed thorax, head and neck FE sub-models for a 10 YO child (Dong et al., 2013; Jiang et al., 2014) to simulate the sedan-to-pedestrian impact. An FE model of a small sedan was obtained from the National Crash Analysis

Center (NCAC) website. This car model was then simplified and only the front portion including the front bumper, hood etc. was used. A constant speed of 10 m/s (36 km/h) was assigned to the car that hit the standing pedestrian in the lateral direction as illustrated in Table 4-6.

Table 4-6: Sedan-to-pedestrian impact simulations using MADYMO dummy model (scaled from adult pedestrian model to 10 YO), published as Shen et al. (2015a)

Model	0 ms	20 ms	40 ms
10 YO FE pedestrian model			
10 YO MADYMO model (Scaled from adult model)			
Model	60 ms	80 ms	100 ms
10 YO FE pedestrian model			
10 YO MADYMO model (Scaled from adult model)			

MADYMO (v.7.5) (TASS, Helmond, the Netherlands) was used for multi-body model development and impact simulation. The 50th percentile MADYMO ellipsoid pedestrian model (v. 5.0) was taken as the baseline model. MADYMO/Scaler, based on GEBOD population (TASS

International, 2014), was used to scale the MADYMO baseline model to a 10 YO multi-body model with the same height and weight of 10 YO child (1401 mm and 35.0 kg) used in this study. Using coupling FE-multi-body version of MADYMO, the same car FE model, initial positioning and impact speed used in FE pedestrian simulation were adopted in the simulation using 10 YO MADYMO scaled model. The kinematic response of the whole-body 10 YO model was compared to the multi-body simulation results, as shown in Table 4-6. The kinematics histories were similar. The initial head contacts occur at 85 ms and 84 ms at speeds of 7.8 m/s and 8.0 m/s in the two simulations. This comparison demonstrates that the 10 YO model is robust with a reasonable agreement in overall kinematic behavior, although there are a number of limitations in this semi-quantitative validation.

Later the whole-body pedestrian model was further postured to represent a seated 10 YO child, and these two whole-body models were named Collaborative Human Advanced Research Model-10 years (CHARM-10), pedestrian and occupant models, respectively). More details about the integration and whole-body models verifications were published in Shen et al. (2016).

4.3.4. Material properties of PLEX

The material properties of the preliminarily validated PLEX model agreed with those published literature, shown in Table 4-7. The scaling factor of the Young's modulus for long bones of the 10 YO child was set as 0.854, which was suggested by Mertz et al. and Irwin et al. while scaling Hybrid III dummies for additional anthropometric groups (Irwin et al., 2002; Mertz et al., 2001).

Table 4-7: Main material properties of 10 YO PLEX FE model, with the relevant references given accordingly

Component	Material Model	Material Parameters	Reference
Cortical at long bones	Elastic-Plastic	$\rho=2.0 \times 10^3 \text{ kg/m}^3$, $\gamma=0.3$, E and σ_Y for different regions of femur: Shaft: 12.8 GPa, 120 MPa; Neck: 8.54 GPa, 77 MPa; Head 0.854 GPa, 7.7 MPa E and σ_Y for Tibia: 14.9 GPa, 125 MPa $\epsilon_{\max}=0.02$	Takahashi et al. (2000); Untaroiu et al. (2005)
Cortical at pelvis	Elastic-Plastic	$\rho=2.0 \times 10^3 \text{ kg/m}^3$, $\gamma=0.3$, E=12.24 GPa, $\sigma_Y=150 \text{ MPa}$ $\epsilon_{\max}=0.027$	Kim et al. (2013)
Trabecular at long bones	Elastic-Plastic	$\rho=1.1 \times 10^3 \text{ kg/m}^3$, $\gamma=0.3$, E and σ_Y for different regions of femur: Head: 0.77 GPa, 9.3 MPa; Proximal: 0.53 GPa, 6.6 MPa; distal: 0.25 GPa, 5.6 MPa For Tibia: 0.38 GPa, 5.3 MPa $\epsilon_{\max}=0.134$	Takahashi et al. (2000); (Untaroiu et al., 2005)
Trabecular at pelvis	Elastic-Plastic	$\rho=1.1 \times 10^3 \text{ kg/m}^3$, $\gamma=0.2$, E=0.0448 GPa, $\sigma_Y=7.5 \text{ MPa}$ $\epsilon_{\max}=0.25$	Kim et al. (2013)
SI joint & acetabulum cartilage	Hyperelastic	$\rho=1.2 \times 10^3 \text{ kg/m}^3$, $\gamma=0.495$, Mooney-Rivlin parameters: $C_1=2.87 \text{ MPa}$, $C_2=0.278 \text{ MPa}$	Anderson et al. (2005); Kim et al. (2013)
PS cartilage	Hyperelastic	$\rho=1.2 \times 10^3 \text{ kg/m}^3$, $\gamma=0.495$, Mooney-Rivlin parameters: $G=0.5 \text{ MPa}$, $C_{10}=0.05 \text{ MPa}$, $C_{01}=0.2 \text{ MPa}$, $C_{11}=0.25 \text{ MPa}$	Li et al. (2006)
Articular cartilage	Elastic	$\rho=1.2 \times 10^3 \text{ kg/m}^3$, $\gamma=0.2$, E=0.17 GPa	Froimson et al. (1997); Yue et al. (2011)
Knee ligaments	Elastic	$\rho=1.2 \times 10^3 \text{ kg/m}^3$, $\gamma=0.45$, E=0.222 GPa, $\sigma_Y=36.4 \text{ MPa}$	Puso and Weiss (1998); Untaroiu et al. (2005)
Pelvis ligaments	Discrete beam	Hip joint (14 beams each side): K=34 N/mm, A:13.4 mm ² SI joint (16 beams each side): K=149 N/mm, A:12.8 mm ²	Bechtel (2001); Hewitt et al. (2001)
Skin	Elastic	$\rho=1.0 \times 10^3 \text{ kg/m}^3$, $\gamma=0.45$, E=0.001 GPa	Pailler-Mattei et al. (2008); Yue et al.

			(2011)
Flesh for pelvis	Viscoelastic	$\rho=1.05 \times 10^3 \text{ kg/m}^3$, $\gamma=0.495$, Mooney-Rivlin parameters: $C_1=21.5 \text{ kPa}$, $C_2=6.37 \text{ kPa}$ $G_1=1.72 \text{ kPa}$, $G_2=7.53 \text{ kPa}$ $\beta_1=0.54$, $\beta_2=0.06$	Kim et al. (2013)
Flesh for limbs	Hyper-elastic	$\rho=1.05 \times 10^3 \text{ kg/m}^3$, loading curve from THUMS model	
Subcutaneous fat	Viscoelastic	$\rho=1.0 \times 10^3 \text{ kg/m}^3$, $\gamma=0.495$, Mooney-Rivlin parameters: $C_1=6.33 \text{ kPa}$, $C_2=1.58 \text{ kPa}$ $G_1=0.5 \text{ kPa}$, $G_2=2.2 \text{ kPa}$ $\beta_1=0.54$, $\beta_2=0.06$	Kim et al. (2013)

Notes: ρ : density, γ : Poisson ratio, σ_Y : Yield stress, E : Young's modulus, ϵ_{\max} : Ultimate strain, K : Spring constant (N/mm), A : Cross-sectional area (mm^2).

4.4. CHAPTER SUMMARY

In this chapter, the PLEX FE model of a 10 YO child was established. The validations of the biofidelity were conducted on component level and sub-assembly level. In addition, the PLEX was integrated with the other body parts and composite of the whole-body model, and the sedan-to-pedestrian impact was simulated using this model. The simulation results showed reasonable agreements with those from experiments or comparable digital models. Therefore, the PLEX model was treated as limited validated and can be used for further applications.

CHAPTER 5. LITERATURE REVIEW OF GROWTH PLATE

GP is considered as a remarkable immature feature in children compared to adults. In this chapter, the anatomy of GP is first reviewed. A summary of investigations on the existing experimental studies on human and animal GPs is presented.

5.1. GROWTH PLATE ANATOMY

GPs lie at the ends of long bones and the junctions of some flat bones (e.g. pelvic bones, skull bones). Within the GP, chondrocytes undergo processes of differentiation (Flynn et al., 2014). It should be noted that a GP is actually not a simple flat plate. It can be seen in Figure 5-1 (a) that there is a quadrinodal interface (four protrusions at four quadrants), which is a 3D presentation of the waved curvature previously shown in the X-ray image of Figure 1-2. Looking more closely using histology reveals more unevenness and ruggedness. A histology photo of femoral head GP section shown in Figure 5-1 (b) is an example. This highly irregular morphology of GP from macroscopic to microscopic scale shows micro engagements, which make the structure much stronger than a simply flat interface, especially in shearing loads (Kandzierski et al., 2012; Peterson, 2007).

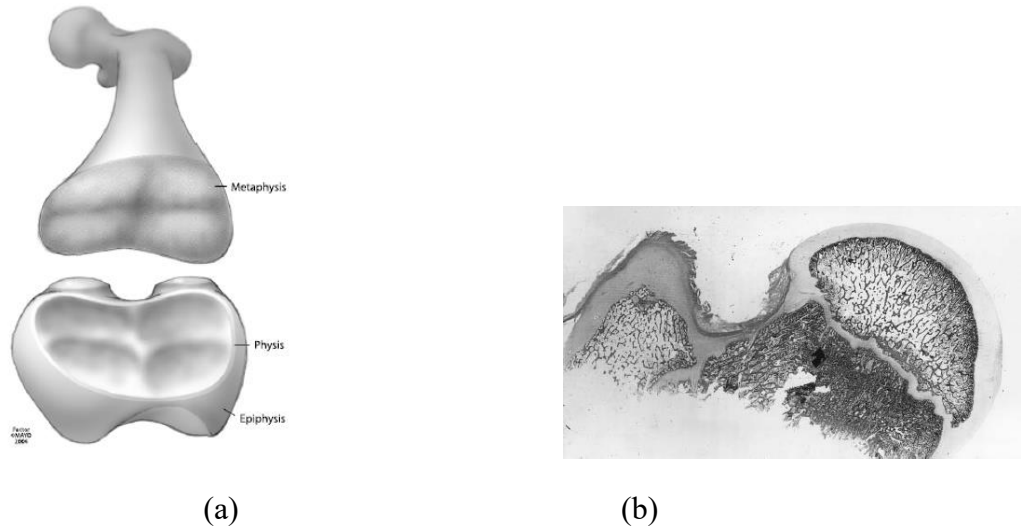


Figure 5-1: Growth plate anatomy. (a) Schematic diagram of distal femoral GP (Peterson, 2007); (b) Histological section picture of the femoral head from an 8 YO girl (Ogden, 2000)

Figure 5-2 shows a stained histological micrograph of a rat proximal tibia GP (Villemure and Stokes, 2009). It reveals that the GP consists of chondrocytes (cartilage cells) organized in columns embedded in an extra-cellular matrix. A GP can be further divided into several cellular zones with different morphologies and arrangements of cells. Typically, there are three zones: the reserve zone (smaller and flatter at epiphysis end), the proliferative zone (where the new cells are generated) and the hypertrophic zone (larger and rounder at metaphysic end). The hypertrophic chondrocytes form columns along the long axis of a bone and produce collagen, which are used subsequently for bone matrix. The growth route map follows a direction through the zones and the endochondral ossification lengthens a long bone at the longitudinal axis.

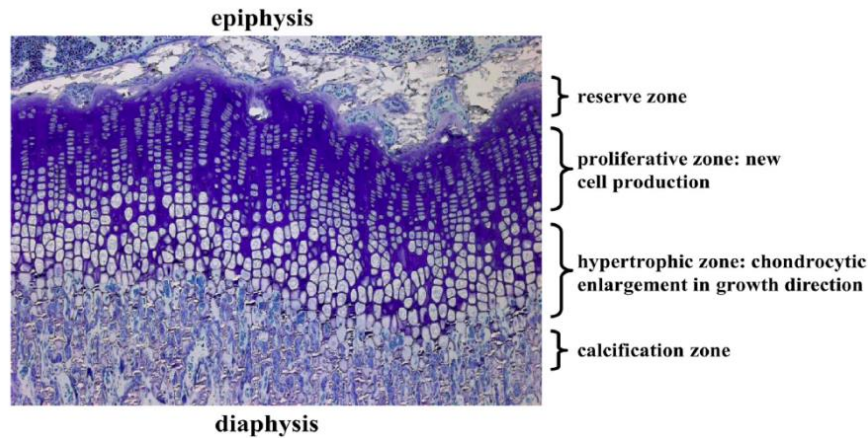


Figure 5-2: Micro-graph of a 2 μ m thick section of a rat proximal tibia GP (Villemure and Stokes, 2009)

At the early stage of the growth, GPs include two types of interface, involving the primary center of ossification (at the diaphysis with two primary physes by metaphysis) and second center of ossification (SCO, within the epiphysis), as shown in Figure 5-3 (Peterson, 2007). Along with the growth and development, the SCO expands and the epiphyseal cartilage shrinks. Its side towards diaphysis approaches the primary physis, and the spherical GP flattens and gradually becomes a contour following the primary physis (Figure 5-3, b). Similar contouring also occurs as the SCO approaches the lateral and subarticular regions of the epiphysis. Since the SCO matures earlier than the primary GP, during the late stage of childhood, only one fused physis will be observed. The primary physis also grows circumferentially. Once the SCO matures, the latitudinal growth becomes appositional and is supported by the zone of Ranvier (Peterson, 2007).

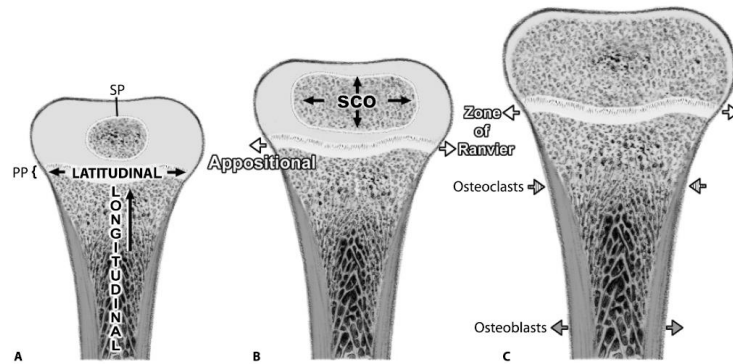


Figure 5-3: Growth patterns of a typical long bone (A) the second ossification center (SCO) surrounded by a spherical physis, secondary physis (SP); (B) the second ossification center expanded; (C) the second physis approached to primary physis and fuses to one (Peterson, 2007)

The closure ages for GPs from different sites are different. Figure 5-4 shows the closure ages for GPs at long bones of extremities. Generally speaking, the closures start from 12 years, and finish after 20 years.

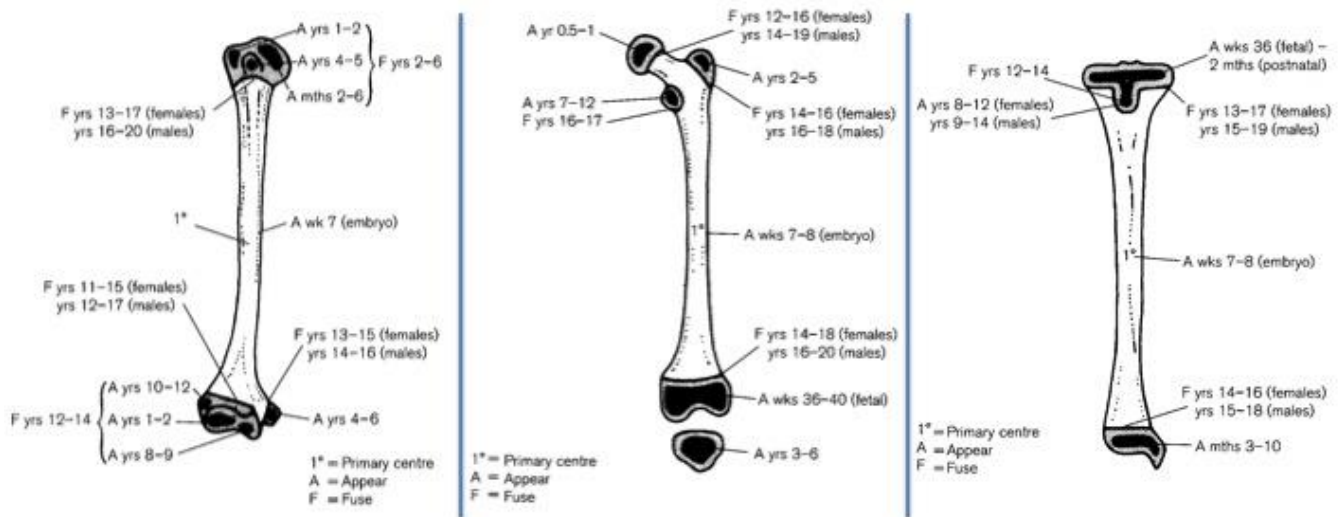


Figure 5-4: The closure ages of GPs in upper and lower extremities (Scheuer et al., 2000)

The GP at pelvis is different from the discoid GPs at lower limbs, because the pelvic bones are categorized as flat bones, rather than long bones for lower limbs. As shown in Figure 5-5, the

Y-shaped triradiate cartilage is in the connecting interfaces of three primary ossification centers on the acetabulum: the ilium, ischium and pubis. The triradiate physis therefore has three arms: one anteriorly located between the ilium and pubis, one posteriorly located between the ilium and ischium, and one vertically located between the ischium and pubis. The physis between two primary growth centers has symmetric structures and generates new osteocytes at both sides to enlarge the socket of hip joint. Its closure occurs at around 15 to 18 years of age (Peterson, 2007).

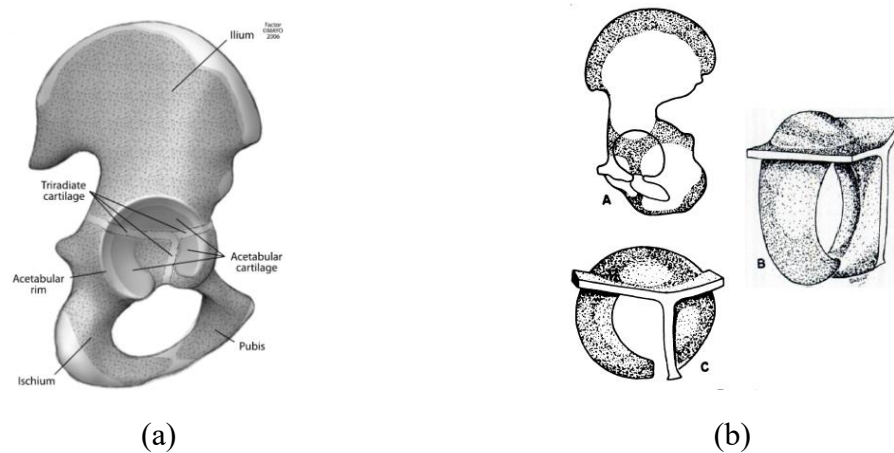


Figure 5-5: GP at pelvis: Triradiate cartilage. (a) Schematic diagram (Peterson, 2007); (b) Detailed view of triradiate cartilage (fused with acetabular articular cartilage) (Bucholz et al., 1982)

Based on anatomical reviews listed above, it could be concluded that GP is a complicated inhomogeneous structure with an irregular 3D shape. The distinct characteristics of GPs compared to trabecular, cortical bones and articular cartilages make them to be potential sources of pediatric trauma injuries.

5.2. GROWTH PLATE EXPERIMENTAL STUDIES

5.2.1. Tensile tests

The tensile tests can be divided into two categories: tests on whole bone sample with intact GP and tests on trimmed bone-GP-bone units. In the first category, most of the tests were on GPs from small animals, thus these tests did not provide much helpful information for testing GPs from larger animal such as pig. In the second category, Williams et al. (2001) conducted tensile tests on human femoral GPs using bone-GP-bone units. The specimens were taken from two subjects, aged 8 and 13 years. Each bone was cut by a diamond wheel into thin slices with dimensions around $0.51 \text{ mm} \times 2.29 \text{ mm} \times 15 \text{ mm}$. A pair of friction grips and guiding rods were used to mount the specimen as shown in Figure 5-6 (a). The loading speed was 0.0004 mm/s , i.e. a strain rate of $0.003/\text{s}$.

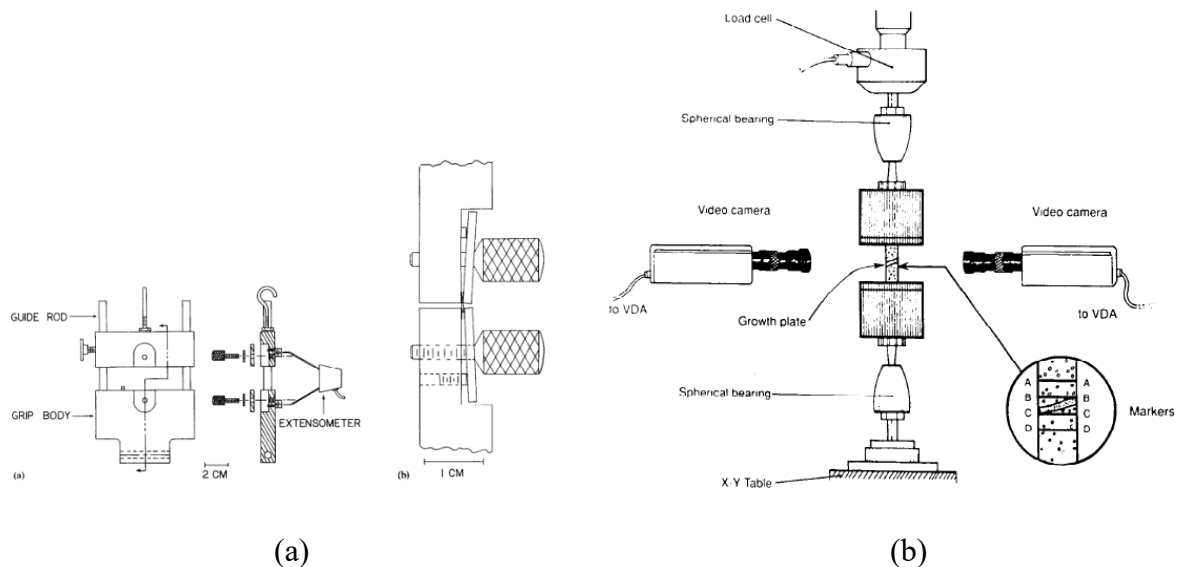


Figure 5-6: Tensile test setup examples. (a) Friction grips in Williams et al. (2001). (b) Complete setup in Cohen et al. (1992), including image tracking system

Cohen et al. (1992) carried out tensile tests on bovine distal femoral GPs (using bone-GP-bone unit) as shown in Figure 5-6 (b). The cross section was 7 mm×7 mm and the axis of the specimen was parallel to the diaphysis shaft axis. Different inclination angles were observed among specimens. However, no significant differences in the elastic modulus or ultimate stress were found for specimens with different inclinations. This phenomenon could be explained by the axial orientation of collagen fibers. An additional Video Dimension Analyzer (VDA) image tracking system was implemented to analyze the deformation distribution among the bony parts and GP. The results showed that the GP deformation accounted for the dominant portion of overall stretch, so that the surrounding bony structures could be treated as rigid parts in tensile tests.

The only tensile test on human showed an average tensile modulus of 4.26 MPa and ultimate stress of 0.98 MPa, while the ultimate strain was 31% (Williams et al., 2001). Other studies involved animal subjects, and a few of them reported the Young's modulus or elastic modulus, as summarized in Figure 5-7. The ultimate tensile stresses reported in literature are summarized in Figure 5-8. The associated information of experiments (species, anatomical site, age of test objects and reference number) is provided along the horizontal axis.

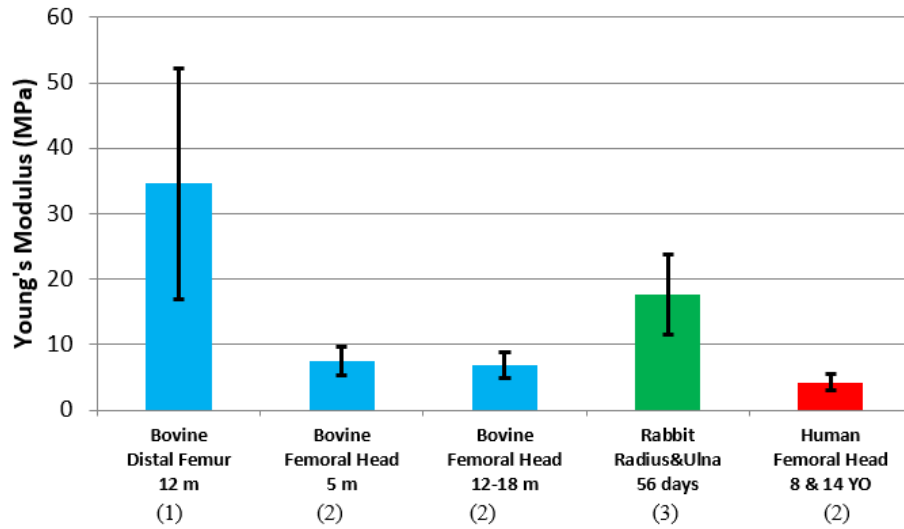


Figure 5-7: The Young's modulus of GP from tension tests. The references in order are (1) Cohen et al. (1992), (2) Williams et al. (2001), (3) Fujii et al. (2000)

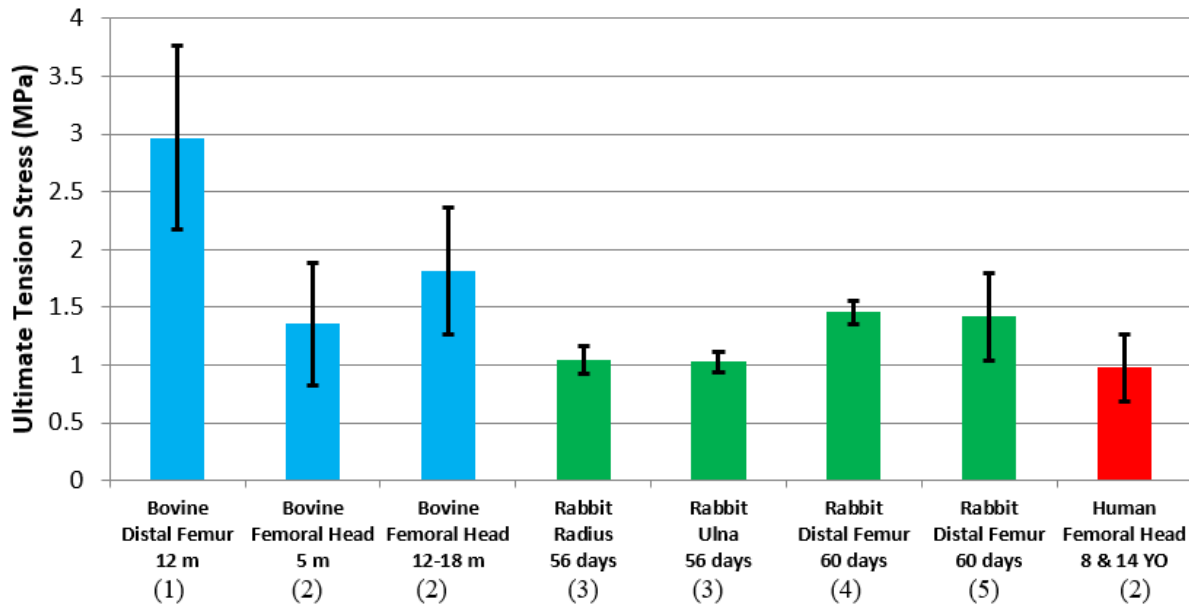


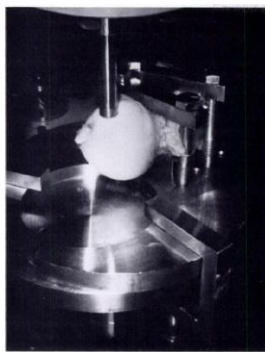
Figure 5-8: Ultimate tensile stress of GP. The references in order are: (1) Cohen et al. (1992), (2) Williams et al. (2001), (3) Fujii et al. (2000), (4) Guse et al. (1989), (5) Noble et al. (1982)

5.2.2. Shearing tests

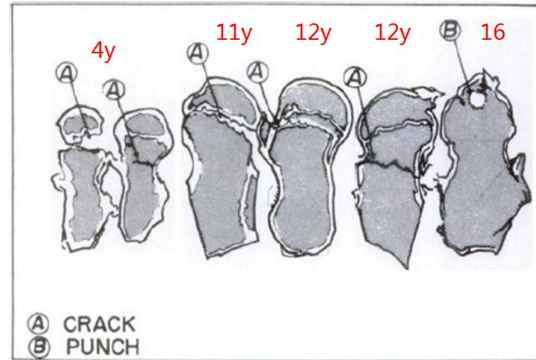
Shearing tests can also be divided into two categories, on the whole bone and on bone-GP-

bone units. Chung et al. (1976) collected 25 pairs of femora of children, aged from newborn to 15

years 10 months. The samples of proximal femur were excised and all skin and flesh were cleared within 48 hours post mortem. For discussion of the effect of the perichondrial fibrocartilaginous complex on the shear strength, the complex was removed for half of the samples, and kept for the other half as the control group. X-ray was taken before tests to confirm that there were no abnormalities in the samples. The fixture used is shown in Figure 5-9 (a). A pin was pushed from the anterior to the posterior side of the femur bone at a speed of 2 mm/min (0.033 mm/s). Each sample was loaded to failure.



(a)



(b)

Figure 5-9: Shearing test by Chung et al. (1976). (a) Experimental setup; (b) Failure patterns for different ages.

A fitting curve was drawn based on the shearing strength for the subjects with different ages, depicting the age influence on the GP strength. For the GP at the femoral head from a 10 YO child, the structural shearing strength was around 12 kg/cm² (1.20 MPa). The failure pattern also changed with age as shown in Figure 5-9 (b). For younger samples, the crack tended to happen on the femoral neck region. For the age group of 9-11 years, the separation of the GP was the main damage pattern. For the older samples, the failures tended to be punches just under the pushing

rod, rather than cracks at other sites. This study demonstrated that the failure was a combined effect of structure and material properties of GPs, cortical bone and trabecular bone and not only governed by GP material property. Therefore, this whole bone (with an intact GP embedded) test was not be mimicked in the planned tests on porcine samples to depict material properties of GP.

As mentioned in Section 5.1, a GP has connections with surrounding perichondrial and periosteum complex. The effect of surrounding soft tissues around GP needs discussion because it may provide extra strength under loading. In the series of tests, Chung et al. (1976) found that the influence of surrounding soft tissues is minor in the femoral head shear tests for children older than 10 YO.

Williams et al. (1999) used bovine proximal tibia GPs (bone-GP-bone units) to investigate the responses of GPs in shearing loads. The specimen was 6.6 mm×6.6 mm×50-80 mm along the longitudinal axis. The shear test setup and fixture is shown in Figure 5-10. The loading direction is from anterior to posterior. The two bone segments were gripped as close to the GP interfaces as possible. One end of bone was fixed to the actuator and loaded vertically, while the other end of bone was fixed to a horizontal sliding stand, which could translate along the bone axis. The effect of pre-load compressing the GP was also studied by applying a constant force onto one end of the bone, using a hanging weight.

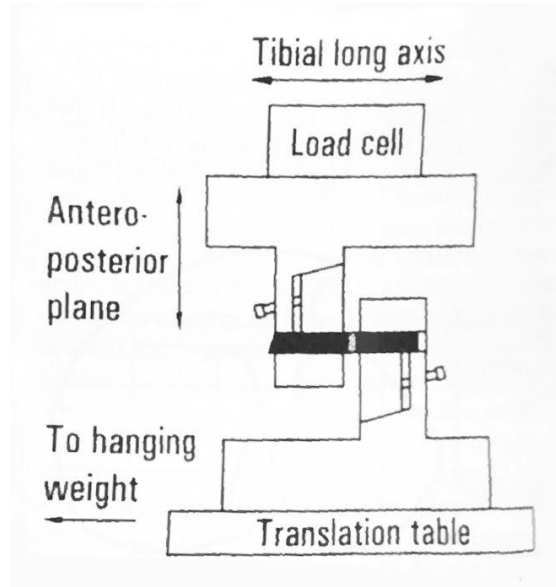


Figure 5-10: Test set-up of shearing of bone-GP-bone unit from bovine proximal tibia (Williams et al., 1999)

The mean ultimate shear stress for bovine tibia GPs was 2.14 MPa with a standard deviation of 0.64 MPa. It was found in this study that there were significant differences on shearing moduli among the different portions at the same GP (i.e. the anterior one third vs. posterior one third). In addition, the inclination angle played a big role in the overall shearing strength. It should be noted that the inclination angle could be either positive or negative, depending on whether the GP was sustaining a compression or tension load during this anterior-posterior shearing.

5.2.3. Compressive tests

A number of unconfined compression tests were conducted and reported (Cohen et al., 1994; Cohen et al., 1998; Sergerie et al., 2009; Wosu et al., 2012). In Cohen et al. (1994), the GP specimens (bone-GP-bone unit) were compressed by a vertical actuator in saline solution to 20% strain at three different strain rates: 0.38×10^{-3} , 0.76×10^{-3} and $1.53 \times 10^{-3} \text{ sec}^{-1}$. The actuator was held

in place after the pre-set compression length until the specimen finished the relaxation completely. The force and displacement were measured and recorded. The GP material was assumed to be a nonlinear biphasic material (solid matrix and interstitial fluid) with strain-dependent permeability. Four parameters were used to define the material properties: the aggregate modulus (H_A), Poisson's ratio (ν), and two intrinsic permeability coefficients (k_0 and M). Curve fitting was done for the results from one strain rate to get the optimized parameters and then the material constitutive model was verified by matching the test results from the other two strain rates. Further, in their continued study, Cohen et al. (1998) added transversely isotropic characteristic to the previous isotropic material model, making the GP material to be a transversely isotropic biphasic model (TIBPE). More parameters such as the Young's moduli and Poisson's ratios in- and out-of- the transverse plane were derived by curve fitting. Sergerie et al. (2009) used the same TIBPE material model to investigate different material properties from three zones in a GP (Figure 5-11).

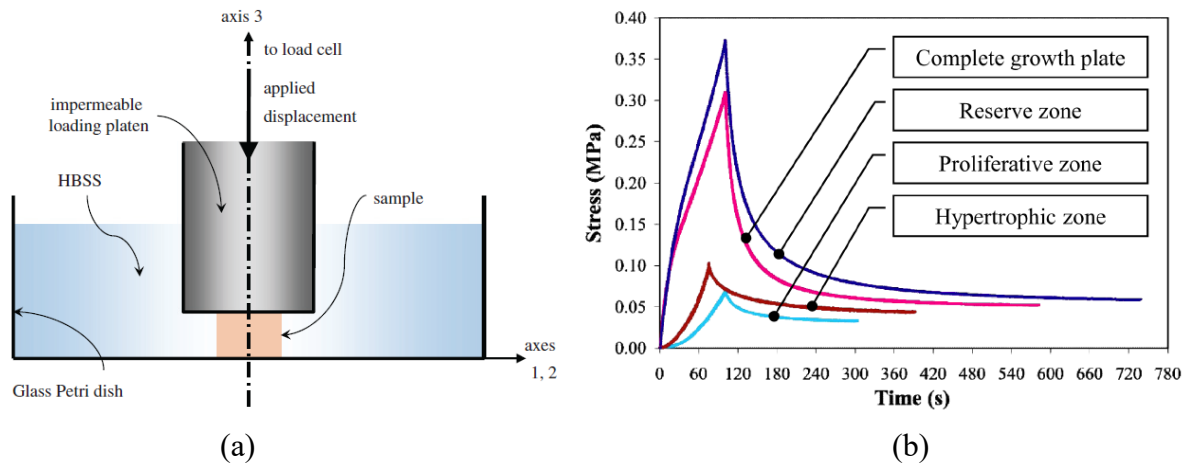


Figure 5-11: Unconfined compression test of GP. (a) Test schematic. The specimen is a thin disc of only GP tissue bathed in Hank's balanced salt solution (HBSS); (b) Experimental stress relaxation time histories on the complete GP and 3 zones respectively. (Sergerie et al., 2009)

A series of delicate processes were used to trim the GP specimens by three different zones. It was found that the reserve zone had significant higher transverse and axial Young's moduli compared to the proliferative and hypertrophic zones. Wosu et al. (2012) extracted the mechanical properties at four different growth stages of pig, using the same TIBPE material model and experiment settings. Nonlinear variation was found with the changing age.

The emphasis of this dissertation study is to identify pelvis and lower extremity responses in a 10 YO child. Because these compression tests had distinct loading conditions from pedestrian lateral impacts and the loading rates were also below those of typical car-to-pedestrian impacts, compression tests are not in the scope of the test design in this dissertation study. However, they can provide more understandings about the anisotropic and viscous features of GP, especially the values of the Poisson's ratio, which were rarely reported in other GP experimental studies.

The behavior of GP in compression tests showed transversely isotropic characteristics. The studies performed on animal samples show that the compression modulus was in the range of 0.3-1.1 MPa in the axial direction and 4.6-10.6 MPa in the transverse direction (Cohen et al., 1992; Cohen et al., 1994; Cohen et al., 1998; Fujii et al., 2000; Sergerie et al., 2009).

5.2.4. Summary of GP tests

In summary, a general range of the Young's modulus (or equivalent modulus) and ultimate strain were abstracted from the experimental studies. However, the mechanical results from tests using human subjects are very limited. Only two studies using human femoral head GP were found.

Although there are a larger number of tests for material properties of GPs from animal subjects,

no systematic investigation is available covering GPs from different sites of the same species of animal with the same age. Additionally, the tests of animal GP samples are mostly conducted at a quasi-static or low strain rate, which is not preferred for studying loading conditions such as traffic accidents. As a result, for better GP finite element modeling, more animal tests at higher loading rates are needed. If no more data of human subjects are discovered in the near future, the animal data could play an important role for estimating the human GP property, by applying some correlation method between human and animal subjects as previously discussed.

5.3. GROWTH PLATE FE MODELING STUDIES IN LITERATURE

Compared to the medical researches of the GP, which emphasize epidemiology, diagnosis and treatments, computational modeling of GP is not so widely investigated. To develop a clear strategy for GP modeling, it is necessary to review the existing FE modeling studies for GPs. The related studies are summarized as follows.

Sylvestre et al. (2007) included GP in a lumbar spine model, featuring three layers representing the three zones for each GP. The material is represented by a simple elastic model with the Young's modulus adopted from Cohen et al. (1998). The thickness proportions of three zones are 10% (reserve), 36% (proliferative) and 54% (hypertrophic), respectively.

During the development of the 10 YO neck model at WSU, GPs were modeled as single layer of elastic bricks in Dong et al. (2013). Fishkin et al. (2006) modeled the femoral head GP to study the disease of slipped capital femoral epiphysis (SCFE). The GP was modeled as three adjacent

plates, with a radius of curvature of 240 mm. Three zones had thickness of 0.3 mm, 1.2 mm and 0.3 mm, respectively. A lateral wall was built to mimic the ring of Lacroix, which is the mechanical support at periphysis. The GP was assigned a Young's modulus of 4 MPa. For the perichondral layers and the Lacroix, the Young's modulus was assumed 250 MPa and 775 MPa (referring to trabecular bone), respectively. The Poisson's ratio was assumed to be 0.49.

Sairyo et al. (2006) developed a lumbar spine FE model with GPs (single layers). The Young's modulus was assumed to be 10 MPa, and Poisson's ratio was 0.40, which was originally taken from the experimental study of Konz et al. (2001) on chacma baboon GPs. Ribble et al. (2001) employed the FE method to study the proximal tibia stress pattern for children from new-birth to eight years of age. The GPs at femoral head and greater trochanter were modeled as a continuous single GP. The Young's modulus was assumed to be 134 MPa and Poisson's ratio was 0.30. In the development of a 6 YO pedestrian FE model by Okamoto et al. (2003), the GP was included in the model, surrounding the second ossification center and the epiphyseal cartilage, but neither the geometric details nor the material properties of GP were reported. Gómez-Benito et al. (2007) studied the damage pattern of GP for SCFE patients. They made a thin layer of 1 mm thickness to connect the two sides of bone at the femoral head. Two models for a 14 YO boy with SCFE were developed and the GPs were modeled as breakable interfaces similar to a bone-cement bonding. It took into account that both shear stress and tensile stress and its parameters were fit based on the mechanical experimental studies.

To sum up, these literatures provide examples of how to reconstruct the GP in FE models. Most of the studies used simplified structures ignoring detailed undulations of the GP. Most of the studies modeled the GP structure using brick (solid) elements. The material properties were roughly estimated or referring to animal experiments. A few modeling studies involved the surrounding soft tissue of GP. Some studies discussed the failure criterion and damage pattern.

CHAPTER 6. GROWTH PLATE EXPERIMENTAL STUDY

Reviews summarized in the previous chapter indicated that the experimental data obtained from human GPs were very limited. Additionally, among the GP experimental studies conducted on animal subjects, few has investigated the strain rate effects or the differences among the GPs taken from different anatomic regions. To better understand the GP mechanical properties for more accurate modeling the human GPs, a series of tensile and shearing experiments on bone-GP-bone units of piglets were conducted. Firstly, a number of tensile tests were conducted on the femoral head GPs, mimicking the tensile tests on human subjects performed by Williams et al. (2001). The purpose of this series of experiments was to determine a conversion factor to correlate the mechanical properties of porcine and human GPs. Additional tensile tests were then conducted on three anatomic regions at the lower limbs (femoral head, distal femur, and proximal tibia) at different loading rates. Statistical analysis revealed that the effects of these two factors (location and strain rate) to the GP mechanical properties in tensile loads and shearing loads, which are of interest for pedestrian impact studies. Using the conversion factor from the tensile tests at the femoral head GP, the porcine GP material properties could be transferred to represent those of human 10 YO children.

6.1. METHODS

6.1.1. Test subject selection

Piglets were chosen as the test surrogates for human subjects. With respect to the age of pig which is correlated to 10 YO human, Franklyn et al. (2007) suggested that 6-month-old pigs/piglets

were comparable to 10 YO children. Discussions with personnel at the local pig farm, slaughterhouse, and distributor revealed that 20-week piglets were more suitable in terms of sexual maturity since the properties of GP are highly relevant to their growth phases (Celarek et al., 2014; Williams et al., 2001). The consultations suggested that 20-week-old (20 WO) piglets would be equivalent to young adolescence, whereas a 6-month one would correspond to late age of puberty. For this reason, the surrogate selected for the current experimental study was targeted on 20 WO piglets. Because the proposed human PLEX FE model is used to simulate pedestrian impacts initiated at the lower limbs, all the tests were conducted on the hind legs of piglets.

A power analysis was conducted to decide the minimum sample size. It was based on a precision criterion, considering the statistical distribution of the obtained measurements and the desired confidence interval. Equation 6-1 was used to estimate the minimum sample size by iteration (Zar, 2010):

$$n = \frac{s^2}{d^2} [t_{\alpha(2),\nu}]^2 \quad 6-1$$

, where n is sample size, s^2 is the sample variance (e.g. for tensile modulus), estimated with $\nu = n-1$ as the degrees of freedom, d is half of the desired interval with a confidence of $1-\alpha$ (normally 95%), $t_{\alpha(2),\nu}$ is the two-tailed critical value of Student's t distribution. Based on the pilot test on three piglets, the average Young's modulus of the proximal femur was derived for each piglet. The mean value is 11.03 MPa, with a variance of 5.78 (MPa)² and the d was set as 4.0 MPa. If n_0 is assumed as 4, the t distribution $t_{0.05(2),4-1}=3.182$. Bringing these values into the Equation 6-

1, the calculated n equals to 3.66, which is below the original estimated sample size of four. Thus, a sample size n of four (four piglets) is considered acceptable.

6.1.2. Specimen preparation and measuring

The hind legs from the 20 WO piglets, including the femur, tibia, fibula and the knee joint, were harvested with the flesh and skin removed at a local slaughterhouse. The legs were shipped in iceboxes to the laboratory within 24 hours after death. Upon arrival of the legs, the capsule and ligaments around the knee joint were dissected to isolate the femur and tibia. A variable-speed band saw (14" Tradesman Model 8201, Wilton Corporation, TN, US) was used to cut the femur and tibia into two parts across the mid-shaft. The same saw was further used for cutting the isolated femur and tibia into slices, as shown in Figure 6-1 (a). During the cutting, the room temperature was kept between 20° C and 30° C. Normal saline (0.9%) was sprayed to the cutting site to avoid overheating.

Figure 6-1 (b) shows a distal femur clamped in a specimen preparation fixture. Depending on the width of the femoral condyle, a total of 4 to 6 parasagittal slices, each with a thickness of 5 mm were cut. Guiding blocks and holding mechanisms were used to control the cutting to assure that all slices are parallel to the mid-sagittal plane. Figure 6-1 (c) shows a cut-off view of slice that consists of the epiphysis, GP, and metaphysis with the GP located near the center of the slice. Each parasagittal slice was further dissected into 3 to 5 bone-GP-bone units (also called as “specimens” hereafter), each with nominal dimensions of 5 mm×5 mm×40 mm (width × depth × length). These specimens were cut from the slice in a manner that the long axis of the specimen was parallel to

the longitudinal axis of the whole bone. For the GPs at femoral head, the axis of the femoral neck was treated as the longitudinal axis.

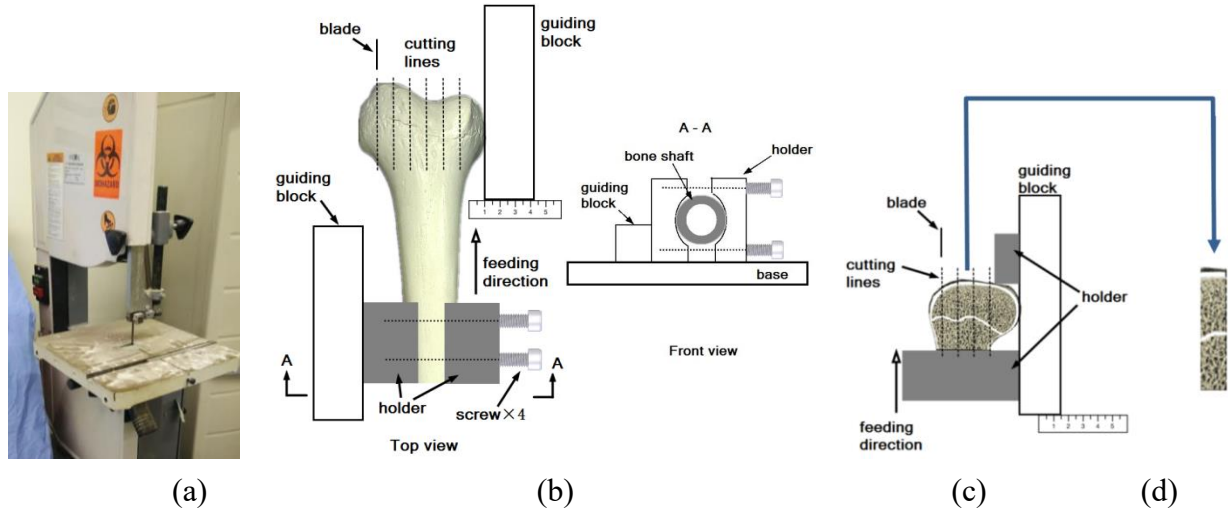


Figure 6-1: Bone-GP-bone unit cutting descriptions. (a) Cutting equipment: a vertical band saw; (b) A schematic diagram of the fixture and guiding blocks used for cutting a distal femur into sagittal slices; (c) A schematic diagram showing how a parasagittal slice was held and cut; (d) A cut bone-GP-bone unit, i.e. a specimen

The raw specimens were qualitatively screened using following criteria:

- The GP is continuous and intact with relatively uniform thickness
- The surfaces of the specimen are smooth and straight
- The bone segments are long enough for the fixtures to hold.

The distal tibia was excluded from this experimental study due to the complicated geometry of the articular surface and the consequential insufficient specimen harvested. They were labeled with sequential numbers and additional marks to denote the specimen locations and orientations. High-resolution photos of the specimens were taken using a digital camera (D80 DSLR, Nikon, Japan) with a precision ruler positioned next to each specimen. After these photos were taken, the

specimens were wrapped in cotton pads soaked with saline and then stored by anatomical regions in a plastic container with divided compartments. The container was sealed and stored in a -20°C freezer until the day before testing. The specimens were thawed in room temperature for 12 hours prior to the testing, and then kept in the container in a portable cooler until the testing. During the tests installing and loading, saline solution was sprayed to the specimens to avoid being dried out.

Specimen measuring

Digitizer software KLONK Image Measurement (Image Measurement Corp., WY, U.S.) was used to draw the reference lines within the software, and the distances and angles were measured, as shown in Figure 6-2.

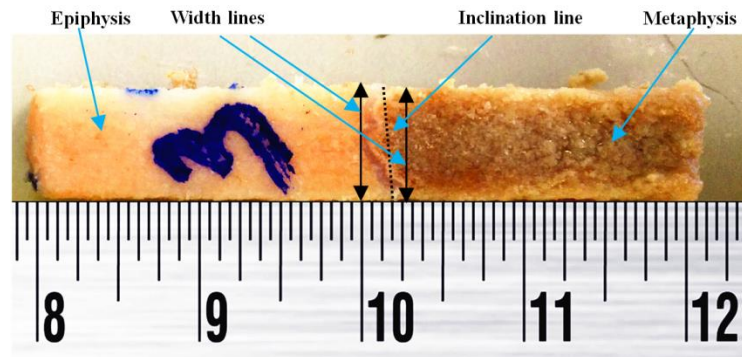


Figure 6-2: Specimen measurement: An anterior view of one specimen with a ruler positioned next to it

The procedures showing how measurements were taken and how they were used to calculate the geometric parameters for one specimen are described in Table 6-1. The anterior width was defined as the average distance measured from the two width lines crossing the most proximal and distal boundaries of GP on the anterior surface (Figure 6-2). The same procedures were used to measure the posterior width. The specimen width was then calculated by averaging the anterior

and posterior widths. The specimen depth was measured and calculated in the same manner, but on the lateral and medial surfaces.

Table 6-1: Calculations of various dimensions measured on each specimen

Original measurement	Intermediate measurement	Final parameter	Function of the final parameter
Anterior width: w_a	Specimen width: $w=(w_a+w_p)/2$	Area: $A=w \times d$	For calculation of stress: $\sigma=F/A$ (F : tensile force) $\tau=Q/A$ (Q : shear force)
Posterior width: w_p			
Lateral depth: d_l	Specimen depth: $d=(d_l+d_m)/2$		
Medial depth: d_m			
Anterior inclination angle: θ_a	N/A	Inclination angle (lateral-medial direction): $\theta=(\theta_a + \theta_p)/2$.	For specimen screening
Posterior inclination angle: θ_p			
GP thickness at five positions (t_i , $1 \leq i \leq 5$)	N/A	GP thickness: $t=\Sigma(t_i)/5$	For calculation of strain: $\varepsilon=\delta/t$ (δ : tensile displacement) $\gamma=Z/t$ (Z : shear displacement)
Coordinates of the highest and lowest points on anterior surface: x_{a1}, x_{a2}	Anterior Maximum Height: $R_{t,a} = x_{a1}-x_{a2} $	Normalized Roughness $R_n=\max(R_{t,a}/w_a, R_{t,p}/w_p)$	For specimen screening
Coordinates of the highest and lowest points on posterior surface: x_{p1}, x_{p2}	Posterior Maximum Height: $R_{t,p} = x_{p1}-x_{p2} $		

A GP inclination line on the anterior surface is drawn by connecting the endpoints (at the lateral and medial margins) of the GP (dotted line in Figure 6-2). The inclination angle on the anterior surface (θ_a) was measured as the angle between the inclination line and the width line. A zero degree indicates that the inclination line was perpendicular to the longitudinal axis of the bone.

The GP thickness was calculated by averaging the longitudinal measurements at five locations along the GP interface (respectively at the side margins, the center, and the first and third quarters). The anterior and posterior Maximum Heights ($R_{t,a}$ and $R_{t,p}$) were defined as the distance between the highest (most proximal) point and the lowest (most distal) point at a boundary line of the GP, which has been projected to the specimen long axis (Young and Budynas, 2002). They were calculated from the anterior and posterior surfaces, respectively. The Normalized Roughness, R_n , was calculated as the larger one of R_{t-a} and R_{t-p} divided by the respective width (Kishida and Uesugi, 1987) for the lateral-medial shearing test.

6.1.3. Experimental design

The influencing factors associated with strain rates and anatomic regions were taken into account in the experimental study. Three levels of strain rates, each with 20 times increments, were chosen. The approximate loading speeds in the tensile and shearing tests were around 0.08 mm/s (low), 0.16 mm/s (medium), and 3.2 mm/s (high). The actual testing speed was further adjusted according to the average GP thickness of each anatomic region from a specimen to assure that the loading rates in the same strain rate group were close to each other. Due to the compliance of the testing system, the actual strain rates applied to the GPs varied by the specimen's stiffness. As such, the loading speeds were selected referring to the settings used in previous studies, and more details are elaborated in Section 6.5.1. The femoral head, distal femur, and proximal tibia were

used to assess the effect of different anatomic regions. From each anatomic region of one piglet, force and deflection time histories were obtained at three different strain rates.

After the qualitative screening during the measuring stage, additional quantitative screening was conducted before the tensile tests and shearing tests were conducted. For the tensile test, the additional screening criteria were the inclination ($\theta \leq 40^\circ$) and Normalized Roughness ($R_n \leq 1.0$). These criteria were less strict regarding the GP shape factors compared to those for shearing tests because it was found by Cohen et al. (1992) that the angle of GP in a bone-GP-bone specimen would not significantly affect the tensile properties. For the shearing tests, the screening criteria were the inclination ($\theta \leq 20^\circ$) and Normalized Roughness ($R_n \leq 0.5$). In this manner, the effects of the roughness and inclination in the shearing tests could be reduced compared to the specimens in the tensile tests.

Tests with the rupture occurred away from the GP were excluded from the analysis, because the results from those tests may not be related to the properties of GP. Finally, results from 65 tensile tests and 48 shearing tests were available for further analyses. The number of tests available for data analyses are shown in Table 6-2 and Table 6-3 for tensile and shearing tests, respectively.

Table 6-2: The numbers of specimens tested in tension

Anatomic region	Strain rate			Subtotal
	low	medium	high	
Femoral head	5	7	5	17
Distal Femur	6	7	8	21
Proximal tibia	10	8	9	27
Subtotal	21	22	22	Total: 65

Table 6-3: The numbers of specimens tested in shear loading

Anatomic region \ Strain rate	Strain rate			Subtotal
	low	medium	high	
Femoral head	2	7	7	16
Distal Femur	4	5	5	14
Proximal tibia	6	5	7	18
Subtotal	12	17	19	Total: 48

6.1.4. Test setup and instrumentation

Tensile test

The test fixture was designed in a manner to mimic the tensile tests on human subjects by Williams et al. (2001). A mini Instron (model 8841, Instron, MA, US) was used to provide the loading. Two grip pairs were used to hold the bony portions of a bone-GP-bone specimen, at locations that were as close to the GP as possible. The upper grip pair was connected to the actuator of the mini Instron through a threaded rod. Nuts were applied to prevent loosening or slippage to the actuator and to the upper grip pair. The lower grip pair was connected to a load cell in the same manner. The load cell (model MDB-25, Transducer Techniques, CA, US), with a range of ± 111.2 N, was rigidly fixed to a movable extension plate that was constrained onto the Instron table by pressing bars and bolts as shown in Figure 6-3.

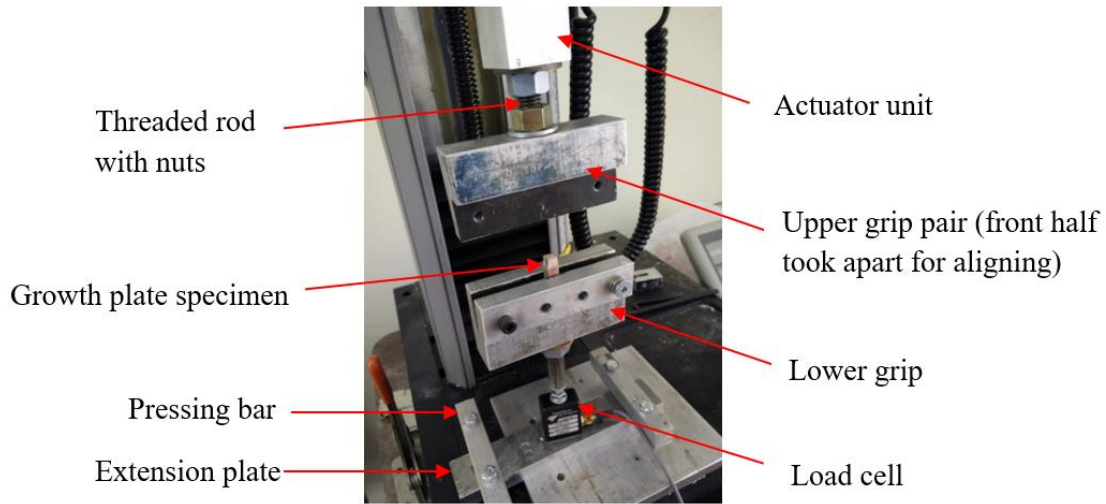


Figure 6-3: Porcine GP tensile test setup at the specimen aligning stage

When mounting the specimen, all screws and bolts were in position but loosened so that the upper and lower grip pairs could be properly aligned. The actuator was lifted with the front half of the upper grip pair opened to allow the specimen insertion into the lower grip pair first. The actuator and the upper grip pair was then moved slowly in the downward direction along with horizontal translation and axial rotation of the lower grip pair until the final alignment was achieved. Rigid plates were used to ensure that the upper and lower grip pairs were properly aligned. The edges of two grip pairs were assured to be close to the GP, but not overlapping the GP line. Afterward, the upper pair was clamped and all the screws and nuts were tightened carefully to prevent the specimen from damaging.

Like the tensile tests conducted by Williams et al. (2001), a digital camera with high definition (D80 DSLR, Nikon, Japan) was used to track the motion of the actuator, failure mode of the specimen, and any possible slippage of the specimen within the grips. A test showed any slippage

during the loading was considered as failure and the corresponding results were discarded. The data collection and processing was accomplished by using the hardware and software system TDAS-Pro (Diversified Technical Systems Inc., CA, US), which is a portable data collection unit. The sampling rates for the low-, medium-, and high-speed tests were 200 Hz, 500 Hz, and 10 kHz, respectively.

An additional series of static tensile tests with only the bony segment (trabecular bone) held in position was conducted to measure the intrinsic stiffness in the loading path of the testing system. Because under tensile loading, the deformation would not only happen onto the GP, but also to the Instron frame, the fixture blocks, the connecting bolts, the load cell internal structures, and the bony segment. A stepwise displacement was manually programmed through the Instron servo-hydraulic controller and the corresponding forces ranged from -30 to 100 N. The negative force (compression) was also covered to take into account the initial force caused by specimen installation. The force-displacement data points were recorded and plotted. The calculated system stiffness was 345.4 N/mm as derived by a linear curve fitting procedure, with a coefficient of determination (R^2) larger than 0.99. Using these data, the actual deformation of the GP specimen could be calculated for later stress-strain relationship calculation.

Shearing test

The Instron (model 8500, Instron, MA, US) was chosen to conduct the shearing tests. This machine provided easier interfaces than the mini-Instron (model 8841) when installing the

shearing test fixtures and larger load cell. The test setup had a similar concept as that reported by Williams et al. (1999) (see Figure 6-4). The specimens were positioned horizontally and the shearing force was provided by a vertically downward motion.

The right side of the bony segment of a specimen was held by a right gripping pair fixed to a self-lubricated roller bearing sliding carriage runs on two guiding tracks (McMaster-Carr Supply Co. OH, US). The snugness of the sliding mechanism was adjustable and the movement of the carriage was restricted to the longitudinal axis of the bone, with a low coefficient of friction. An adaptor plate connected the track guiding system to a load cell, which was rigidly mounted to the Instron table. This load cell was made by Robert Denton at Wayne State University, with a 500 lb. (± 2223 N) capacity, to record the force data.

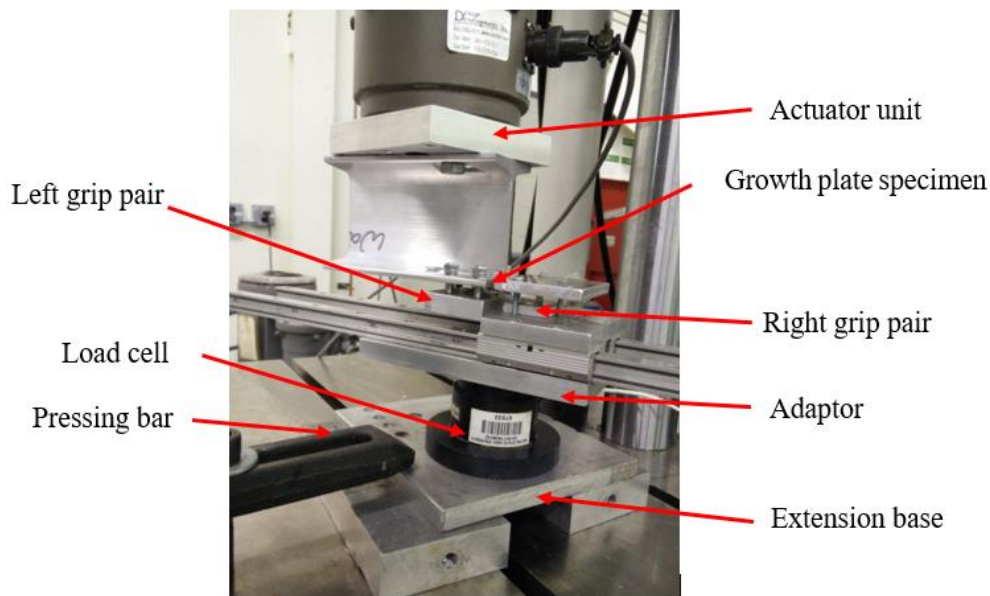


Figure 6-4: Porcine GP shearing test setup. The right grip pair is adjustable along the long axis of the bone-GP-bone specimen to allow proper positioning of the test specimen; The left grip pair is rigidly mounted to the vertical actuator of the Instron

The left (per the orientation in Figure 6-4) side of the bony segment was held by the left grip pair, which was rigidly mounted to the actuator of the Instron machine. During the downward motion of the actuator, the left segment of specimen was lowered vertically, while the right segment had no motions in all directions except the direction along the tracks. The edges of the grip pairs were set to be close to the GP interface, and the bolts and nuts were used for tightening the grips after the final alignment.

The sampling rates for the low-, medium-, and high-speed tests were selected to be 200 Hz, 500 Hz, and 10 kHz, respectively. The shearing deformation was assumed to be zero when a cut-off force of 1.0 N was reached so that the subtle clearance of the sled-track system can be compensated. The load cell was mounted on the bottom rather than on the actuator so that the inertia effect could be eliminated. The center line of load cell was aligned to the center of GP, thus the influence due to offset loading could be neglected.

As described in the tensile tests, the same image tracking system and data acquisition system were implemented. A series of static shearing tests with the two grip pairs tightly holding a bony segment were conducted to investigate the intrinsic stiffness of the test system. The stepwise displacement was manually applied through the Instron controller and the corresponding forces ranged from -30 to 200 N. The system stiffness was determined to be 693.6 N/mm through linear curve fitting, with a coefficient of determination (R^2) larger than 0.99. Therefore, the actual shearing deformation of GP could be deduced for later shear stress-strain relationship calculation.

6.1.5. Selection of stress – strain scales

Three different scales of stress-strain relationship: true stress-true strain (true scale), engineering stress-engineering strain (engineering scale), and engineering stress-finite strain (finite scale) were mentioned in various parts of this dissertation. The true scale can directly describe the material properties and is preferred for material constitutive modeling for more compliant materials. Many material models in commercially available FE codes are referring to true stress-true strain relationship. When the true scale is used, a direct material modeling methodology is applicable. In this method, the parameters of a material law were solved by comparing the true stress-strain curves from tests to the theoretical behaviors of the constitutive model. The engineering scale was most commonly used in the GP experimental studies. It can be obtained directly from the mechanical experiment, but it was limited to the small-deformation range to approximate the true stress-strain relationship of a material.

In the current study, the engineering strain could be as high as 0.40 in tensile tests, and as high as 1.0 in shearing tests, which exceeded the small-deformation range. Efforts were first made to transfer the stresses and strains from engineering scale to true scale, so that a direct material modeling could be achieved. For example, in a uniaxial tensile test, the transformation could be done by Equation 6-2.

$$\sigma_{true} = \sigma(1 + \epsilon) \quad \epsilon_{true} = \ln(1 + \epsilon) \quad 6-2$$

, where σ and ϵ are the engineering stress and strain, respectively. ϵ_{true} is the true strain, also known as logarithmic strain, which is defined as the accumulation of instantaneous increments

divided by the real-time length. σ_{true} is the true stress, defined as the load divided by the real-time cross-sectional area (Young and Budynas, 2002). Equation 6-2 is valid with two preconditions:

1. The stress is homogeneously distributed in the cross-sectional plane and the deformation is homogeneous along the specimen length.
2. The volume of the material is unchanged, i.e. the Poisson's ratio is close to 0.5 and the cross-sectional area can be determined from the real-time length.

For the current experimental study on GP specimens, the first precondition was not fulfilled because of the boundary condition limitation; the second precondition was unknown since the Poisson's ratio has not been measured. However, some literature has suggested that GP is not isotropic material and Poisson's ratio was expected to have different values in different directions (Sergerie et al., 2009; Villemure and Stokes, 2009). For example, Konz et al. (2001) found that the Poisson's ratio was 0.4 from chacma baboon GPs shearing tests; Sergerie et al. (2009) found that the out-of-plane Poisson's ratio was 0.08 in unconfined compression tests; Another study by Wosu et al. (2012) yielded that the Poisson's ratio at the same direction was 0.06. So, it was implied that Poisson's ratio for GP did not had a simple reference value and Equation 6-2 would not be applicable in the current study.

As a result, an indirect material modeling approach was used. In this method, FE models with the same bone-GP-bone structures as a specimen were built to mimic the tension and shearing loadings under the same boundary conditions as in the tests. Engineering stress and engineering strain were calculated from real-time externally applied force and displacement calculated from the simulations (dividing the force by the original area to calculate the stress and dividing the

deformation by the original length to calculate the strain, respectively). They were compared to the stress-strain captured from the tests in the same engineering scale. A set of optimization processes was then carried out to minimize the differences between the stress-strain curves from a test and the corresponding simulation. More details of the optimization can be found in Section 7.1. All the measurements were kept consistent in the same engineering scale.

Finite scale was not commonly used in GP experiments, but it was used in Williams et al., 2001 who tested GPs from human subjects. For later correlation of human-porcine GP material properties, the engineering strains in the porcine tests were transferred to finite strain, using the Equation 6-3:

$$\varepsilon_f = \frac{1}{2}(\lambda_s^2 - 1) , \quad \lambda_s = 1 + \varepsilon \quad 6-3$$

, where ε_f is the finite strain, λ_s is the stretch ratio, i.e. the deformed length divided by the original length.

To sum up, true stress-true strain was favorable for direct material modeling, but it was not applicable for current GP experiments. Engineering stress-finite strain was only used in a few experimental studies, including the key literature by Williams et al. (2001), whose data were taken as the reference for porcine-human GP correlation. A temporary transformation from engineering scale was performed to do this correlation. Engineering stress-engineering strain scale was finally chosen for current study. An indirect material modeling method was adopted accordingly.

6.1.6. Data acquisition and processing

The tensile and shearing forces were measured by two respective load cells, while the tensile and shearing displacements were measured by the two Instron systems. TDAS-Pro system was used for data acquisition. An electrical relay was used to trigger the force and displacement data acquisition simultaneously. The original binary data was exported to MS Excel for data processing by using TDAS Control software (Diversified Technical Systems Inc., CA, US).

In tensile tests, the load cell force (F) and actuator displacement (δ) time histories were measured. Given the static system stiffness (K_{0-t} , 354.4 N/mm) obtained previously, and the dimensional measurements: the average GP thickness (t) and the specimen cross-sectional area (A) of the specimen, the engineering tensile stress (σ) and strain (ε) were calculated as shown in Equations 6-4 and 6-5, respectively:

$$\sigma = \frac{F}{A} \quad 6-4$$

$$\varepsilon = \left(\delta - \frac{F}{k_{0-t}} \right) / t \quad 6-5$$

A typical engineering stress-strain curve is shown in Figure 6-5. A linear fit covering a range from 20% to 80% of the maximum stress was conducted to derive the tensile modulus (E) for each tensile test. The coefficient of determination (R^2) of each fit was also recorded to evaluate the goodness of the fit. The ultimate tensile stress (σ_{max}) and ultimate tensile strain (ε_{max}) were defined as the stress and strain when the stress arrived at the peak.

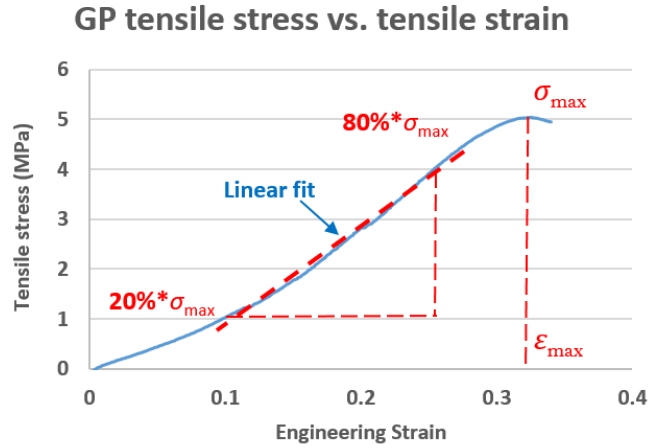


Figure 6-5: A typical engineering stress-strain curve from a GP tensile test. The calculation of the elastic modulus, ultimate stress, and ultimate strain were illustrated. Typically, there was a toe-in region followed by a larger linear segment. A decrease in slope, when the stress was approaching the ultimate point, was not always observed

For the shearing tests, the data processing procedures were similar to the tensile tests. The actuator force (Q), displacement (Z), and the system stiffness ($K_{0-s}=693.6$ N/mm) were used to determine the shear stress and strain. As in the tensile tests, the GP thickness (t) and cross-sectional area (A) of the specimen were taken from the measuring processes. The engineering shear stress and shear strain were calculated as shown in Equations 6-6 and 6-7, respectively.

$$\tau = \frac{Q}{A} \quad 6-6$$

$$\gamma = \left(Z - \frac{Q}{k_{0-s}} \right) / t \quad 6-7$$

Similar to the tensile stress-strain curves, a typical shear stress-strain curve had a toe-in region and large linear portion. The curve for each test was processed using the same method in the tensile tests to derive the shear modulus (G), ultimate shear stress (τ_{max}), and ultimate shear strain (γ_{max}) for each specimen.

6.1.7. Human-porcine GP correlation

To the best of the author's knowledge, the tension study on human femoral head GPs conducted by Williams et al. (2001) was the only available experimental study on human subjects. Therefore, the results of the tensile tests on the porcine femoral head GPs from the current study were compared to correlate animal tests to human test results. For the tests on human specimens, there were 8 specimens tested, 7 of which were from a 14 YO child and the other one was from an 8 YO child. These data provided, so far, the best estimation of GP tensile properties for 10 YO children. It was noticed that the strain formulation in that study was based on finite (large) strain, and the definition was adopted from an early growth plate experimental study reported by Cohen et al. (1992). The transformation function from engineering strain to finite strain was shown in Equation 6-3.

From the data obtained from the porcine femoral head GP tensile tests at the low strain rate, the average tensile modulus (E_p), ultimate stress ($\sigma_{max,p}$), and ultimate finite strain ($\varepsilon_{max,p}$) were elicited. The mean tensile modulus for human (E_h) was 4.26 MPa (± 1.22 MPa), the mean ultimate tensile stress $\sigma_{max,h}$ was 0.98 MPa (± 0.29 MPa), and the mean ultimate finite strain $\varepsilon_{max,h}$ was 31% ($\pm 7\%$). By assuming that the ultimate strain remained constant, a modulus conversion factor X could be used to scale the tensile modulus and ultimate tensile stress from porcine tests to human. This assumption was based on the finding by Williams et al. (2001) that the ultimate tensile strain was not sensitive to varying GP inclination angles and strain rates, but the tensile modulus and

ultimate stress were. Similar trends were found in the current porcine tests and would be described in detail in Section 6-2.

A normalized root mean square error (NRMSE), shown in Equation 6-8, was used to measure the difference between the two sets of material property parameters. This index was adopted for the optimization purpose in literature, such as those reported by Jin (2009) and Sergerie et al. (2009).

$$NRMSE = \sqrt{\frac{\left(\frac{X \cdot E_p - E_h}{E_h}\right)^2 + \left(\frac{X \cdot \sigma_{max,p} - \sigma_{max,h}}{\sigma_{max,h}}\right)^2 + \left(\frac{\varepsilon_{max,p} - \varepsilon_{max,h}}{\varepsilon_{max,h}}\right)^2}{3}} \quad 6-8$$

Using the equation, the best conversion factor X would be the one with the minimal NRMSE. A continuous change of NRMSE was plotted using Origin 8.1 (OriginLab, MA, US) while X was changed continuously. As a result, the optimal X (X_{opt}) associated with the minimum NRMSE was identified. This conversion factor, in the engineering stress-finite strain scale was assumed to be valid when transferring the porcine mechanical properties in engineering scale (E , σ_{max} , ε_{max} and G , τ_{max} , γ_{max}) to human GPs. Besides, the stress-strain curves in engineering scale obtained from the porcine specimens were accordingly transformed to human GP stress-strain relationships. Further material optimization processes would keep using the transformed curves as the optimization targets for the human GP material modeling.

6.1.8. Statistical analysis

Statistical analysis was conducted using SPSS v.24 (IBM, NY, US). Descriptive basic statistical analysis (mean, standard deviation) was performed for the major parameters, the GP thickness, strain rate, tensile properties (E , σ_{max} , ϵ_{max}) and shear properties (G , τ_{max} , γ_{max}).

Analysis of Variation (ANOVA) was conducted to investigate the effects of the anatomic region (three categories: femoral head, distal femur, and proximal tibia) and strain rate (low, medium, and high) on the material properties related to tensile and shear parameters (E , σ_{max} , ϵ_{max} and G , τ_{max} , γ_{max}). It should be noted that the piglet from which a specimen was taken from also played a factor in the tests, because in each factorial combination of strain rate and anatomic region, the specimens were not fully random and independent but relevant because some of them were from the same piglet (block). If the repeating appearances of the piglets were ignored, the result would be biased. As a result, Randomized block ANOVA was selected as the statistical model used in this study.

In this Randomized block ANOVA, the main effects and interacting effect of the two independent variables, "anatomic region" and "strain rate", were tested, while the dependent variables are the six parameters obtained from tensile and shearing tests. The independent variables were categorized, while all the dependent variables were continuous and in numeric format. The piglet subject was treated as the block factor and only its main effect was considered in the statistical model. Post Hoc analysis using Scheffe method was conducted to do pairwise comparisons to check the differences among the levels of a factor. If $p \leq 0.05$, the compared pair

(two levels) was considered as significantly different to each other. Otherwise, they could be pooled for a larger number of specimens.

6.2. RESULTS

6.2.1. Test results overview

Strain rates

As mentioned in Tables 6-2 and 6-3, 65 specimens were included in the tensile property study and 48 specimens in the shearing property study. Due to the system compliance issue mentioned in Section 6.1.5, the actual strain rates varied with the stiffness of the GP for each specimen, hence, the individual strain rate within a group varied slightly around the preset value. Table 6-4 shows the calculated strain rates falling into three categories: low, medium, and high strain rates, for both tensile and shearing tests. Statistically, each strain rate level was significantly different from the other two levels ($p < 0.001$).

Table 6-4: actual strain rates in tensile and shearing tests

Loading mode	Strain rate level	No of specimens	Mean train rate on GP (s^{-1})	Standard Deviation (s^{-1})
Tensile	low	21	0.0053	0.0017
	medium	22	0.094	0.038
	high	22	1.907	0.776
Shearing	low	12	0.0085	0.0015
	medium	17	0.163	0.030
	high	19	3.037	0.415

GP Thickness

The thicknesses of GP in each specimen were measured and the mean values were plotted by region as shown in Figure 6-6. The average thickness was 0.829 mm (± 0.159 mm) for the femoral head GPs, 0.918 mm (± 0.169 mm) for distal femur GPs, and 0.829 mm (± 0.157 mm) for proximal tibia GPs. A series of Student's *t*-tests were conducted and the results showed a significant difference between the GPs located in the femoral head and distal femur ($p=0.029$), distal femur and proximal tibia ($p=0.017$), whereas GPs located in the femoral head and proximal tibia had similar mean thickness values ($p=0.994$).

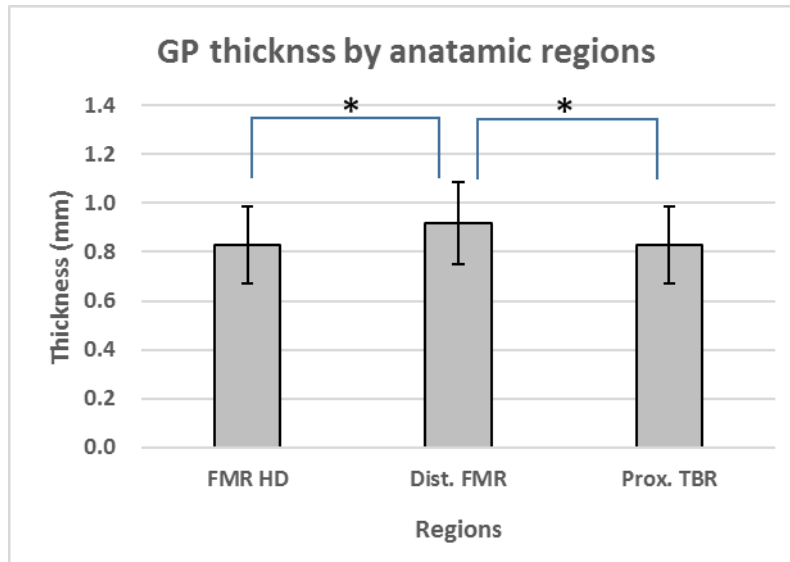


Figure 6-6: GP thickness measurement results. A “*” marking indicates a significant difference ($p < 0.05$). (FMR HD: femoral head; Dist. FMR: distal femur; Prox. TBR: proximal tibia)

Failure pattern

After examining the fractured post-tensile-test specimens (excluding the cases with fractures occurred on the bony portion), it was found that 90% of specimens had most of the GP tissues

remained on the epiphysis, based on visual examination and HD camera image analysis. As previously shown in Figure 5-2, the hypertrophic zone is adjacent to the calcified trabecular bone of metaphysis. Based on these observations and the layered structure of a GP, it was deduced that most of the failures happened in the hypertrophic zone, where the chondrocytes began to enlarge. This was consistent with the fact that the strength is weaker near the hypertrophic zone because of the enlarged chondrocytes and lower density of the inter-territorial matrix (Cohen et al., 1992; Fujii et al., 2000; Peterson, 2007). However, no scanning electron microscopy (SEM) or histologic section analysis was performed in the current study, since the focus was placed on the mechanical behaviors of the GP. Consequently, the author was not able to observe any similarities or variations compared to other published studies, such as the chondral bundles got pulled out of the matrix as described in the work of Williams et al. (2001), or a clear separation between hypertrophic zone and proliferating zone as reported by Fujii et al. (2000).

The failure modes observed after the shearing tests were similar to those after the tensile tests, but a higher probability of involving trabecular bones was noticed, especially when the roughness was large. After excluding these cases, the separation near hypertrophic zone was observed for most of the specimens. For some cases with more undulations, the cleavage plane passed through the reserve zone. These findings were consistent with the failure mode reported in the literature (Lee et al., 1985; Williams et al., 1999), although no detailed SEM or histologic image was provided in the current study.

Linearity

The tensile and shearing moduli were obtained from the tensile or shearing engineering stress-strain curves. The linear curve fitting of the curve segment from 20% to 80% of the ultimate stress resulted in an R^2 of 0.995 for tensile tests, and 0.992 for shearing tests, which demonstrated the high goodness of fit, i.e. the selected segments of the tensile and shearing stress-strain curves showed good linearity.

6.2.2. ANOVA results

Factorial effects comparison

The between-subject effects on tensile properties (E , σ_{max} , ϵ_{max}) and shearing properties (G , τ_{max} , γ_{max}) were tested using the Randomized block ANOVA. The p values for all independent variables are summarized in Table 6-5, where the critical significance level (α) is 0.05.

Table 6-5: P values calculated using the Randomized-block ANOVA on the three tensile and three shearing mechanical properties

Dep. Variables \ Indep. variables	Tensile modulus	Ultimate. tensile stress	Ultimate tensile strain	Shear modulus	Ultimate shear stress	Ultimate shear strain
Strain Rate	0.020*	<0.001*	0.555	0.001*	0.021*	0.918
Anatomic Region	0.030*	<0.001*	0.631	0.422	0.007*	0.729
Region * Strain Rate	0.602	0.723	0.885	0.998	0.939	0.990

* indicates that the p values < 0.05 .

For the tensile properties, the strain rate was a significant factor for the tensile modulus ($p=0.02$) and ultimate tensile stress ($p < 0.001$), while the anatomic region was a significant factor

for the tensile modulus ($p=0.03$) and ultimate tensile stress ($p < 0.001$). The interaction term of the region and strain rate was not significant for any of the three tensile properties. The ultimate tensile strain did not vary by any of the influencing factors studied. For the shearing properties, strain rate was significant for shear modulus ($p=0.001$) and ultimate shear stress ($p=0.021$). Anatomic region was not significant for shear modulus ($p=0.422$), but it is significant for ultimate shear modulus ($p=0.007$). The interaction term of region and strain rate was not significant for any of the three shearing properties. The ultimate shearing strain did not vary by any of the influencing factors in the current statistics model.

Means for each level of independent variable

The means of six mechanical properties (E , σ_{max} , ε_{max} and G , τ_{max} , γ_{max}) for the three anatomic regions and three strain rates are tabulated in Table 6-6 and Table 6-7, respectively, associated with the standard error of the mean (SEM).

Table 6-6: Mechanical properties of GPs in tensile and shearing tests at different strain rates

Strain rate Mat. property	Low		medium		high	
	Mean	SEM	Mean	SEM	Mean	SEM
E (MPa)	7.12	0.94	8.96	0.92	10.97	0.96
σ_{max} (MPa)	1.27	0.14	1.84	0.14	2.22	0.14
ε_{max}	0.255	0.018	0.282	0.018	0.275	0.019
G (MPa)	1.68	0.33	2.11	0.25	3.16	0.24
τ_{max} (MPa)	1.32	0.13	1.48	0.10	1.75	0.09
γ_{max}	0.844	0.096	0.817	0.072	0.797	0.068

Table 6-7: Mechanical properties of GPs in tensile and shearing tests at different anatomic regions

Region Mat. property	Femoral head		Distal femur		Proximal Tibia	
	Mean	SEM	Mean	SEM	Mean	SEM
E (MPa)	11.26	1.05	8.06	0.97	7.72	0.83
σ_{max} (MPa)	2.40	0.15	1.46	0.14	1.48	0.12
ε_{max}	0.286	0.020	0.259	0.019	0.268	0.016
G (MPa)	2.51	0.30	2.02	0.28	2.42	0.24
τ_{max} (MPa)	1.82	0.12	1.28	0.11	1.44	0.10
γ_{max}	0.850	0.085	0.836	0.080	0.772	0.070

Result of Post Hoc analysis

Post Hoc analysis was conducted to examine the difference in each pair of the levels of an independent variable. The distributions of E , σ_{max} , ε_{max} and G , τ_{max} , γ_{max} by anatomic region and strain rate are shown by bar charts with SEM bars in Figure 6-7 for strain rate effect, and in Figure 6-8 for anatomic region effect. After the Scheffe Post Hoc analysis, the pairs having significant differences ($p \leq 0.05$) are marked by “ * ” in the following figures.

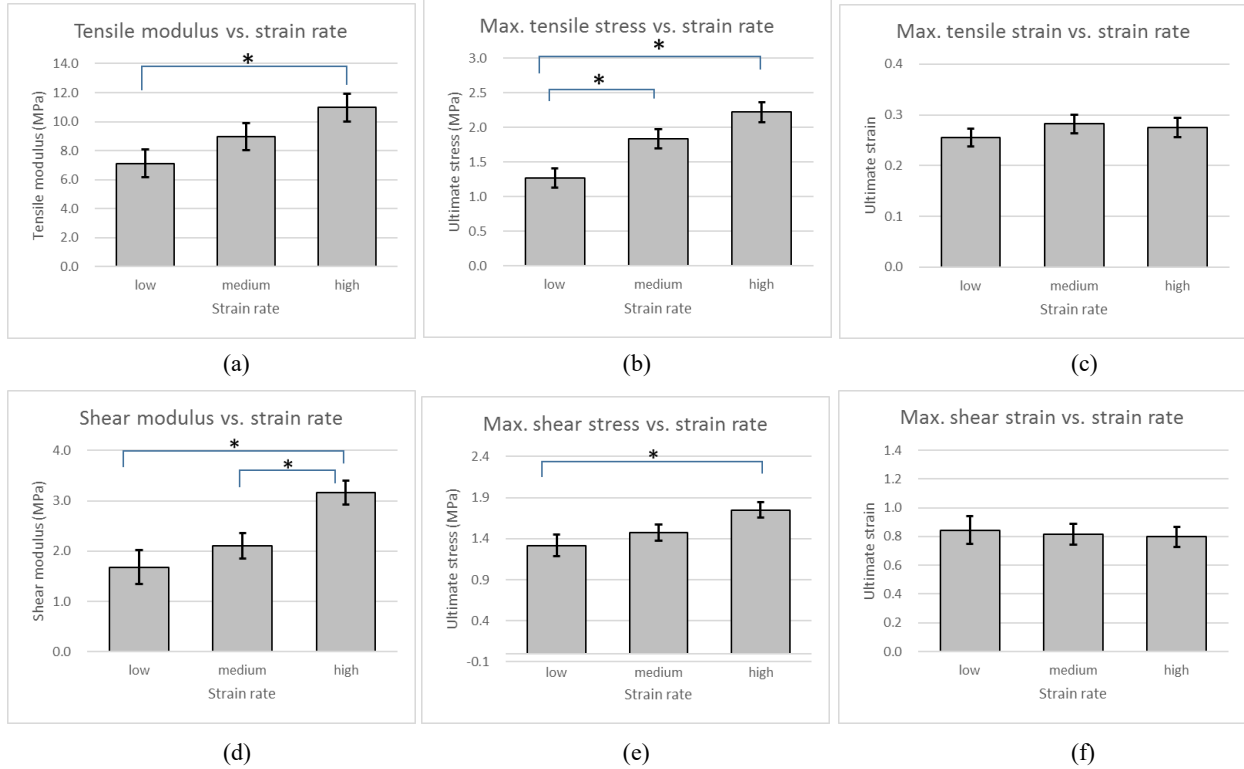


Figure 6-7: The effect of strain rate on tensile and shearing properties. The mean values are plotted as bars and the standard errors of the mean are also shown. A “*” marking indicates a significant difference

Generally speaking, the tensile modulus, ultimate tensile stress, shear modulus, and ultimate shear stress increased when the strain rate increased. As for the average E (tensile modulus), the high-rate group had a significantly higher modulus than the low-rate group did ($p=0.008$), but no significant difference was observed between the high-rate and medium-rate groups ($p=0.475$), or the medium-rate and low-rate groups ($p=0.134$). For the average σ_{max} (ultimate tensile stress), the high-rate and low-rate groups showed a significant difference ($p < 0.001$), while the high-rate and medium rate groups showed a marginally significant difference ($p=0.076$), and the medium-rate and low-rate groups showed a significant difference ($p=0.008$). For the average ϵ_{max} (ultimate tensile strain), all groups of strain rate did not have significant differences.

The average G (shear modulus) of the high-rate group is significantly higher than that of the low-rate group ($p=0.002$), and a significantly higher shear modulus than that of the medium-rate group ($p=0.006$). No significant difference on G was observed between the medium-rate and low-rate groups ($p=0.718$). For the average τ_{max} (ultimate shear strain), the high-rate and low-rate groups showed a significant difference ($p=0.005$), while no significant difference was observed between the high-rate and medium-rate groups ($p=0.178$), or the medium-rate and low-rate groups ($p=0.220$). For the average γ_{max} (ultimate shear strain), all groups of strain rate did not have significant differences.

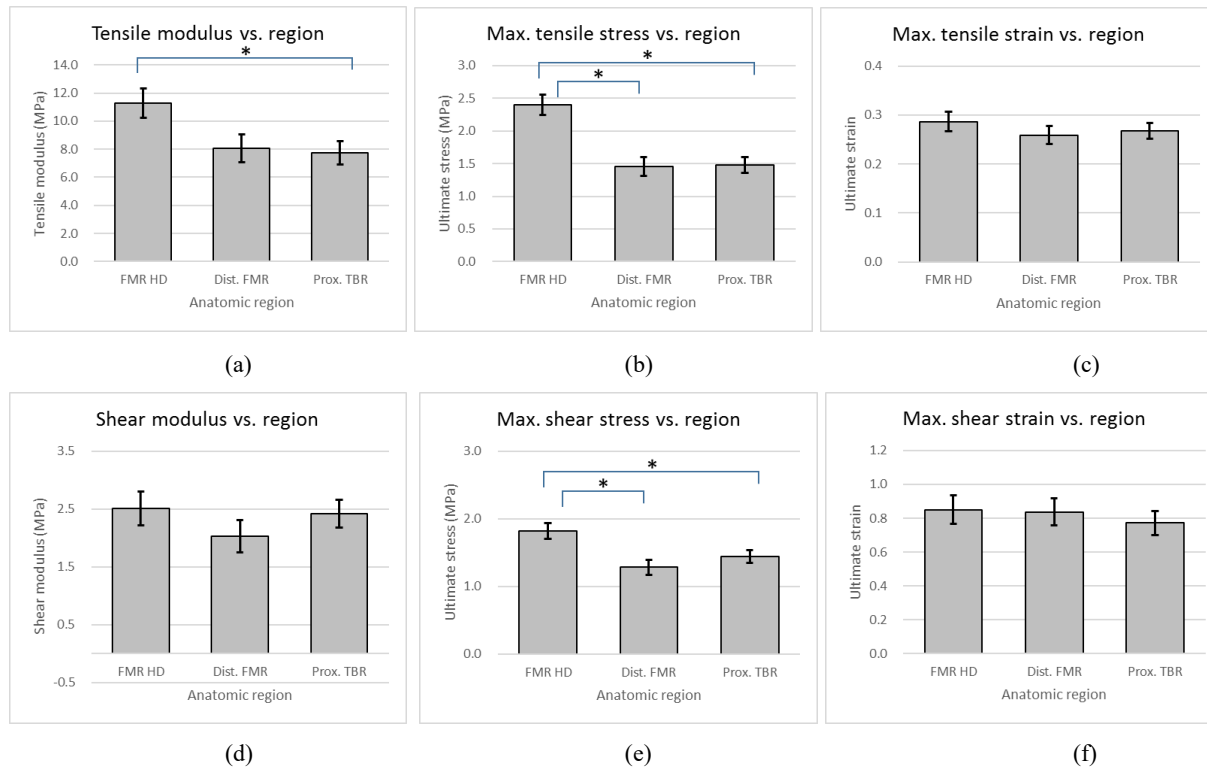


Figure 6-8: The effect of anatomic region on tensile and shearing properties. The mean values are plotted as bars and the standard errors of the mean are also showed. A “ * ” marking indicates a significant difference (FMR HD: femoral head; Dist. FMR: distal femur; Prox. TBR: proximal tibia)

The average E (tensile modulus) of the femoral head GPs (FH) was significantly higher than the proximal tibia GP (PT) ($p=0.021$), and marginally significantly higher than the distal femur GP (DF) ($p=0.06$). DF had similar E as PT ($p=0.947$). FH had significantly higher σ_{max} (ultimate tensile stress) than DF ($p < 0.001$) and PT ($p < 0.001$). DF had similar σ_{max} as PT ($p=0.978$). For ε_{max} (ultimate tensile strain), all groups of anatomic region did not have significant differences.

For the average shear modulus, none of the three pairs showed a significant difference. FH had significantly higher τ_{max} (ultimate shear stress) than DF ($p=0.001$) and PT ($p=0.017$). DF and PT had no significant difference on τ_{max} ($p=0.499$). For γ_{max} (ultimate shear strain), all groups of anatomic region did not have significant differences.

Based on the above findings, it is appropriate to group the results obtained from the distal femur and proximal tibia into one group to get a larger sample size representing the knee GPs. The femoral head GP should be treated separately in the material modeling. The factor that femoral head GP has higher moduli and ultimate stresses compared to the knee GPs could be explained by the dimensional and morphological differences between these GPs. For femoral head GP, the weight bearing function was realized by a smaller cross-sectional area and more inclined interface, when compared to the knee GPs. Therefore, it was reasonable to assume that the GP at the femoral head was mechanically stronger than the knee GPs. This turned out to be judicious based on the results of experimental study and human-porcine correlation in Chapter 6, and further observation from simulated human GPs responses using parametric constants determined from the GP material modeling described in Chapter 7.

6.3. HUMAN-PORCINE GP CORRELATION RESULT

Data obtained from the tensile tests on porcine femoral head GPs at the low strain rate were correlated with the human subject tests. This selection was made because both series of tests had similar strain rates (0.0053 s^{-1} for piglets vs. 0.003 s^{-1} for children) under tension, and the specimens were obtained from their respective femoral heads. The engineering stress-engineering strain curves obtained from the porcine femoral head GPs tests were firstly modified to the finite strain scale to have consistent reporting format as those reported for human subjects in Williams et al. (2001), using Equation 6-3. The modified curves using finite strain were plotted in Figure 6-9. The portion beyond the ultimate stress of each curve has been truncated, because after the failure point, the engineering strain on the GP calculated using Equation 6-5 became invalid.

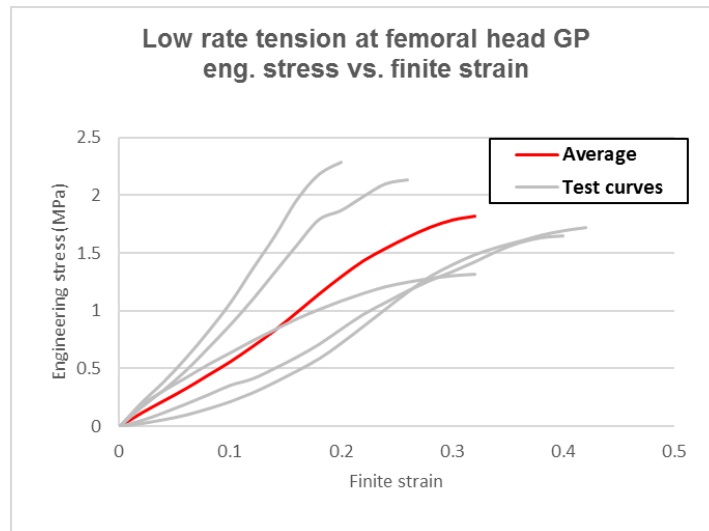


Figure 6-9: Relationship of the porcine femoral head GP engineering stress vs. finite strain. The average curve was derived using normalization, resampling, and averaging technique.

Averaging of five porcine experimental curves were conducted according to a normalizing process reported by Jin (2009). The average ultimate stress and ultimate strain were first calculated,

and then each curve was scaled to the same failure point. It was noticed that the scaled curves had different intervals at the horizontal axis (finite strain). A resampling technique was conducted based on interpolation to convert all curves with identical intervals at the horizontal axis. Then the average curve was obtained by numerical averaging of the stress at each strain point. This averaging curve obtained from the five normalized curves was treated as the average engineering stress vs. finite strain curve to represent the porcine femoral head GP. The resulting average curve is also plotted in Figure 6-9.

Based on the average curve calculated, the three tensile properties were extracted and compared to the human femoral head GP properties reported by Williams et al. (2001), as shown in Table 6-8.

Table 6-8: Comparison of the human and porcine tensile properties on the femoral head GP

Test subjects	Tensile modulus (MPa) (S.D.)	Max. tensile stress (MPa) (S.D.)	Max. tensile strain (S.D.)
Human femoral head GP (10 YO)	4.26 (± 1.22)	0.98 (± 0.29)	0.31 (± 0.07)
Porcine femoral head GP (20 WO)	8.356	1.820	0.32

The optimal solution was found when the minimal value of the normalized root mean square error (NRMSE), as illustrated in Equation 6-8, was achieved. The NRMSE history along with the continuously changing conversion factor (X) is plotted in Figure 6-10. The conversion factor (X) was changed by an increment of 0.0001 to search the minimum NRMSE. It was found the minimal NRMSE was 0.029, and the associated conversion factor was the globally optimal solution,

$X_{opt}=0.5234$. This is the correlation factor used to transform the porcine GP mechanical properties to those of human GP.

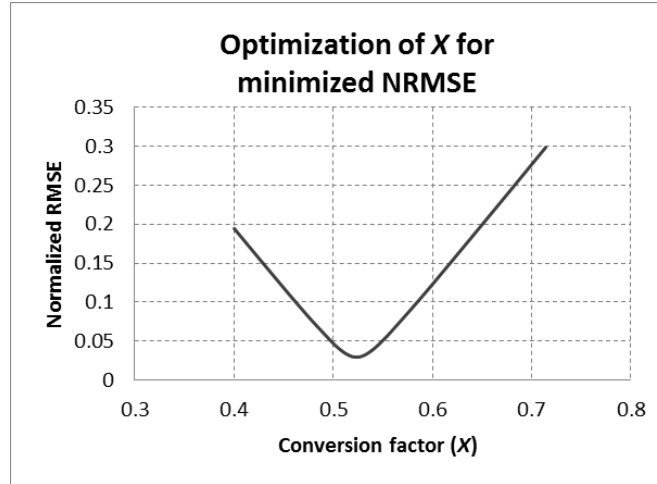


Figure 6-10: The normalized root mean square error (NRMSE) considering tensile modulus, ultimate tensile stress, and ultimate tensile strain. The minimal NRMSE was found as 0.029, and the optimal conversion factor X_{opt} was 0.5234



Figure 6-11: The transferred porcine engineering stress-finite strain curve using the correlation factor X_{opt} . The estimated failure point for 10 YO was plotted together with the that from human GP tests (William et al., 2001). The ranges of stress and strain with plus/minus one standard deviation were given

6.4. ESTIMATED 10 YO HUMAN GP PROPERTIES

Because there were no other human GP data available (Shearing test on human was reported by Chung et al. (1976), but it was on the whole femoral head, which was not similar in current porcine experiments), the same conversion factor ($X_{opt}=0.5234$) extracted from femoral head GP tensile tests was adopted to transfer the data obtained from 20 WO porcine GP to 10 YO human GP for the other two regions in tensile tests and all three regions in shearing tests. The tensile and shear stresses were both scaled by X_{opt} , while the tensile and shear strains stayed unchanged. This implementation was based on three assumptions. First, the relationship between porcine and human femoral head GPs would also be valid for the distal femur GP and proximal tibia GP. In other words, the mechanical properties variation pattern from the femoral head GP down to the proximal tibia GP were identical. The second assumption was the tensile properties scaling would also work for shearing properties, if both the tensile and shearing stiffness changes were caused by elastic difference between children and piglets. The third assumption was the ultimate strains (tensile and shearing) did not vary significantly despite the changing modulus. This assumption was based on the findings reported by Williams et al. (2001) that the ultimate strains were not as sensitive as the tensile modulus and ultimate tensile stress when the GP conditions were changed (anatomic site, loading rates). The same insensitivity was observed in the current tensile and shearing tests on porcine subjects.

The estimated 10 YO human tensile stress-strain curves and shearing stress-strain curves (in engineering scale) for human 10 YO femoral head GP were plotted in Figure 6-12. Portions of the

curves beyond the failure points have been discarded due to the unrealistic stress and strain representation specifically on the GP. The same normalizing, resampling and averaging methodologies, as described in Section 6.3, were used.

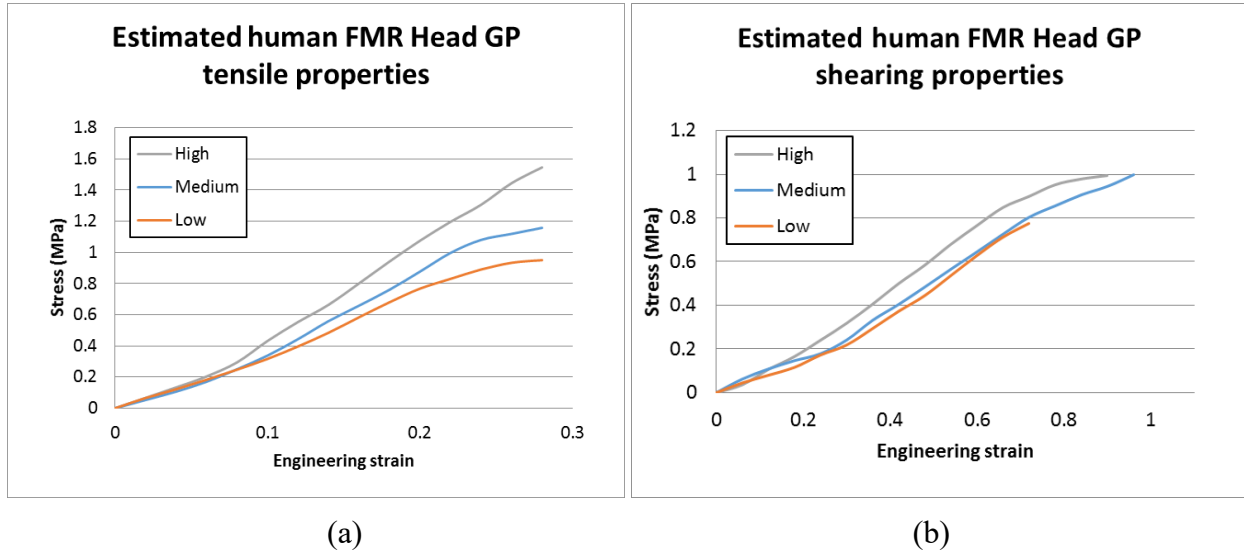


Figure 6-12: The estimated 10 YO human femoral head GP tensile engineering stress-engineering strain relationship (a), and shearing engineering stress-strain relationship (b). The curves were transferred from 20 WO piglets' mechanical properties of the same anatomic region. Three curves for the high, medium, and low strain rates were separately plotted for each loading condition. The curve portions beyond the failure points have been discarded

The estimated 10 YO human tensile stress-strain curves and shearing stress-strain curves (in engineering scale) for human 10 YO knee (distal femur and proximal tibia) GPs were plotted in Figure 6-13. As for femoral head GP, the curve portions beyond the failure points have been removed.

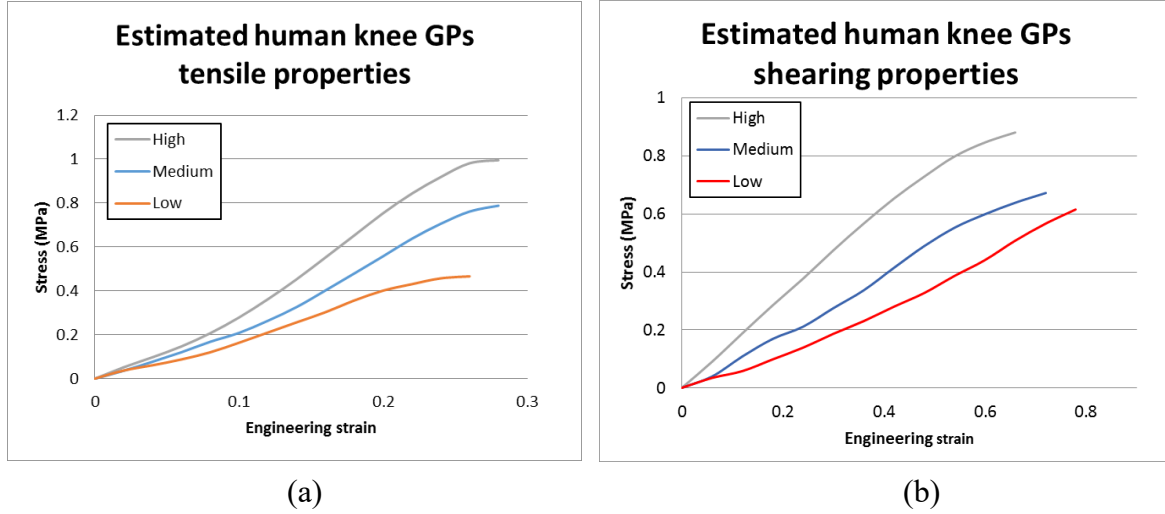


Figure 6-13: The estimated 10 YO human knee (distal femur and proximal tibia) GP tensile engineering stress - engineering strain relationship (a), and shearing engineering stress-strain relationship (b). The curves were transferred from 20 WO piglets' mechanical properties of the same anatomic region. Three curves for the high, medium, and low strain rates were separately plotted for each loading condition. The curve portions beyond the failure points have been discarded

6.5. CHAPTER DISCUSSIONS

6.5.1. Loading rate selection

The strain rates in the current tensile tests ranged from 0.0053 ± 0.0017 to 1.907 ± 0.78 , and the strain rates in shearing tests ranged from 0.0085 ± 0.0015 to 3.037 ± 0.415 . They were compared to the tensile tests and shearing tests conducted in either animal subjects or human subjects, and the loading speeds or rates were listed in Table 6-9.

Table 6-9: Comparison of the loading speeds/rates of current study and literatures

Literature	Loading speed or strain rate	Loading type	Test subject
Cohen et al. (1992)	0.004 mm/s	tension	Bovine GP
Moen and Pelker (1984)	0.5 mm/s	tension	Bovine GP
Noble et al. (1982)	0.25 mm/s	tension	Rabbit GP
Guse et al. (1989)	0.25 mm/s	tension	Rabbit GP
Fujii et al. (2000)	0.0083 mm/s	tension	Rabbit GP
Williams et al. (2001)	0.0004, 0.004 and 0.04 mm/s	tension	Bovine GP
	0.003 s ⁻¹	tension	Human GP
Current study	0.0053 to 1.907 s ⁻¹ or equivalent to 0.004 to 1.53 mm/s	tension	Porcine GP
Literature	Loading speed or strain rate	Loading type	subject
Chung et al. (1976)*	0.033 mm/s	shearing	Human GP
Moen and Pelker (1984)	0.5 mm/s	shearing	Bovine GP
Lee et al. (1985)	0.5 mm/s	shearing	Rabbit GP
Williams et al. (1999)	0.04 mm/s	shearing	Bovine GP
Bright et al. (1974)	20 mm/s	shearing	Rat GP
Current study	0.0085 to 3.037 s ⁻¹ or equivalent to 0.007 to 2.4 mm/s	shearing	Porcine GP

*: The Chung's study utilized the whole femoral head of human in their tests. As such, these tests were not comparable to the current study, hence the test results were not used to determine the conversion factor for shearing.

For the tensile tests, it can be found that the lowest strain rate level in the current study was comparable to the tensile test on human subject reported by Williams et al. (2001), and at the same level as the quasi-static experiments conducted by Cohen et al. (1992) and Fujii et al. (2000). The highest strain rate in the current study has been higher than those in early literature. For the shear tests, the lowest strain rate level in the current study was lower than those reported in the shearing experiments in literature. The highest strain rate in the current study was higher than most of those published in literature, except the shearing strain rates were lower than those reported by Bright et al. (1974).

In order to investigate the rate effect, an interval of 20 times was set for the low to medium strain rate, and medium to high strain rate levels. The current strain rate selections covered a reasonable strain rate range as a pioneering in-depth GP mechanical study, including rate effect and anatomic region differences. It was noted that in the pedestrian impact to a human child, the human body might be exposed to a dynamic loading with a strain rate which is much higher than the those conducted in the current experiments. A discussion was made in Section 7.4 based on a whole-body pedestrian simulation. Although the accurate loading rate on a GP in a real-world high-speed car-to-pedestrian impact accident is unknown. As a result, the tensile and shearing tests at higher strain rates would be demanded in the next stages of study on the GP material properties.

6.6. CHAPTER SUMMARY

Among all specimens harvested from four 20 WO piglets, 65 specimens were included in the tensile tests and 48 specimens in the shearing tests. Three levels of strain rate for tensile tests

(0.0053 to 1.907 s⁻¹) and for shearing tests (0.0085 to 3.037 s⁻¹) were conducted, and three anatomic regions were chosen: the femoral head GP (FMR HD), distal femur GP (dist. FMR), and proximal tibia GP (prox. TBR). The majority of tension failures were in the hypertrophic zone, while most of the shearing failures happening in the hypertrophic zone as well, although a larger variation of failure modes was observed in shearing. The findings were consistent with those reported in the literature.

Randomized block ANOVA was performed to investigate the effects of strain rates and anatomic regions on the six mechanical property parameters: E , σ_{max} , ϵ_{max} and G , τ_{max} , γ_{max} . For the tensile properties, anatomic region was a significant factor for E ($p=0.03$) and σ_{max} ($p < 0.001$), while strain rate was a significant factor for E ($p=0.02$) and σ_{max} ($p < 0.001$). For the shearing properties, anatomic region was not significant for G ($p=0.422$), but significant for τ_{max} ($p=0.007$). Strain rate was significant for G ($p=0.001$) and τ_{max} ($p=0.021$). The interaction term of anatomic region and strain rate was no significant for all six material properties. The ultimate tensile strain and shearing strain did not vary by any of the influencing factors.

Paired comparisons were conducted using Scheffe Post Hoc analysis. As for the strain rate effect, the high-rate group had higher E than the low-rate group (10.97 MPa vs. 7.12 MPa, $p=0.008$); the high-rate group had higher σ_{max} than the low-rate group (2.22 MPa vs. 1.27 MPa, $p < 0.001$) and the medium-rate group had higher σ_{max} than the low-rate group (1.84 MPa vs. 1.27 MPa, $p=0.008$); the high-rate group had higher G than the medium-rate group (3.16 MPa vs. 2.11

MPa, $p=0.006$) and the low-rate group (3.16 MPa vs. 1.68 MPa, $p=0.002$); the high-rate group had higher τ_{max} than the low-rate group (1.75 MPa vs. 1.32 MPa, $p=0.005$).

As for the anatomic region differences, FMR HD had a higher E than prox. TBR (11.26 MPa vs. 7.72 MPa, $p=0.021$); FMR HD had a higher σ_{max} than dist. FMR (2.40 MPa vs. 1.46 MPa, $p < 0.001$) and prox. TBR (2.40 MPa vs. 1.48 MPa, $p < 0.001$); FMR HD had a higher τ_{max} than dist. FMR (1.82 MPa vs. 1.28 MPa, $p=0.001$) and prox. TBR (1.82 MPa vs. 1.44 MPa, $p=0.017$). Based on results of these comparisons, the distal femur and proximal tibia GPs were grouped together.

The 10 YO human-20 WO porcine GP correlation was done and the optimal conversion factor was determined to be 0.5234 as to minimize the overall error for the tensile properties. Based on this scaling factor, the 10 YO human tensile and shear stress-strain curves at the femoral head GP and knee GP were estimated using the porcine experimental data. The curves were plotted and discretized at different strain rates, and these data could be taken for human GP material modeling to be described in the Chapter 7.

CHAPTER 7. HUMAN GROWTH PLATE MODELING AND PARAMETRIC STUDY

In this chapter of GP modeling study, the three main focuses are: (1) Determine a material model and its parameters to mimic the human GP mechanical behavior based on the results from Chapter 6, (2) Establish a detailed FE model of a 10 YO child proximal femur with the femoral head GP embedded, and (3) Conduct a series of parametric study on the 10 YO pedestrian model with GPs in the hip and the knee regions by using an SUV-to-pedestrian impact scenario. It was noted that all the stresses and strains in this chapter were in engineering scale.

7.1. 10 YO HUMAN GP MATERIAL MODELING

7.1.1. Material model selection

Selecting a constitutive model to mimic the human GPs was based on the resulting stress-strain curves at different strain rates estimated for GPs of 10 YO Children as described in Chapter 6. Significant strain rate effects have been observed on the tensile modulus, ultimate tensile stress, shear modulus, and ultimate shearing stress, based on the Randomized block ANOVA. These conclusions were consistent with the early studies reported by Williams et al. (1999), Sergerie et al. (2009) , and Wosu et al. (2012), etc. Therefore, proper modeling of the human GPs needs to use a material model capable of reflecting the strain rate effect.

A quick review was performed to check the relationship between the tensile and shear moduli for the femoral head GP of a 10 YO child. The average stress-strain curves for the tensile and shear tests at the low strain rates previously shown in Figure 6-12 (a) and (b) were replotted, and a linear

fitting was conducted to quickly estimate the tensile and shear moduli, as shown in Figure 7-1. It was noticed that the engineering stress-strain curves were considered as close to the true stress-strain when the deformation was small. Thus, the first halves of these curves were used to calculate the slope. The resulting Young's modulus E was 3.29 MPa, and the shear modulus G was 0.75 MPa from the linear curve fitting.

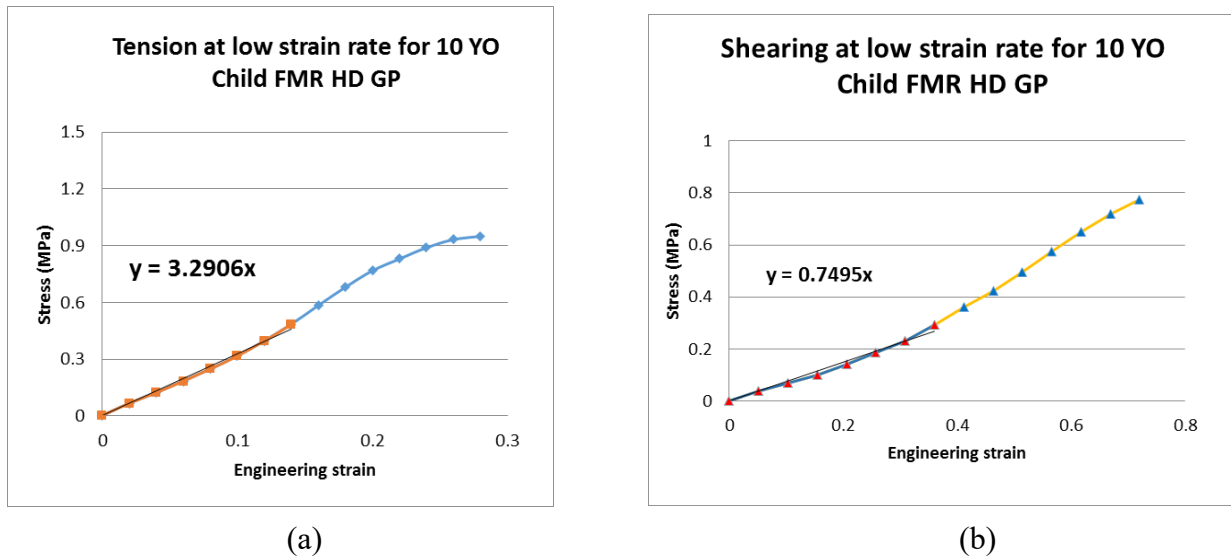


Figure 7-1: Linear fitting for the initial portion of the tensile stress-strain and shearing stress-strain curves estimated for 10 YO child as shown previously in Figure 6-12. The Young's modulus and shear modulus were estimated to be: $E=3.29$ MPa, $G= 0.75$ MPa

Assuming the material is isotropic and elastic, the Poisson's ratio (ν) can be calculated by Equation 7-1 (Young and Budynas, 2002):

$$\nu = \frac{E}{2G} - 1 \quad 7-1$$

Using this equation, the Poisson's ratio calculated from the estimated tensile and shear moduli was 1.19, which was unrealistic as the Poisson's ratio lies between 0 and 0.5 for any isotropic

natural material. The relationship between the tensile modulus and shear modulus as calculated from Equation 7-1 invalidated the isotropic assumption for the GP material.

From biological structure of the GP tissues, a number of studies have suggested that the GP tissue has column-like arrangement of chondrocytes along the growth direction that serve as strengthening fibers surrounded by the ground substances. This architectural arrangement makes the GP to be out-of-plane anisotropic and in-plane isotropic and was called as a transversely isotropic, hyperelastic material by Cohen et al. (1998).

Based on the above factors, the No. 92 material law, MAT_SOFT_TISSUE_VISCO (written as MAT_92 for short) available in LS-DYNA, was chosen, because it can represent the transversely isotropic hyperelastic features by using a directional strengthening theory. The viscosity option provided the capability of modeling the strain rate dependency. This material model would be used for the reverse engineering processes to determine the unknown material properties by optimizations.

7.1.2. Material law and parameters

As introduced in the theory manual of LS-DYNA (Hallquist, 2007), MAT_92 is a transversely isotropic hyperelastic model for representing biological soft tissues such as ligaments, tendons, and fascia. The representation includes an isotropic Mooney-Rivlin matrix reinforced by fibers to contribute as collagens. MAT_92 material law assumes a strain energy function as described in Equation 7-2:

$$W = C_1(\tilde{I}_1 - 3) + C_2(\tilde{I}_2 - 3) + F(\lambda) + \frac{1}{2}K[\ln(J)]^2 \quad 7-2$$

The overall strain energy W has four terms: two isotropic deviatoric matrix terms (associated with the Mooney-Rivlin coefficients C_1 and C_2), a fiber term F (a function of λ , which is the stretch ratio along the fiber direction, as shown in Equation 7-3), and a bulk term (associated with bulk modulus K). \tilde{I}_1 and \tilde{I}_2 are the deviatoric invariants for right Cauchy deformation tensor, as in the isotropic terms. J is the volume ratio, and K is the effective bulk modulus of the material (input parameter K).

$$\frac{\partial F}{\partial \lambda} = \begin{cases} 0 & \lambda < 1 \\ \frac{C_3}{\lambda} [\exp(C_4(\lambda - 1)) - 1] & 1 < \lambda < \lambda^* \\ \frac{1}{\lambda}(C_5\lambda + C_6) & \lambda \geq \lambda^* \end{cases} \quad 7-3$$

The fiber term is further divided into three segments: when $\lambda < 1$, the added strain energy is zero, i.e. no extra stiffness added when compressed; when $1 < \lambda < \lambda^*$ the added strain energy is governed by an exponential function involving coefficients of C_3 and C_4 ; when $\lambda > \lambda^*$, the slope is determined by C_5 and C_6 . λ^* is the boundary stretch between two segments.

The viscosity is superposed via a convolution integral function for the time-dependent 2nd Piola-Kirchhoff stress $\mathbf{S}(\mathbf{C}, t)$, where \mathbf{C} is the right Cauchy-Green deformation tensor, as shown in Equation 7-4.

$$\mathbf{S}(\mathbf{C}, t) = \mathbf{S}^e(\mathbf{C}) + \int_0^t 2G(t-s) \frac{\partial W}{\partial \mathbf{C}(s)} ds \quad 7-4$$

This material model can be approximated by a six-term Prony series kernel for the stress relaxation function. In this case, the hyperelastic strain energy represents the elastic (long-time) response. \mathbf{S}^e is the elastic part and not time dependent. $G(t-s)$ is a reduced relaxation representation, written as a summation of a Prony series, as shown in Equation 7-5, which has the maximum of 6 as the number of the Prony factors S_i and correlated time T_i . In this study, a two-term Prony series were used: S_1, T_1 , and S_2, T_2 .

$$G(t) = \sum_{i=1}^6 S_i \exp\left(-\frac{t}{T_i}\right) \quad 7-5$$

7.1.3. Specimen tension and shearing simulation

For the reverse engineering process to optimize the material properties, the specimen tension and shearing simulations were required as a step in an iteration. The simulation setting is introduced in this section.

A generic FE model of bone-GP-bone unit, with an element size of 0.17 mm along each direction, was built to represent the average porcine specimens, as shown in Figure 7-2. The average dimensions of porcine GPs tested and reported in Chapter 6 were 5.1 mm×5.1 mm (depth×width), while the average GP thickness was 0.85 mm. Tensile and shearing loadings were simulated using this generic model for the optimizations to be described in the next section. In tensile loading, the upper bone segment allowed translation at a constant speed in the +Z direction, while the lower bone segment was fully constrained, as shown in Figure 7-2 (a). In shear loading, the upper bone segment allowed translation at a constant speed in the +X direction, while the lower

bone segment was constrained in the manner that only the degree of freedom (DOF) in the Z axis was allowed, as shown in Figure 7-2 (b).

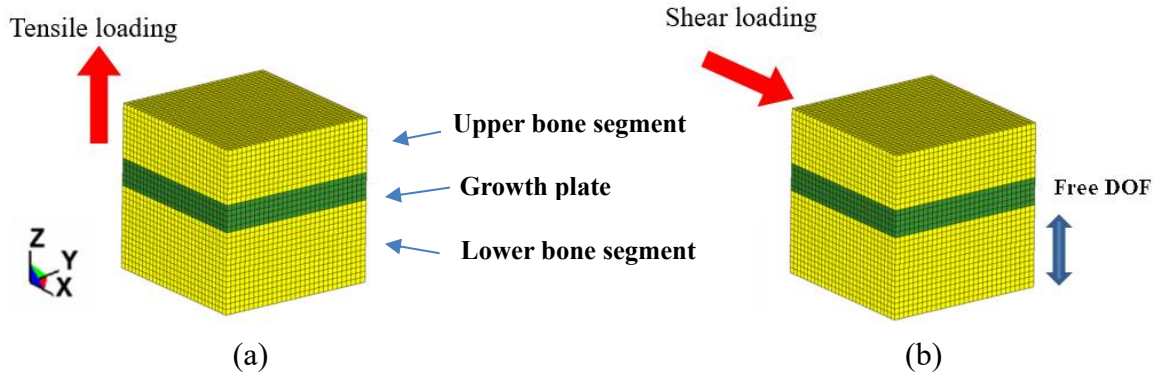


Figure 7-2: Tension and shearing simulations using the generic FE model of a specimen. (a) Tension in the +Z direction; (b) shearing in the +X direction

The loading speeds in the experimental study and the simulations to be performed in the iterations of optimization for human femoral head GP are listed in Table 7-1. The tension was applied until the +Z displacement of 0.255 mm (engineering tensile strain of 0.3) and the shearing was applied until the +X displacement of 0.765 mm (engineering shear strain of 0.90).

Table 7-1: Loading conditions of generic FE model representing the corresponding experiments on the femoral head GP specimens

Optimization stage	Tensile/shearing	Average loading speed on the porcine femoral head GP (mm/s)	Simulation loading speed (mm/s)	Max. displacement (mm)
Low-speed	Tensile	0.003655	0.34 *	0.255
	Shear	0.006205	0.51 *	0.765
High-speed	Tensile	1.50	1.50	0.255
	Shear	2.70	2.70	0.765

*: The quasi-static tensile and shear tests at low-speed were simulated at higher speeds, since no rate effect was considered at the stage

The simulations were performed using LS-DYNA (v. 971, R6.1, Livermore Software Technology Corporation, Livermore, CA). The trabecular bones were modeled as MAT_RIGID, since the engineering stress-engineering strain had been transferred to the GP material in the process of system compliance compensation, as described in Section 6.1. The density for the GPs was set as 1.2×10^{-6} kg/mm³, the same as the cartilage as reported in literature by Li et al. (2006). The critical stretch λ^* was set as 1.15, after preliminary trials to match the curve trends. The values of the remaining material parameters in MAT_92 were changed and inserted as needed during the iterative procedure of the optimizations, to be described in the following section.

From the FE simulations, the engineering stress was calculated by dividing the tensile force or shearing force by the cross-sectional area of the GP. The engineering strain was calculated by dividing the displacement by the original GP thickness. The calculation method is identical to that adopted in the experimental study.

7.1.4. Optimization processes

The optimization was conducted by using modeFRONTIER v. 4.5 (ESTECO, Italy). This software package can provide a multi-objective optimization platform coupling to the CAE software such as LS-DYNA. The unknown parameters needed for MAT_92 fell into two general categories: the hyperelasticity (bulk modulus, $C_1 \sim C_6$) and viscosity associated parameters (S_i, T_i). Two stages of optimization were carried out to optimize these parameters for representing the 10 YO femoral head GPs first.

In the first stage, the viscosity option of MAT_92 was switched off. In the second stage, the previously determined parameters, bulk modulus and $C_1 \sim C_6$, were adopted into optimization to determine the viscosity parameters, S_1, T_1, S_2, T_2 .

The Objective function

The two stages of optimization had two objective functions, OBJ_{low} and OBJ_{high} . OBJ_{low} was the normalized differences between the engineering stress-strain curves from the simulations and the corresponding curves estimated for 10 YO GP in low-speed tension and shearing loadings. OBJ_{high} was the same measurement for the high-speed curves. They were defined in the same manner, as shown in Equation 7-6.

$$OBJ = \sum_{i=1}^n \left(\frac{\sigma.tgt_i - \sigma.simu_i}{\sigma.simu_i} \right)^2 \quad 7-6$$

, where $\sigma.tgt_i$ and $\sigma.simu_i$ are the stress values (tensile or shear) for each data point from the target curves, and simulation result curves, respectively. n is the number of the discrete data points, and all the points were obtained at a constant time increment, i.e. constant strain increment. For example, for the femoral head GP in the 1st stage of optimization, the increment strain was 2% for tension and 6% for shearing, so that the number of discrete data points were both $n=15$.

Optimization of the 1st stage

The first step was finding the initial ranges of parameters K and $C_1 \sim C_6$ for hyperelasticity, for design of experiments (DOE) space generation. The initial ranges of the parameters were obtained by referring to the studies that also used MAT_92 for modeling low limb ligaments (Li et al., 2007;

Yue et al., 2011) and pelvic cartilages (Li et al., 2007; Yue et al., 2011). A series of trials were conducted to further improve the selections of initial ranges, and the final selected ranges are shown in Table 7-2. It is expected that these selections covered the entire spectrum of possible ranges for the corresponding parameters.

Table 7-2: Initial ranges of parameters in the 1st stage of optimization for 10 YO femoral head GP

	K (Bulk modulus) MPa	C_1 (MPa)	C_2 (MPa)	C_3 (MPa)	C_4	C_5 (MPa)	C_6 (MPa)
Range	0.1~4	0.1~0.3	0.1~0.3	0.1~3	3~6	0.1~2	0~0.1

Sobol method (Esteco, 2014) was applied to generate the DOE space which can distribute the DOE samples randomly and evenly. A total of 56 DOEs were generated to assure the global coverage with a reasonable processing cost.

For each design in the DOE space, an adjacent local optimum was identified using the B-BFGS (Broyden-Fanno-Fletcher-Goldfarb-Shanno) algorithm available in modeFRONTIER. This algorithm was known as a classic gradient based extremum-searching algorithm with a relatively high convergent speed (Esteco, 2014). The B-BFGS algorithm automatically generated additional designs to calculate a “gradient matrix” and an approximation “Hessian matrix”. Through these two matrices, a “Newton step” was calculated to initialize the iteration. A new design was generated by adding the changing step (vector) to the old design. The termination accuracy was set as 1×10^{-4} which allowed the algorithm to stop when it cannot find a better OBJ function with

improvements higher than this convergence value. More details of the theory of this algorithm can be found in the modeFRONTIER manual (Esteco, 2014) and their technical report (Rigoni, 2003).

Upon termination, the local optimal result was obtained for this design. The same iterative process was performed for each of the other 55 designs in the DOE space. Among all the local optimal results, the one with the minimal OBJ_{low} was then treated as the global optimal solution of the first stage.

Optimization of the 2nd stage

The determined hyperelasticity parameters from the first stage of optimization were then brought to the second stage of optimization by simulating high-speed tests. In this stage, the viscosity option of MAT_92 was switched on, and the parameters for the two-term Prony series, S_1 , T_1 and S_2 , T_2 , were to be determined. The initial ranges are shown in Table 7-3, which were based on preliminary trials.

Table 7-3: Initial ranges / values of parameters in the 2nd stage of optimization for the femoral head GP of a 10 YO Child

	S_1	T_1 (ms)	S_2	T_2 (ms)
Range	0.5~0.9	50	0.01~0.05	1000

The optimization processes were similar to those in the first stage. The stress-strain curves in high-speed tensile and shearing loadings estimated for 10 YO femoral head GP were used as the target curves. The same Sobol method and B-BFGS algorithm were used. The original DOE number was 40. The termination criterion was set as 1×10^{-4} . Among the optimal local results from

the 40 designs, the one with the minimal OBJ_{high} was treated as the global optimal solution for the viscosity parameters.

After the viscosity parameters were determined, the overall optimization process for the femoral head GP of a 10 YO child was completed. At that time, all the parameters of the proposed material model of MAT_92 to represent the femoral head GP were determined.

The optimization processes for identifying the material properties of human femoral head GP are summarized and shown in Figure 7-3.

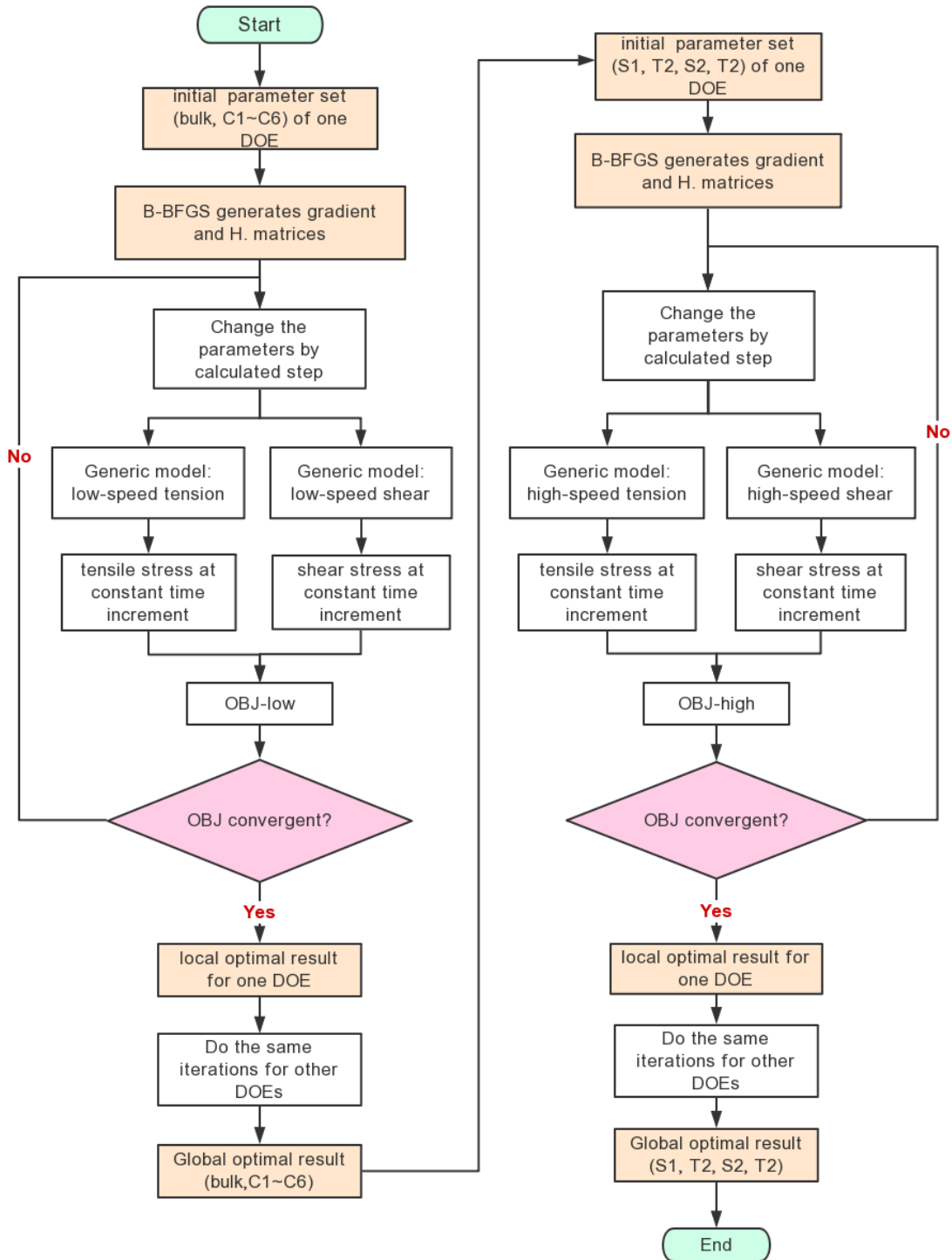


Figure 7-3: The flow chart of the complete optimization process for human femoral head GP material properties. The left half is for the hyperelasticity associated parameters (bulk modulus, C_1 ~ C_6) and the right half is for the viscosity associated parameters (S_i , T_i)

Optimization process for the GPs at knee region

The same set of optimization processes was conducted to optimize the material properties of 10 YO knee GPs. The initial ranges of the parameters in both the first and second stages are shown in Table 7-4.

Table 7-4: Initial ranges of parameters in both 1st and 2nd stages of optimization for the knee GP of a 10 YO child

	K (Bulk modulus) MPa	C_1 (MPa)	C_2 (MPa)	C_3 (MPa)	C_4	C_5 (MPa)	C_6 (MPa)
Range	0.1~4	0.1~0.3	0~0.2	0.1~1	3~6	0.5~3	-0.1~0.1

	S_1	T_1	S_2	T_2
Range	0.85~0.99	1000	0.005~0.05	30000

7.1.5. Material modeling results

The optimization results for the femoral head GP of a 10 YO child are shown in Table 7-5.

Table 7-5: MAT_92 parameters for the femoral head GP of a YO child

LS-DYNA Keywords	C_1 (MPa)	C_2 (MPa)	C_3 (MPa)	C_4	C_5 (MPa)	C_6 (MPa)
Value	0.22	0.10	0.785	4.0	1.0	0
LS-DYNA Keywords	K (Bulk modulus, MPa)	ρ (density, kg/mm ³)	S_1	T_1 (ms)	S_2	T_2 (ms)
Value	2.0	1.2E-6	0.80	50	0.02	1000

The simulation results using this set of parameters in the high-speed and low-speed tension are plotted as solid lines, along with the solid-dotted lines estimated for 10 YO children reported

in Chapter 6 are shown in Figure 7-4 (a). The comparison in shearing material modeling results for the femoral head GP of a 10 YO child are shown in Figure 7-4 (b).

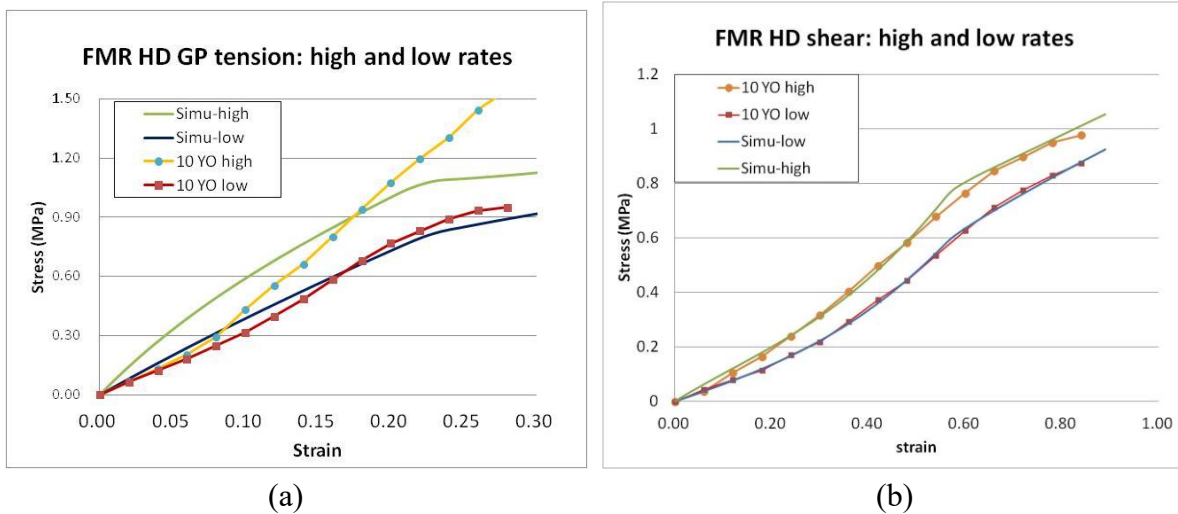


Figure 7-4: Engineering stress-strain curves of the femoral head GP of a 10 YO child, calculated by FE simulations with optimized GP material (market as “simu”), and estimated for 10 YO child from experimental study (market as “10 YO”). (a) tensile stress-strain curves comparison; (b) shearing stress-strain curves comparison

To avoid excessive computational cost, the medium rate tensile and shear stress-strain curves were not used in the optimization process. The assumption was that the stress-strain curves in the medium rate would be between the low-speed and high-speed curves. A verification for the medium rate responses was conducted using the optimized parameter set. The results for the femoral head GP of a 10 YO child are shown in Figure 7-5. It was observed that the material stress-strain relationships under the medium rate are close to those of the low rates, for both tension and shearing. The discrepancies were deemed acceptable.

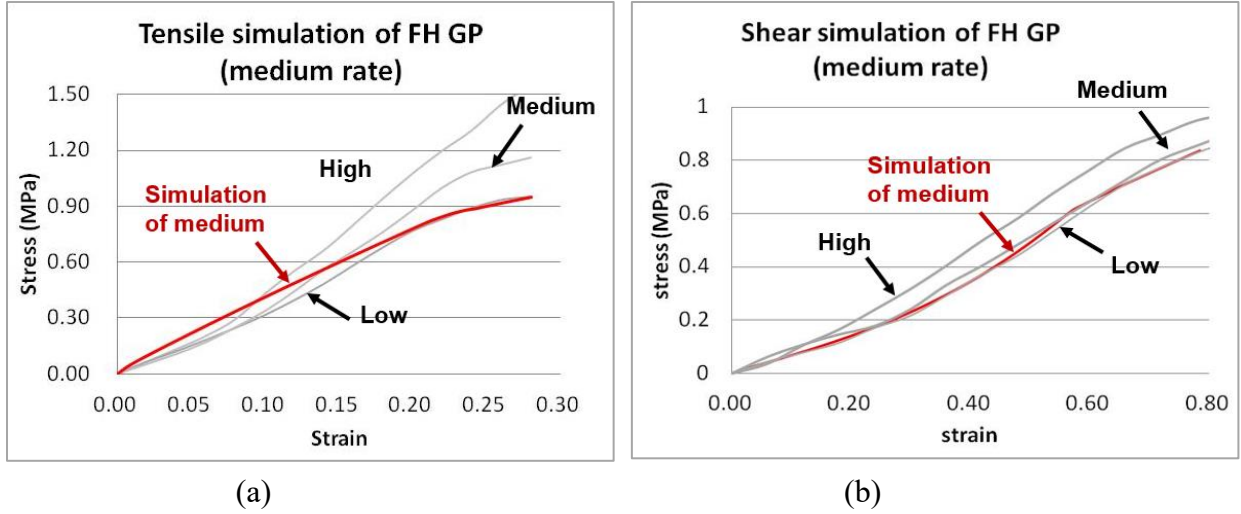


Figure 7-5: Verification at medium rate. The red curves are calculated from the simulations of medium strain rates, using the parameter set determined from the optimization processes. The grey curves were the estimated curves for 10 YO child from Chapter 6

The material optimization results for the knee GP's of a 10 YO child are shown in Table 7-6.

Table 7-6: MAT_92 parameters for the knee GP's of 10 a YO child

LS-DYNA Keywords	C_1 (MPa)	C_2 (MPa)	C_3 (MPa)	C_4	C_5 (MPa)	C_6 (MPa)
Value	0.174	0.095	0.295	4.0	2.33	0.075
LS-DYNA Keywords	K (Bulk modulus, MPa)	ρ (density, kg/mm ³)	S_1	T_1 (ms)	S_2	T_2 (ms)
Value	1.0	1.2E-6	0.98	1000	0.01	30000

The material modeling results for 10 YO knee GP is shown in Figure 7-6.

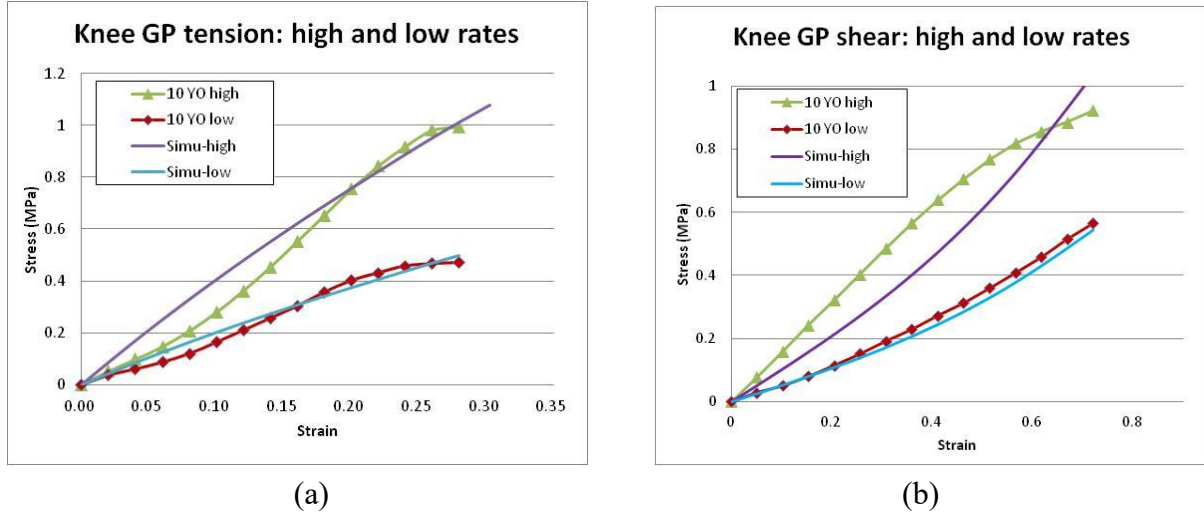


Figure 7-6: Optoimzation result of the knee GP for a 10 YO child. (a) tensile stress-strain curves comparison; (b) shear stress-strain curves comparison. The solid lines were from the simulations, while the solid-dot lines were from experimental study

7.2. MODELING OF PROXIMAL FEMUR WITH GPS

In this section, the sub-model of proximal femur was extracted from the PLEX baseline model. The femoral head GP was modeled using the geometry from CT scans of a 9.5 YO boy and the material properties derived in Section 7.1. A shearing loading was simulated as the experiments conducted by Chung et al. (1976). The GP modeling settings, such as the GP geometry representation (mesh density), perichondrial cartilage thickness and Young's modulus, the failure criteria of GP and cartilage, were investigated by parametric study. Since only one experimental study on human subjects was available serving as the correlation reference, the modeling techniques summarized from this section should be treated as preliminary results.

7.2.1. GP model generation

CT scanned images of the hip region from a 9.5 YO boy was acquired from ICAM during the collaborative anthropometric study. The height and weight of this subject were 1.46 m and 41.3

kg, respectively, which were higher than the current CHARM-10 whole-body FE model (i.e., namely 1.40 m and 35.0 kg). Based on the anthropometric study by Snyder et al. (1977), the standard deviations of height and weight of 9.5 to 10.5 YO children were 63 mm and 6.6 kg. Therefore, the height and weight of this subject were considered close to the average values of 10 YO children. The CT scans had resolutions of 0.5075, 0.5075, and 0.625 mm in the lateral-medial, anterior-posterior, and vertical directions, respectively. Mimics (v. 12.0, Materialise, Leuven, Belgium) was used to view and preprocess the images, as shown in Figure 7-7 (a). Then the 3D CAD was reconstructed in Mimics and cleaned in HyperMesh. The external surfaces of the femur and the proximal surface of the GP were shown in Figure 7-7 (b) and (c), respectively.

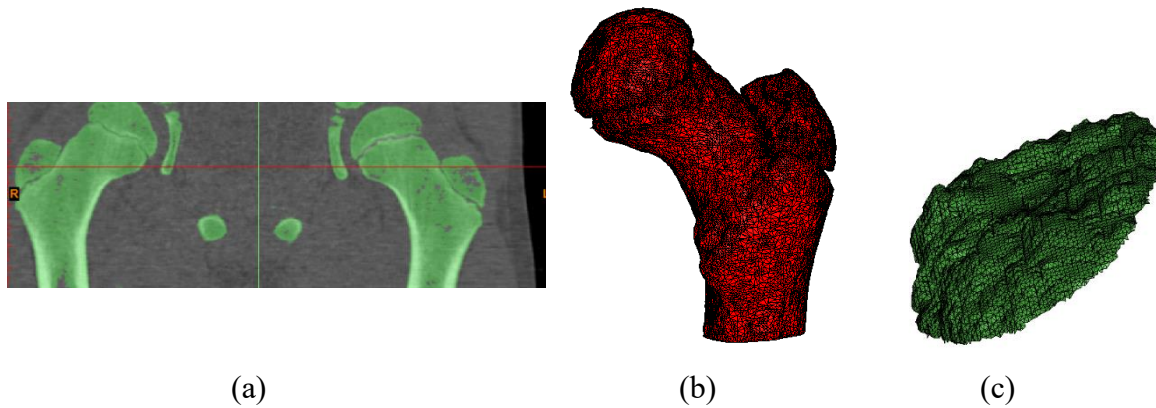


Figure 7-7: 3D reconstruction of the proximal femur and femoral head GP based on CT scans of a 9.5 YO boy. (a) One slice of CT scan in the coronal plane in Mimics. The dense regions were colored in bright green, while the non-bony tissue or cavities were colored in grey in Mimics; (2) Extracted outer surfaces of the left proximal femur bone, and (c) The proximal surface of the left femoral head GP, meshed by triangular elements in Mimics

A measurement on the reconstructed CAD model was conducted. The proximal surface of the GP was then scaled and realigned to fit the proximal femur meshes of the current sub-model, as shown in Figure 7-9 (a). The GP surface was reconstructed to two models using two different levels

of mesh density: The lower density mesh had 72 quadrilateral elements with the length of sides from 2.10 to 5.62 mm, while the higher density one had 288 quadrilateral elements with the length of sides from 0.98 to 2.97 mm. The finer meshes demonstrated more details of the irregularity of the original surface, but would cost more computational resources. In both models, the 2D meshes were dragged along the femoral neck axis to build the 3D plates representing the GP, as shown in Figure 7-8 (b) and (c). The thickness was set as 1.35 mm, which was consistent with the thickness measurement on the child femoral head GP, conducted by Williams et al. (2001).

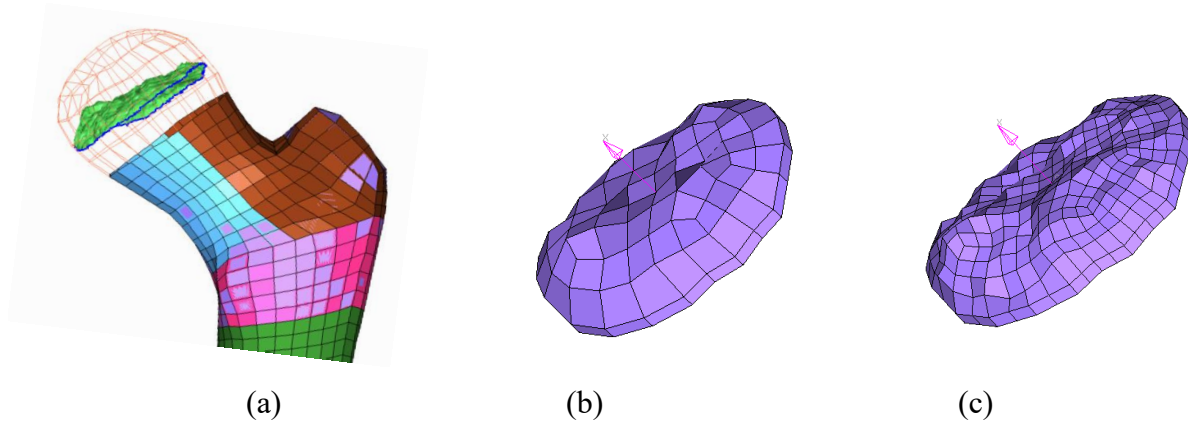


Figure 7-8: Reconstruction and modeling of the femoral head GP. (a) The proximal surface of GP extracted from the CT scans was scaled and located to the correct place in CHARM-10 proximal femur. 2D quadrilateral elements were used to reconstruct the GP proximal surface. A total of 72 elements (b) and 288 elements (c) were used to investigate which mesh density is better. The 3D plates of the femoral head GP were generated by dragging the 2D surface by 1.35 mm along the axial direction of the femoral neck

The circumferential nodes were manually moved to the surface of the original cortical shells of the baseline sub-model. The trabecular bones surrounding the GP were then re-meshed while maintaining the nodal connections between the GP and surrounding bones. According to the measurements reported by Chung et al. (1976), the average thickness of the perichondral cartilage

around the femoral head GP was 16.0% of the GP cross-sectional radius. The radius of GP in the current sub-model was 31.8 mm, so the thickness of cartilage would be 2.5 mm. The mid-sectional view of the proximal femur with the lower density mesh of GP is shown in Figure 7-9.

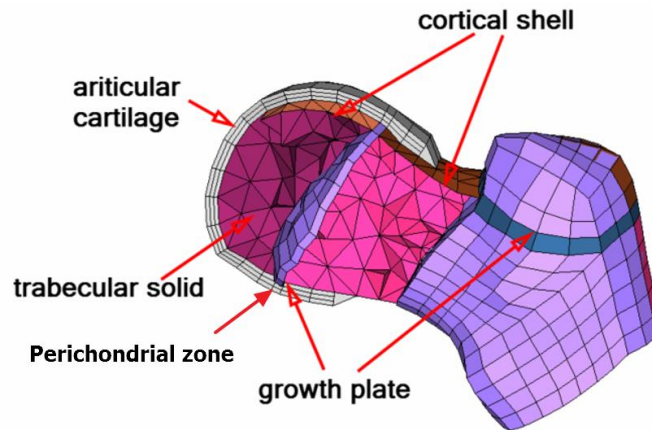


Figure 7-9: Details of the proximal femur FE sub-model with the GPs embedded the GPs. The lower mesh density model is shown here

The GP in the greater trochanter was modeled as a single layer of solid elements extracted from the preexisting solid elements. The same set of material properties of the femoral head GP was assigned to this GP since no experimental data on human greater trochanter GP were found in the literature. The material axis of the greater trochanter GP was set to be perpendicular to the cross-sectional surface of the meshed greater trochanter plane.

7.2.2. Parametric study in shearing load

The material properties of MAT_92 for the 10 YO femoral head GP (as shown in Table 7-5) were assigned to the updated proximal femur model. A pin loading in the anterior-posterior direction was modeled to simulate the experiment conducted by Chung et al. (1976), as shown in

Figure 7-10. Since the experiment applied an extremely slow quasi-static loading, the simulation in the same speed (2 mm/min, i.e. 0.003 s^{-1}) would take days and was not feasible for the FE parametric study. A higher loading speed of 0.34 mm/ms was adopted and the viscosity terms of MAT_92 was disabled. It had been verified the viscosity effect in a higher loading rate (the medium rate of 0.163 s^{-1}) was neglectable as shown in Figure 7-4 (b) and Figure 7-5 (b). Therefore, the viscosity effect in the quasi-static loading speed as used in the Chung's tests would be neglectable.

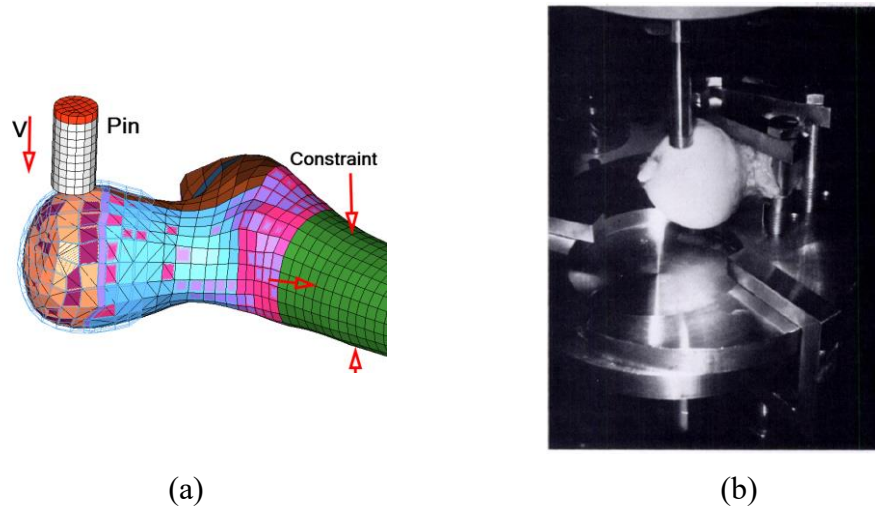


Figure 7-10: The femoral head GP shearing test. (a) The FE model with a higher loading speed with the viscosity of the GP material disabled. (b) The setup of the shearing experiment carried out by Chung et al. (1976)

The cartilage was modeled as solid elements using an elastic material. The Young's modulus was estimated from literatures. In the tensile tests conducted on the bovine distal femur by Cohen et al. (1992), the measured Young's modulus was 84 MPa for the articular cartilage and the 35 MPa for the GP. A ratio of 2.4 between the cartilage and GP was derived and then implemented to estimate the Young's modulus of the femoral head cartilage of a 10 YO child. As shown in Figure

7-1, the linear fit of the tensile stress-strain curve of the femoral head GP was 3.3 MPa. As a result, the Young's modulus of this cartilage was approximated as 7.9 MPa ($3.3 \text{ MPa} \times 2.4$).

In Chung's study, the perichondrial complex, i.e. the cartilaginous tissue surrounding the GP was dissected to investigate the influences of the complex on the shearing strength. It was found that, with the cartilage, the ultimate shearing force (P_t) would be 15% larger than that of the femur sample without cartilage (P_p). Therefore, in the FE model, the cartilage was also removed to simulate this shearing effect on the dissected femur samples. The ultimate shearing forces were captured from the models with and without cartilage ($P_{t\text{-simu}}$ and $P_{p\text{-simu}}$). The shear strength τ_{\max} was calculated by dividing the P_t by the original cross-sectional area at the GP level. A linear fitting curve was drawn to estimate the relationship between shear strength and the age, as shown in Equation 7-7, which was derived by Chung et al. (1976).

$$\tau_{\max} = 6.56 + 0.55 \times \text{Age} \quad 7-7$$

τ_{\max} was in kg/cm^2 and "age" was in year. For 10 YO group τ_{\max} was 12.06 kg/cm^2 , i.e., 1.195 MPa. The ratio of ultimate shear force (P_t/P_p) was also reported for each age group. P_t/P_p for 10 YO group was 1.14. Since the displacement histories were not reported, the comparison was not performed for the deformation history in the whole process. The von Mises strain was used as the failure criterion of femoral head GP. This failure strain was tuned to match the two outcomes, namely τ_{\max} and P_t/P_p at the failure point of the femoral GP. The maximum principal strain was taken as the failure criterion for cartilage, and it was tuned in a manner that the cartilage failure

and GP failure happened at the same time. The material parameters and the failure criteria tuning results are shown in Table 7-7.

Table 7-7: Material properties of the major components in the upgraded proximal femur FE model for the PLEX modeling

Part	Properties	Failure criterion
Cartilage	Elastic, E=7.9 MPa (2.4 times of the GP tensile modulus. The ratio was from Cohen et al. (1992), Thickness=2.5 mm (Chung, et al., 1976)	Max. principal strain: 0.35 (from tuning)
FH GP	MAT_92, the estimated 10 YO femoral head	Max. von Mises strain:
GT GP	GP material properties from Section 7.1	0.80 (from tuning)

Note: FH: femoral head; GT: greater trochanter.

The shearing force vs. displacement relationships were plotted for the models with and without the cartilage. The two models with lower and higher element densities were used in the shearing simulation. The results are shown in Figure 7-11 and Table 7-8.

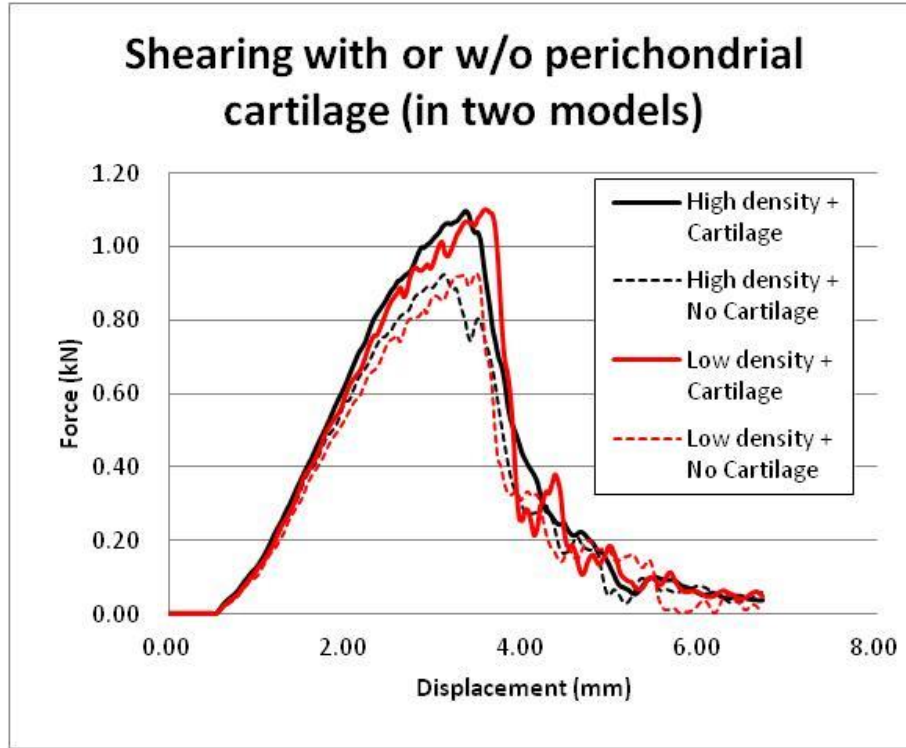


Figure 7-11: Force displacement histories for the updated femoral head models. The solid curves are from the model with perichondrial cartilage, and the dot curves are from the model without perichondrial cartilage. Both the higher and lower mesh density models were used for this analysis

Table 7-8: Simulation results compared to the test results by Chung et al., 1976

	Shear Strength (τ_{max})	Shear force ratio with & without cartilage (Pt/Pp)
Chung et al., 1976	1.195 MPa	1.14
FE model (lower mesh density)	1.186 MPa	1.19
Error	-0.75%	+4.4%
FE model (higher mesh density)	1.188 MPa	1.19
Error	-0.59%	+4.4%

It was observed that that both the lower and higher mesh density FE models showed reasonable agreement with the experimental results as reported by Chung et al. (1976). It can be found that the differences between the FE models with higher and lower mesh density were not significant. Based on this finding, it was decided that the lower mesh density model would be embedded into the whole-body pedestrian model of 10 YO child, because it was considered as a balance between the modeling accuracy and computational cost.

The other modeling settings as shown in this section was verified as valid, such as the GP geometry aligning, extracting a one-layer of elements to represent the GP and remeshing the surrounding bones, perichondrial cartilage thickness of 2.5 mm, cartilage's Young's modules of 7.9 MPa, and the failure criteria for the GP (max. von Mises strain of 0.80) and cartilage (max. principal strain of 0.35). These techniques would be referenced for the following GP modeling in the whole PLEX model.

7.3. WHOLE-BODY PEDESTRIAN MODEL WITH GPs IN THE PLEX

The material models and modeling techniques were implemented into the baseline CHARM-10 model as an application of whole-body child pedestrian impact. Similar to the modeling process of the GP at the proximal femur sub-model, the other GPs in the PLEX were modeled, so that the baseline PLEX model and the whole-body pedestrian model were advanced by including GPs. The updated whole-body pedestrian model was used in an SUV-to-pedestrian impact scenario, and the mechanical influences of the GPs were discussed. It should be noted that, because the whole-body pedestrian impact simulation was not validated to any realistic experiments, the findings obtained

from the simulation study of this section should be treated as technical applications with preliminary results thus far.

7.3.1. GP closure age examination

The closure ages of GPs were checked to confirm which GPs were not calcified by age of 10. The closure ages of the GPs for six different locations in the PLEX are summarized in Table 7-9. The ischiopubic ramus GP should be already calcified for a 10 YO child. Distal tibia GP was not included yet at the current modeling stage. the other GPs were included in the updated CHARM-10 model.

Table 7-9: Closure ages of the GPs in the PLEX

No.	Name	Closure age	Literature
1	Triradiate cartilage	15-18	Peterson (2007)
2	Femoral head GP	12-19	Scheuer et al. (2000)
3	Greater trochanter GP	14-18	Scheuer et al. (2000)
4	Ischiopubic ramus GP	4-7	Ogden (2000)
5	Distal femur GP	14-20	Scheuer et al. (2000)
6	Proximal tibia GP	13-19	Scheuer et al. (2000)
7	Distal tibia GP	14-18	Scheuer et al. (2000)

7.3.2. PLEX model updated with GPs

The GPs at the distal femur, proximal tibia, and the acetabulum (triradiate cartilage) were additionally modeled using the same strategy as in the proximal femur sub-model, as described in Section 7.2. Generally, the GPs were modeled as one layer of 8-node solid elements. Modeling of these GPs were done by rebuilding a layer of elements at GP position in the baseline model, and assigning the corresponding GP materials. Necessary local remeshing was performed to maintain

the mesh connectivity and smoothness. Figure 7-12 (a) shows the result of the knee GPs modeling, where the shapes in anatomy books (Moore et al., 2011; Ogden, 2000) were referred to. For the triradiate cartilage, CT scans from the same subject of 9.5 YO body, as mentioned in Section 7.2, were used, and are shown in Figure 7-12 (b). The geometry from the CAD model was approximately referred to. The material properties estimated for the 10 YO child knee GPs, described in Section 7.1.5, were assigned to the knee GPs. The material properties of the acetabulum cartilage (hyperelastic rubber as shown in Table 4-7) were assigned to the triradiate cartilage, since they were essentially fused together.

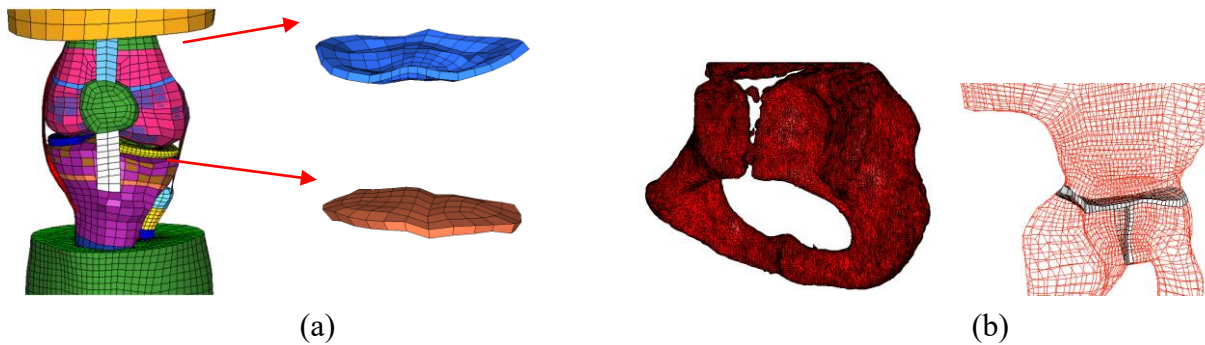


Figure 7-12: GP embedding: (a) GPs at the knee joint (distal femur and proximal tibia) (b) Triradiate cartilage. The shape and morphological details of these GPs were approximate and not as accurate as the femoral head GP

The updated PLEX model is shown in Figure 7-13. In the pelvic region, the femoral head (FH) GP, greater trochanter (GT) GP, and triradiate cartilage (TC) were modeled. In the knee joint region, the distal femur (DF) GP, and the proximal tibia (PT) GP were modeled. The updates were also applied to the whole-body FE model, CHARM-10 pedestrian model. In the baseline CHARM-10 pedestrian model, the elements at the location of a GP were included as a part of the surrounding

trabecular bone. The Young's moduli ranged from 250 to 770 MPa for trabecular bones in the long bones in the PLEX, and was 44.8 MPa for the pelvic trabecular bone (as previously shown in Table 4-7). Besides, there were cortical shells in the baseline model, whose Young's moduli ranged from 0.85 to 14.9 GPa. In the updated model with GP, the elements for previous trabecular bones were assigned with GP material models (with elastic moduli less than 10 MPa in quasi-static tension), and the cortical shell elements were replaced by perichondrial cartilages (Young's modulus was 7.9 MPa as determined in Table 7-8). The significant differences between the baseline and updated models, in terms of the material elastic moduli, implied the stress distributions should be remarkably different for the two models.

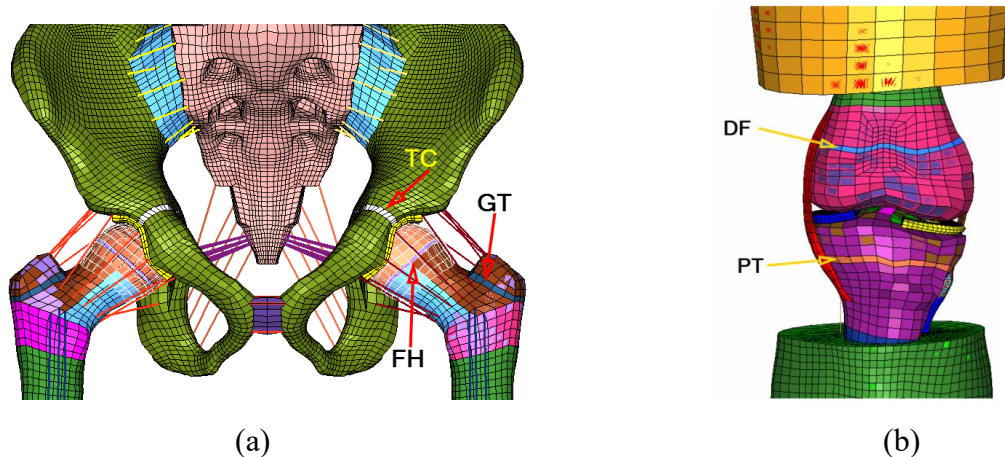


Figure 7-13: The updated PLEX model of the 10 YO child with GPs embedded: (a) The pelvic region and (b) The knee region. Some soft tissues were hidden for better viewing. TC: triradiate cartilage, GT: greater trochanter, FH: femoral head, DF: distal femur, PT: proximal tibia

An SUV-to-pedestrian impact scenario was simulated for conducting the parametric study to investigate the mechanical influences of the GPs. The updated CHARM-10 was standing upright and the SUV struck from the lateral direction at a speed of 5.0 m/s (Figure 7-14). The SUV model

was downloaded from the website of NCAC (National Crash Analysis Center) and simplified to represent the front portion of a 2002 Ford Explorer. The simulation was performed using LS-DYNA (v. 971, R6.1, Livermore Software Technology Corporation, Livermore, CA).

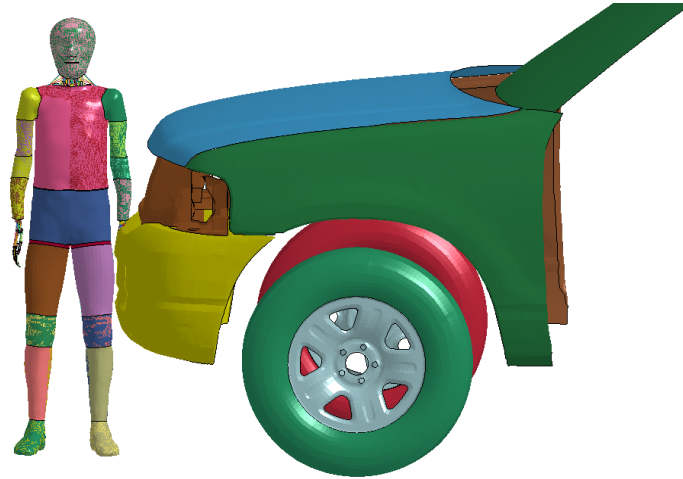


Figure 7-14: Simulation setup of the SUV-to-pedestrian impact

At this point, the failure criterion in MAT_92 in LS-DYNA is sensitive to the loading condition. As a result, the ultimate von Mises strain criterion of GP derived in Section 7.2 from the femoral head shearing may not be valid for complex loadings applying to the GPs in a real-world pedestrian impact. Consequently, the 10 YO pedestrian model included GPs in the PLEX without failure settings. To quantitatively assess the mechanical influences of GPs in the PLEX, the baseline model of CHARM-10 without GPs was also used under the same SUV-to-pedestrian loading condition. Additionally, the deformations of the GPs during the impact were monitored for discussing the probability of material failure.

7.3.3. Pedestrian impact simulation results

Contours of the maximum principal strain (MPS) for cortical bones at the pelvis (shell elements), femoral shaft (solid elements), and tibia shaft (solid elements) were shown for the baseline and updated CHARM-10 models. The contours of strain distribution were captured at 14 ms from the initial contact for acetabulum and femoral shaft. The contours at 20 ms for the tibia shaft were plotted. The results of the baseline model are shown in Figure 7-15, while the results of the updated model are shown in Figure 7-16.

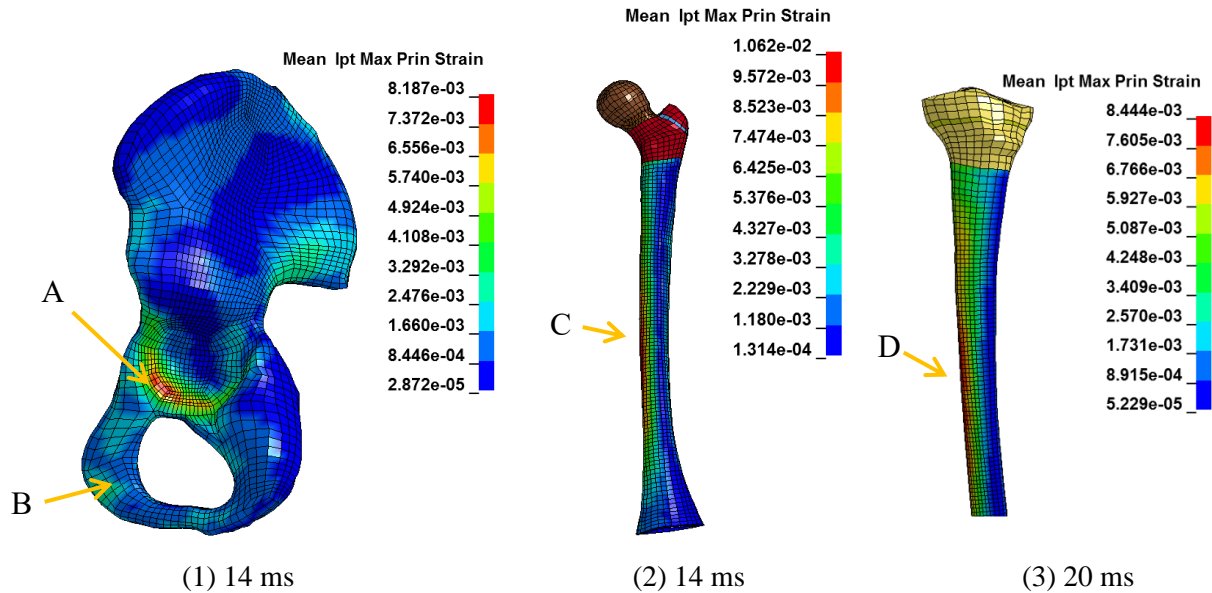


Figure 7-15: The Maximum Principal Strain (MPS) contours of the simulation using the baseline CHARM-10 model. The unit of the countour is GPa. The four cirtical regions are: (A) bottom of acetabulum, (B) ischiopubic ramus, (C) the medial side of femoral shaft, and (D) the medial side of tibia shaft. Only cortical bones are presented in these figures

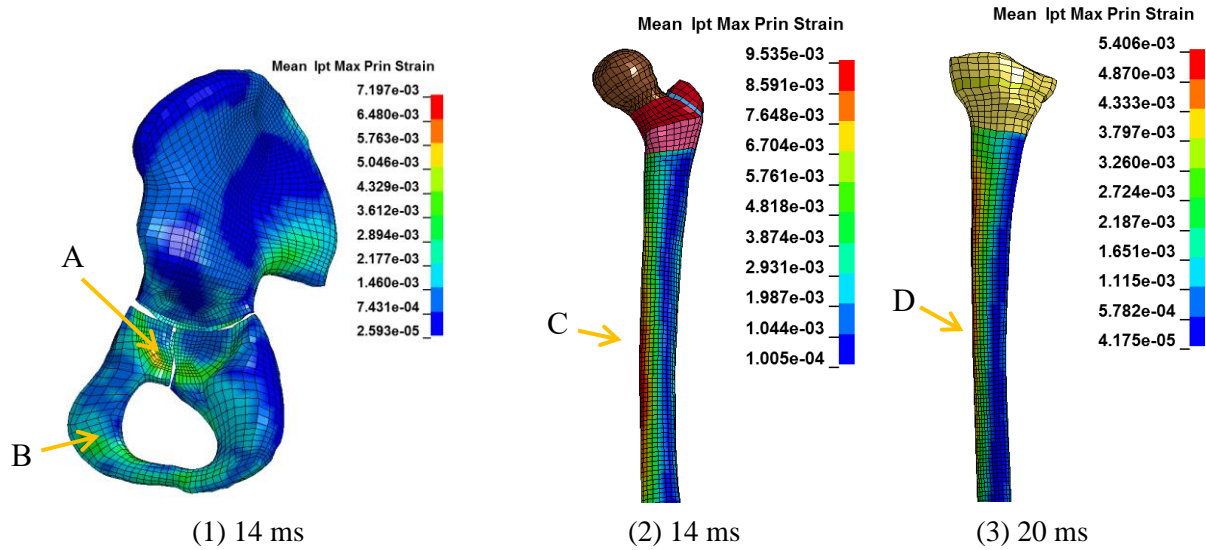


Figure 7-16: The Maximum Principal Strain (MPS) contours of the simulation using the updated CHARM-10 model including the PLEX GPs

Four critical sites where fractures may occur were monitored: (A) bottom of acetabulum, (B) ischiopubic ramus, (C) medial side of the femoral shaft, and (D) medial side of the tibia shaft. The MPS of the same elements at each site from the baseline and updated models were plotted in Figure 7-17 to evaluate the strain changes. It should be remarked that the elements where the MPSs were measured were at least 10 mm away from the boundaries of the GPs in the updated model, to avoid capturing the MPS values from the elements with abrupt stresses change due to the boundary effect.

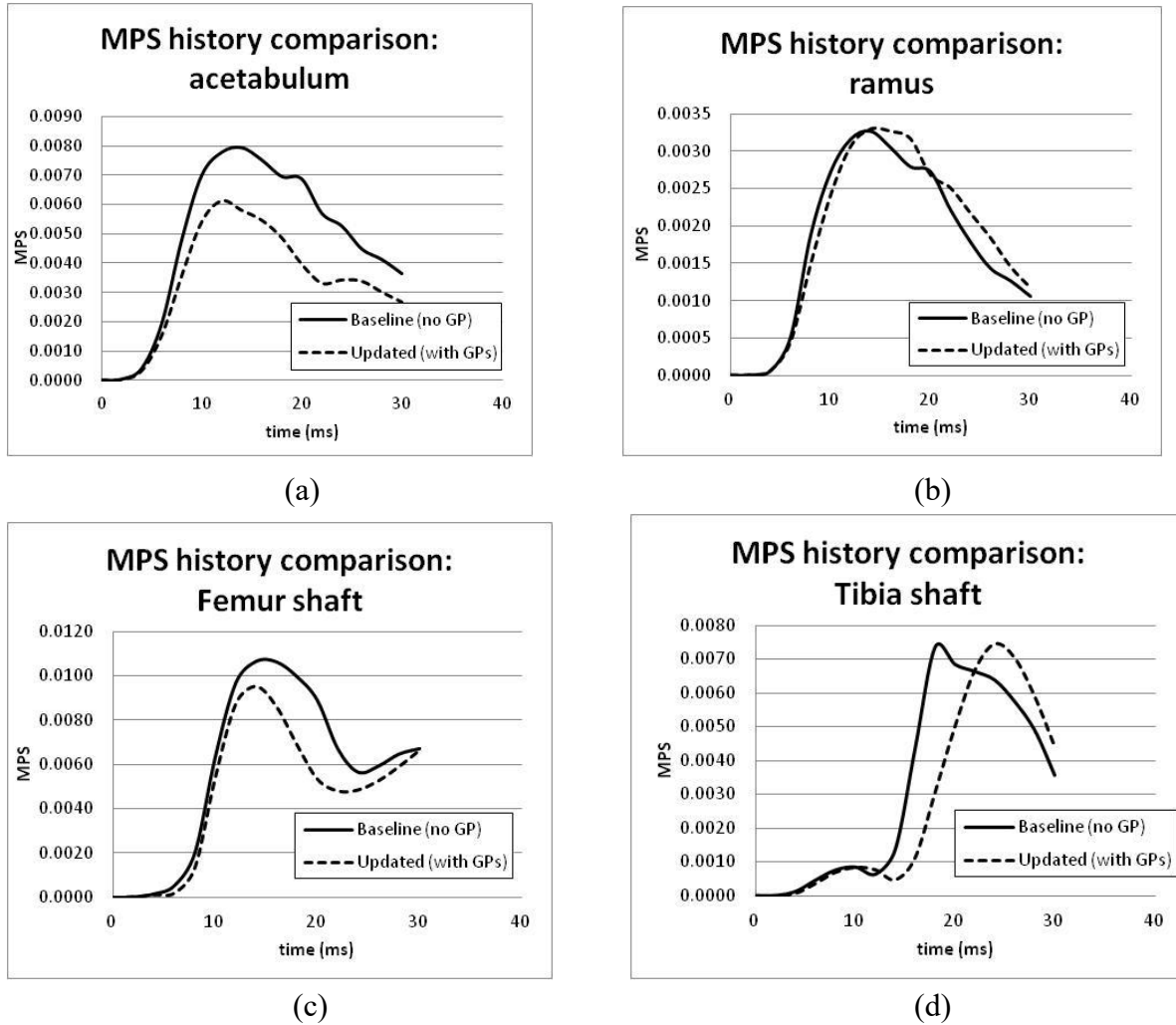


Figure 7-17: The MPS history comparisons between the baseline model (without GP) and updated model (with GPs), at four monitored locations. (a) at location A; (b) at location B; (c) at location C; (d) at location D

It was noticed that the MPS histories for acetabulum bottom and femur shaft were changed in terms of the magnitude. With GPs, the peak MPS at the acetabulum bottom was reduced by 23.0%, and it was reduced by 10.4% for location B at the medial side of femoral shaft. The peak value of MPS at the tibia shaft was not significantly changed after embedding the GPs (decreased by 0.7%), but the timing of the peak changed apparently (18 ms to 24 ms). Both the value and

timing of the peak MPS did not significantly change at the ischiopubic ramus after the embedding the GPs.

The strain distribution in the GP was further analyzed. The MPS contours of the GPs in the proximal femur and knee are shown in Figure 7-18 (a) and (b), respectively. Nodal displacements of four elements with peak MPS within a GP were examined to analyze the strains.

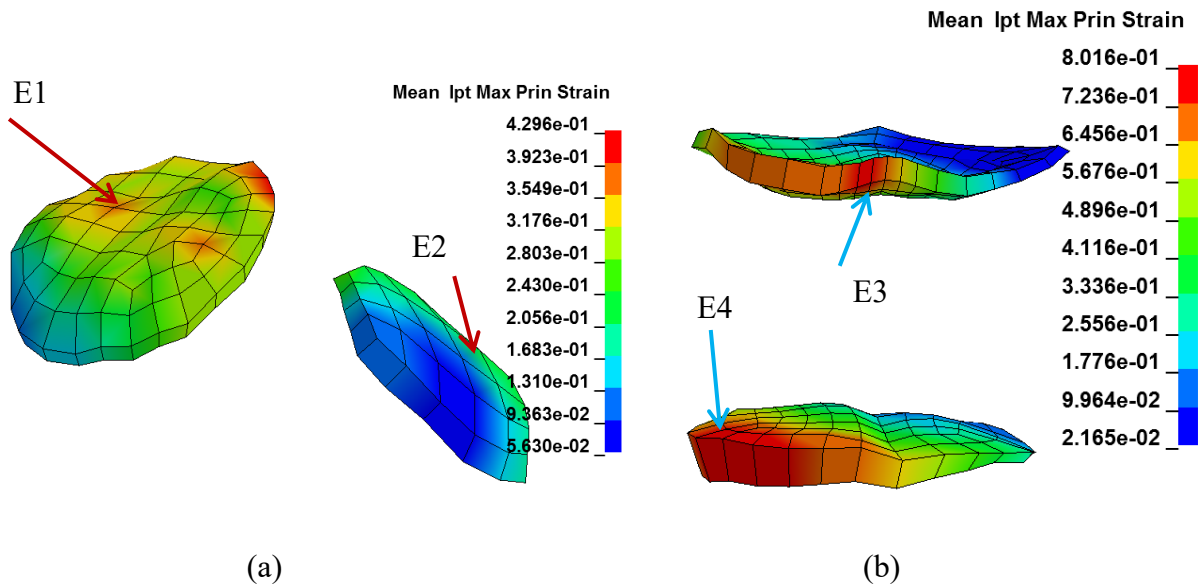


Figure 7-18: MPS distribution of (a) proximal femur GPs (FH and GT), (b) knee GPs (DF and PT). $t=22$ ms. The elements under arrows are the elements of interest, and are used for local deformation analysis

The ultimate strain (engineering) values from the experimental study in Chapter 6 were taken as references. The ultimate tension strain at the material axis was 30% and the ultimate shearing strain perpendicular to the material axis was 90%. Both criteria were implemented to evaluate the failure probabilities.

For E1 element from the FH GP, the maximal engineering shear strain was 0.67, and the maximal tensile strain was 0.10, which were both below the aforementioned failure criteria. For

E2 element from the GT GP, the maximal shear strain of 0.56, which was below the shearing failure criterion. In the material axis, the normal strain was compression, which did not lead to a failure here. Both GPs at the proximal femur showed lower probability of failure.

Similarly, for E3 from the DF GP, the maximal shear strain was 0.10 and the maximal tensile strain was 1.01. For E4 from the PT GP, the maximal shear strain was 0.54 and the maximal tensile strain was 1.16. The shear strains were below the shearing failure criterion. The tensile strains from the knee GPs were remarkably higher than the tensile threshold, i.e. 0.30 in the material axis.

These findings suggested that, in this pedestrian impact scenario, the knee GPs would be failed due to excessive tension along the fiber direction, while the GPs in the proximal femur had lower risks of failure.

It should be noted that if the striking vehicle is a sedan with a much lower height of the leading edge, the failure due to excessive shear strain is also possible. It has been preliminarily verified in an early study by Shen et al. (2015b), using simple elastic material models for the GPs. In that study, the sedan-to-pedestrian impact was at 10 m/s (similar as previously shown in Table 4-6), and the element deletion on the GPs apparently change the stress distribution significantly, avoiding the failures of the cortical bones in the long bones.

It can be summarized that the presence of GPs in the PLEX would change the stress and strain distribution at the acetabulum bottom, femoral shaft and tibia shaft, in terms of the peaks or/and the phase in the time domain. The effect on the pelvic ramus would be minor. In an SUV-to-pedestrian impact in 5 m/s, the knee GPs would be failed due to tension and the failures would

start from the medial side of these two GPs. The GPs in the proximal femur showed lower failure risks. In a sedan-to-pedestrian impact in 10 m/s, the knee GPs may be failed due to the shearing loads. Once a failure of GP happened, the stress distribution would be changed dramatically, and the risk of failures on cortical bones will be much reduced, compared to the baseline model without GPs.

7.4. CHAPTER DISCUSSIONS

7.4.1. Mesh convergence of the specimen FE model

A mesh convergence study was performed to determine an appropriate mesh density considering both the simulation accuracy and computational cost. Three more specimen models with different mesh densities were built, and the numbers of the elements in the GP are 25, 675, 4,500 (baseline), and 36,000, respectively (Figure 7-19).

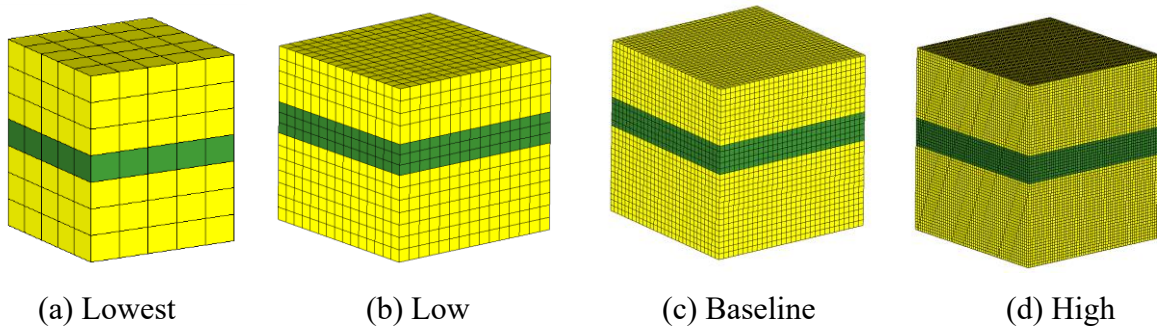


Figure 7-19: FE models of a specimen with different mesh densities. The numbers of elements for the GP only (shown as a layer of green elements in each model above) are (a) 25, (b) 675, (c) 4,500, and (d) 36,000, respectively

The material property of human femoral GP determined in Section 7.1.5 was used to verify the mesh convergence by varying mesh densities. The tensile and shear simulations were conducted with loading speeds of 0.3 mm/ms. The tensile stress at 0.3 tensile strain, and the shear

stress at 0.75 shear strain were extracted for discussion. The results of the four models with different levels of mesh density are shown in Figure 7-20. For the tensile stress at 0.3 tensile strain, with the mesh density increasing from the lowest to the highest levels, the tensile stress increased by 2.6%, 0.028%, and 0.012% of the value obtained from model with the lowest mesh density. For the shear stress at 0.75 shear strain, with the increasing mesh density from the roughest mesh to the fine, the shear stress decreased by 5.02%, 0.53%, and 0.19% of the value obtained from the roughest model. This suggested that the convergence had been achieved when the “baseline” mesh density was adopted in both tension and shearing.

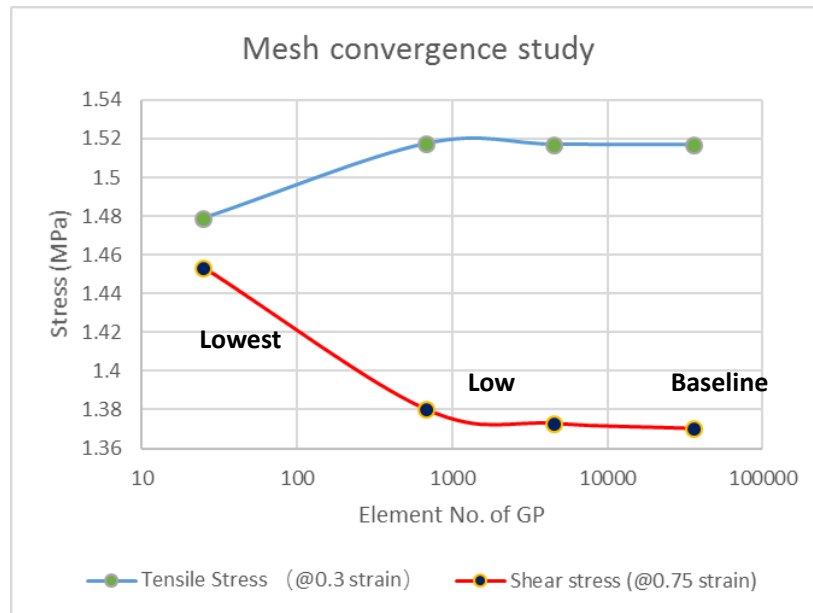


Figure 7-20: Simulation results of FE models with different mesh densities

7.4.2. Material axis

There were six options in MAT_92 to define the material axes in each element, since the fiber orientation is critical. Two most usual methods to determine the material axes are: 1) by the element nodes, and 2) by a vector. For the first method, the keywords in MAT_92 should be set as AOPT=0, and the node numbers of every element need to be carefully ordered so that the material axis of this element could be automatically generated. In this case, the fiber orientations of different elements are not necessarily identical, since the element orientations could be different, as shown in Figure 7-21 (a). For the second method, the keywords in MAT_92 should be set as AOPT=2 (using 2 pairs of nodes in the material), or AOPT=-CID (CID identifies a local coordination system) to define a common vector for the material axes. The material axes for all the elements are identical and defined by the same vector, as shown in Figure 7-21 (b). The fiber orientation of each element is indicated by the C axis of the local orthotropic coordinate system in the figure. It can be observed that the GP part has element-dependent orientations in the first method (by element nodes) and has identical fiber orientations for all elements in the second method (by vector). When the GP elements have un-ordered element numbers, the material axes discrepancy between the first and second methods may become even larger.

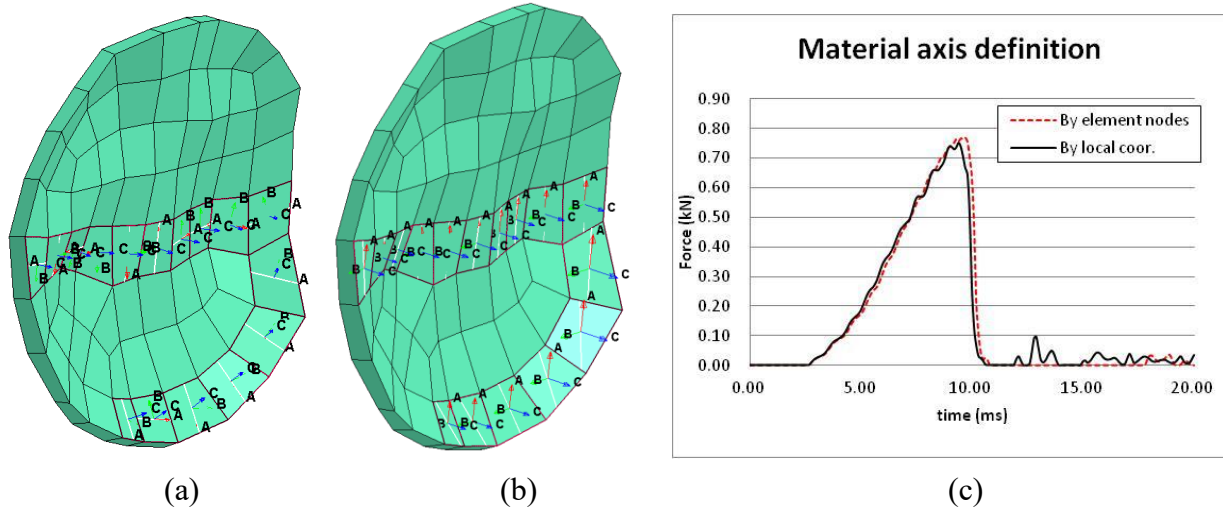


Figure 7-21: Material axes for elements in GP using different methods: (a) by element nodes, (b) by a vector. The local orthotropic axis for each element is shown by letter A, B, and C, while C is indicating the fiber orientation. It is noted that in both method, the fiber orientation in one element will be updated in each time step of the simulation. (c) is showing the shearing force difference between two GP models using these methods, respectively

These two methods were used for the GP modeling under the shear loadings. The failure criterion was set if the maximum effective strain (V-M strain) exceeded 0.80. It was found the overall stress was not changed significantly, and the failure strain would be larger for the element nodes method.

The histologic studies such as the ones conducted by Ogden (2000) and Peterson (2007) revealed that the GP material orientation is basically along the growth axis, and not sensitive to the local GP interface inclination. From this point of view, the second method provides a more reasonable numerical means to define the material orthotropic axes within the MAT_92 material.

7.4.3. Strain rates measured from whole-body pedestrian simulation

In the current experimental study on the porcine specimens, the highest tensile strain rate was 1.91 s^{-1} and the highest shear strain rate was 3.04 s^{-1} , which were not as desirable as the one

reaching high enough to that in a real-world pedestrian impact. Nevertheless, although the current whole-body model was not fully validated, the measurements based on this FE model can provide beneficial insights for estimating the strain rate levels of the GPs in the PLEX under such loading condition as that in Section 7.3, i.e. 5.0 m/s lateral impact.

The 1st Principal strain rate was taken as the output parameter by using LS-PrePost (v.4.3, Livermore Software Technology Corporation, Livermore, CA). The highest peak value was 647 s⁻¹ for the triradiate cartilage, and the lowest peak value was 63.3 s⁻¹ for the great trochanter GP. The complete results are shown in Table 7-10.

Table 7-10: The maximum 1st Principal strain rates at the GPs in the PLEX in SUV-to-pedestrian impact simulation (5.0 m/s)

Region	TC	FH	GT	DF	PT
Strain rate (s ⁻¹)	647	646	63.3	193	136

As expected, the measured strain rates from the above simulation were higher than those of the porcine tests by several orders of magnitude. It suggested that the current material models from Section 7.1 would be unreliable in a high dynamic loading. The optimization results based on the current stage of experimental study should be treated as an initiative investigation of the GP material behaviors and subsequent material modeling. In the future phase of study, dynamic loading at higher strain rates, above 600 s⁻¹, should be planned on further improving the material model under very high strain rates.

7.5. CHAPTER SUMMARY

A transversely isotropic hyperelastic material model (MAT_92 in LS-DYNA) was chosen for the material modeling of GP. Through two stages of material optimization, the hyperelastic parameters of MAT_92 and the viscosity parameters were optimized, for both 10 YO femoral head GP and knee GPs. A good match for the shearing properties in all strain rates has been achieved between the stress-strain curves using the newly-obtained material and those estimated for 10 YO in Chapter 6. The tensile properties showed good matching at the low and medium strain rates, and acceptable matching at the high strain rate in this experimental study.

A detailed sub-model of the proximal femur region was established, including the geometric data of GPs from CT scans. The femoral head anterior-posterior shearing was simulated to mimic the experiments conducted on human subjects as reported by Chung et al. (1976). A reasonable agreement was achieved in the parametric study, so the GP modeling techniques implemented in the sub-model should be considered as good preliminary references for future GP modeling studies.

As an application for pedestrian simulation, other GPs in the PLEX were then modeled in the similar means of the femoral head GP as a technical application. All the unfused GPs in the PLEX were included in the updated PLEX model and further whole-body 10 YO pedestrian FE model. An SUV-to-pedestrian impact scenario was simulated at an impact speed of 5.0 m/s. The stress and strain distribution analysis revealed that: the presence of GPs in the PLEX would change the stress distribution and reduce the MPS at acetabulum bottom, femoral shaft, tibia shaft, but did not change the MPS at the pelvic ramus significantly. The deformation analysis on the elements

suggested that the knee GPs would have failed due to tensile strain along the material axes. The GPs at the proximal femur showed lower risks of failure. The knee GPs may be also failed due to shearing loads if the striking vehicle is a small sedan. The failure of the GPs would change the stress distribution dramatically and avoid the failure of cortical bones in the long bones.

CHAPTER 8. LIMITATIONS AND FUTURE WORK

8.1. LIMITATIONS

10 YO PLEX baseline modeling

Due to regulatory and ethical concerns, the pediatric PMHS data were insufficient for comprehensive material modeling and FE model validation. As a result, the baseline 10 YO PLEX model and CHARM-10 should be considered as not completely validated. Some material properties were directly adopted from adult experimental studies. Some advanced material models in adult human body models were not applied to the current child model. Some material properties were scaled from adult data, and these scaling laws yet require more pediatric PMHS data for further validations. The MADYMO 10 YO pedestrian model, a numerical model using the multi-rigid-body approach which was not fully validated, was used to provide responses for comparison with those from the 10 YO FE pedestrian model. The qualitative and quantitative comparisons provided indirect evidence about the prediction capability of the whole-body child pedestrian model, with obvious limitations.

Experimental tests

In terms of experiment design and investigation in the current study, the highest strain rate was still considered to be much lower than possible severe loading conditions on a child, such as the estimation in Section 7.4.3. It should be noted that some other influencing factors, such as the gender, the weight/size of a piglet, and the location of a specimen within one GP, etc., were not fully considered at this stage. But it should be pointed out that the effect of the location within one

GP had significant differences on shear moduli as reported by William et al. (1999) under the shearing loads. With an enlarged sample size (piglet number), more specimens tested and a full-factorial DOE, the mechanical properties of the GP could be better understood, and the material models of GP could be consequently improved.

The system intrinsic stiffness was calculated by an additional stepwise loading test using a trabecular bone held in the specimen position, with the two grip pairs in the average distance of the GP tests. This process was designed to compensate the system deformation including trabecular bone. It was assumed that the deformation of the system would mainly from the spring in the load cell and the compliance of the screw-nut connections, considering the Young's modulus of the trabecular block was hundreds of megapascals. However, no quantitative measurement of material property of the trabecular bone was conducted. Besides, no repeated measurement was done using different trabecular blocks to investigate the potential influence. As a result, this is considered as a limitation during the system stiffness calculation, and should serve as a reminder for conducting similar test in the future.

The load cell chosen in the shearing tests in the current study had a measuring capacity of 500 lb. ($\pm 2223\text{N}$), which was much larger than the measured ultimate shear force (130 N) of the specimens. Ideally a load cell with a range under 300N would be preferred. However, the one chosen was a dummy load cell with the lowest measuring capacity available at the time of test preparation. This might affect the accuracy of the shearing test results. The accuracy of the load

cell readings could be reduced, although the dummy load cell was calibrated prior to the shearing tests.

The failure modes of the specimens after the tests were observed by visual examination and digital images. Since SEM or histologic section analysis was not conducted in this study, a remark is made that the failure modes mentioned previously in Section 6.2.1 was based merely on limited evidences collected during the current experimental study.

GP FE modeling

A generic specimen FE model was used in the GP material optimizations. In this FE model, the GP interface was modeled as a flat plane. This was an average and approximation of currently available specimens after qualitative and quantitative screenings. The microstructures, such as the undulations in micro-meter levels, have been taken into account as a portion of the mechanical strength of the GP material. Other macrostructures, such as the inclination angle and wavy interface of the GP in a specimen were ignored, assuming the degree of freedom in the specimen's longitudinal axis could compensate most of these effects. Such an approximation would be one limitation of the current material modeling. Ideally, if the sample size is very large and the screening criterion of irregular structure could be set more strictly, or the specimen dimension could be further reduced using advanced cutting technology, the influences of the macro-structure could be minimized.

In the GP material modeling, the material failure criterion was not available for an arbitrary loading condition, because of the limited capability of predicting the failure by using the current

material models in LS-DYNA. The sub-routine method could be used to develop the advanced material failure criteria.

Additionally, it is valuable to investigate the GP damage progress and the fractures of the surrounding bones. This study requires high-definition of local geometry and accurate material property. In the microscopic scale, a GP consists of several layers with different properties. When the GP damage progress becomes the research focus, the inhomogeneous mechanical behaviors through the various layers should be a concern, and the detailed modeling of different layers would be demanded. A multi-scale FE modeling strategy could be implemented to address the excessive computation expense issue. Similar study could be found in Farzaneh et al. (2014). Inhomogeneous material modeling and microstructure of the trabecular bones will also be challenging.

When embedding the GPs to the PLEX model, the geometries of the triradiate cartilage, and the GPs at the greater trochanter, distal femur and proximal tibia did not directly refer to accurate clinical images, as in the modeling of the femoral head GP. In the next stage of CHARM-10 improvement, more efforts are needed to improve the geometric representation of the GPs. Besides, the finalized updated model will be subject to a new round of validations at various levels.

8.2. FUTURE WORK

Optimization improvement

Current optimization strategy could be further improved to achieve better overall curve matching. One improvement is to lower the weight of the shearing in the objective function. In current evenly-weighting strategy, the curve matching under tensile loading conditions was not as

good as that under shearing (as previously shown in Figure 7-4 and Figure 7-6). A larger weight of tension may lead to a better curve matching for tension, without significantly affecting the performance in shearing. An appropriate weighting ratio needs to be further studied to achieve an acceptable balance between the performances in the tension and shearing loading conditions. Another improvement can be made to perform extra low-speed and high-speed optimizations for tension and shearing, respectively. After the optimizations in the current strategy, the hyperelastic parameters and viscosity parameters could be used to an extra optimization problem including low-speed and high-speed tension. New ranges of variables should be determined accordingly. In this means, the curve matching in the high-speed could be further improved by changing the hyperelastic parameters. A similar improvement can be achieved for shearing by conducting an extra optimization including low-speed and high-speed shearing.

Age effect on the GP material and structure

The test results were used to estimate the GP material for children only around 10 YO in the current study. It would be of great interest to investigate the relationship between the GP properties and the age (or maturity level). An experimental study involving piglets from different age group could be designed to investigate the material property changes caused by the age. Additional geometric study would be also required to examine the dimension and shape changes. With such in-depth knowledge, the material correlation results and the modeling technique in current study could be broadly implemented into the GPs of children in other age groups.

Simulation of different types of GP fractures

It is also valuable to investigate the GP damage progress and the fractures of the surrounding bones as previously shown in Figure 2-7, as the fracture involving GP could be classified into five different categories by Salter and Harris (1963). Although the GPs have been included in the current updated CHARM-10 model, it is not capable of simulating these complicated modes of fracture. To improve this prediction capability in the future study, following information would be required: high-definition local geometry, accurate material properties of the cortical and trabecular bones, as well as the GPs, and the failure criteria of these bony structures and the GPs. If necessary, the layered structure of a GP would also be modeled. A multi-scale FE modeling strategy could be implemented to solve the excessive computation expense issue. Similar study could be found in Farzaneh et al. (2014). With these advanced modeling techniques, the accurate stress distribution and crack propagation could be simulated.

Continuous improvement of the biofidelity of the human model

To further improve the model, efforts should be focused on three directions to: (1) Include pediatric volunteer tests for kinematic comparison, like the study on the kinematics of upper torso of children by Arbogast et al. (2009), (2) Reconstruct the traffic accidents involving pediatric pedestrians for injury outcome comparison, such as the preliminary studies by Zhu et al. (2015) and Li et al. (2017), (3) Further implement the adult PMHS data with the help of improved scaling laws, such as the explorations done by Shen et al. (2015b). These three directions, combined with

the reasonable GP modeling technique discussed in the current study, are expected judiciously to further improve the biofidelity of the child human body model.

CHAPTER 9. CONCLUSIONS

Clinical images were implemented to build an average 10 YO child whole-body CAD model. An anthropometric study was conducted to adjust the CAD model to accurate geometric dimensions, based on which the PLEX FE model of a 10 YO child was established. The validations of the biofidelity were conducted on component level and sub-assembly level. All the validations showed reasonable agreement with the pediatric experimental data, or scaled adult test data. In addition, the PLEX was integrated with the other body parts to form a whole-body model, named as CHARM-10. A sedan-to-pedestrian impact was simulated using this model to verify its responses. The simulation results showed reasonable agreements with those from the MADYMO simulation. Therefore, the PLEX model was treated as limitedly validated and can be used for further applications and model improvement.

To further include the GPs in the PLEX FE model, tensile and shearing tests were conducted by using 20 WO porcine specimens. Among all specimens harvested from four 20 WO piglets, 65 specimens were included in the tensile tests and 48 specimens in the shearing tests. Three levels of strain rates for tensile tests (0.0053 to 1.907 s^{-1}) and for shearing tests (0.0085 to 3.037 s^{-1}) were conducted, and three anatomic regions were chosen: femoral head GP (FMR HD), distal femur GP (dist. FMR), and proximal tibia GP (prox. TBR). The majority of tension failures were in the hypertrophic zone, while most of the shearing failures happening in the hypertrophic zone as well, although a larger variation of failure modes was observed in shearing. The findings were consistent with those reported in the literature.

Randomized block ANOVA was performed to investigate the effects of strain rates and anatomic regions on the six mechanical property parameters: E , σ_{max} , ϵ_{max} and G , τ_{max} , γ_{max} . For the tensile properties, both anatomic region and strain rate were significant factors for E and σ_{max} . For the shearing properties, anatomic region was not significant for G , but significant for τ_{max} . Strain rate was significant for both G and τ_{max} . The interaction term of region and strain rate was not significant for all six property parameters. The ultimate tensile strain and shearing strain did not vary by any of the influencing factors.

Paired comparisons were conducted using Scheffe Post Hoc analysis. As for the strain rate effect, the high-rate group had higher E than the low-rate group (10.97 MPa vs. 7.12 MPa, $p=0.008$); the high-rate group had higher σ_{max} than the low-rate group (2.22 MPa vs. 1.27 MPa, $p < 0.001$) and the medium-rate group had higher σ_{max} than the low-rate group (1.84 MPa vs. 1.27 MPa, $p=0.008$); the high-rate group had higher G than the medium-rate group (3.16 MPa vs. 2.11 MPa, $p=0.006$) and the low-rate group (3.16 MPa vs. 1.68 MPa, $p=0.002$); the high-rate group had higher τ_{max} than the low-rate group (1.75 MPa vs. 1.32 MPa, $p=0.005$).

As for the anatomic region differences, FMR HD had higher E than prox. TBR (11.26 MPa vs. 7.72 MPa, $p=0.021$); FMR HD had higher σ_{max} than dist. FMR (2.40 MPa vs. 1.46 MPa, $p < 0.001$) and prox. TBR (2.40 MPa vs. 1.48 MPa, $p < 0.001$); FMR HD had higher τ_{max} than dist. FMR (1.82 MPa vs. 1.28 MPa, $p=0.001$) and prox. TBR (1.82 MPa vs. 1.44 MPa, $p=0.017$). Based on results of these comparisons, the distal femur and proximal tibia GPs were grouped together.

The 10 YO human-20 WO porcine GP correlation was done and the optimal conversion factor was determined to be 0.5234 as to minimize an overall error for the tensile properties. Based on this scaling factor, the tensile and shear stress-strain curves at 10 YO human femoral head and knee GPs were estimated using the porcine experimental data. The curves were plotted and discretized at different strain rates, and these data were taken for the following material modeling.

A transversely isotropic hyperelastic material model (MAT_92 in LS-DYNA) was chosen for the material modeling of GP. Through two stages of material optimization, the hyperelastic parameters of MAT_92 and the viscosity parameters were optimized, for both 10 YO femoral head GP and knee GPs. A good match for the shearing properties in all strain rates has been achieved between the stress-strain curves using the newly-obtained material and those estimated for 10 YO in Chapter 6. The tensile properties showed good matching at the low and medium strain rates and acceptable at the high strain rate in this experimental study.

A detailed sub-model of the proximal femur region was established, including the geometric data of GPs from CT scans. The femoral head anterior-posterior shearing was simulated to mimic the experiments conducted on human subjects as reported by Chung et al. (1976). A reasonable agreement was achieved in the parametric study, so the GP modeling techniques implemented in the sub-model should be considered as good preliminary references for future GP modeling studies.

As an application for pedestrian simulation, other GPs in the PLEX were then modeled in the similar means as the proximal femur sub-model. All the unfused GPs in the PLEX were included in the updated PLEX model and further whole-body 10 YO pedestrian FE model. An SUV-to-

pedestrian impact scenario was simulated at an impact speed of 5.0 m/s. The stress and strain distribution analysis revealed that the presence of GPs in the PLEX would change the stress distribution in terms of both peaks and timing. The deformation analysis on the elements suggested that the knee GPs would have failed due to the tension strains along the material axes, and the failure would start from the medial side of a GP. The GPs in the proximal femur showed lower risk of failure. Once a failure of GP happened, the stress distribution would be dramatically changed, and the failures at long bones might be avoided.

REFERENCES

- Anderson, A.E., Peters, C.L., Tuttle, B.D., Weiss, J.A., 2005. Subject-specific finite element model of the pelvis: development, validation and sensitivity studies. *Journal of biomechanical engineering*, 127(3), 364-373.
- Arbogast, K.B., Balasubramanian, S., Seacrist, T., Maltese, M.R., Garcia-Espana, J.F., Hopely, T., Constans, E., López-Valdés, F.J., Kent, R.W., Tanji, H., 2009. Comparison of kinematic responses of the head and spine for children and adults in low-speed frontal sled tests. *Stapp Car Crash Journal*, 53, 329-372.
- Asang, E., Posch, P., Engelbrecht, R., 1969. Experimentelle Untersuchungen über die Bruchfestigkeit des menschlichen Schienbeins. *Monatsschr Unfallheilkd Versicher Versorg Verkehrsmed*, 72(8), 336-344.
- Asang, E., Wittmann, G., Hopp, H., Watzinger, P., 1973. Experimentelle und praktische Biomechanik des menschlichen Beins. *Medizinische Welt*, 24(15), 576-581.
- Bechtel, R., 2001. Physical characteristics of the axial interosseous ligament of the human sacroiliac joint. *The Spine Journal*, 1(4), 255-259.
- Bose, D., Bhalla, K., Rooij, L., Millington, S., Studley, A., Crandall, J., 2004. Response of the Knee Joint to the Pedestrian Impact Loading Environment. *SAE Technical Paper* (No. 2004-01-1608).

- Bright, R.W., Burstein, A.H., Elmore, S.M., 1974. Epiphyseal-plate cartilage. *The Journal of Bone & Joint Surgery*, 56(4), 688-703.
- Bucholz, R., Ezaki, M., Ogden, J., 1982. Injury to the acetabular triradiate physeal cartilage. *The Journal of Bone & Joint Surgery*, 64(4), 600-609.
- Caine, D., DiFiori, J., Maffulli, N., 2006. Physeal injuries in children's and youth sports: reasons for concern? *British journal of sports medicine*, 40(9), 749-760.
- CDC. 1999-2013 Fatal Injury Data of WISQARS (Web-based Injury Statistics Query and Reporting System) of Centers for Disease Control and Prevention (accessed April 2015).
- Celarek, A., Fischerauer, S., Weinberg, A., Tschegg, E., 2014. Fracture patterns of the growth plate and surrounding bone in the ovine knee joint at different ages. *Journal of the mechanical behavior of biomedical materials*, 29, 286-294.
- Chidester, A.B., Isenberg, R.A., 2001. Final report: The pedestrian crash data study. *Proceedings of the 17th International Technical Conference on the Enhanced Safety of Vehicles (ESV)* (No. 248). Amsterdam, the Netherland.
- Choi, H.Y., Sah, S.J., Lee, B., Cho, H.S., Kang, S.J., Mun, M.S., Lee, I., Lee, J., 2005. Experimental and numerical studies of muscular activations of bracing occupant. *Proceedings of the 19th International Technical Conference on the Enhanced Safety of Vehicles (ESV)* (No. 05-0139). Washington DC, USA.
- Chung, S.M., Batterman, S.C., Brighton, C.T., 1976. Shear strength of the human femoral capital epiphyseal plate. *Journal of Bone and Joint Surgery*, 58(1), 94-103.

- Cohen, B., Chorney, G.S., Phillips, D.P., Dick, H.M., Buckwalter, J.A., Ratcliffe, A., Mow, V.C., 1992. The microstructural tensile properties and biochemical composition of the bovine distal femoral growth plate. *Journal of Orthopaedic Research*, 10(2), 263-275.
- Cohen, B., Chorney, G.S., Phillips, D.P., Dick, H.M., Mow, V.C., 1994. Compressive stress-relaxation behavior of bovine growth plate may be described by the nonlinear biphasic theory. *Journal of Orthopaedic Research*, 12(6), 804-813.
- Cohen, B., Lai, W.M., Mow, V.C., 1998. A transversely isotropic biphasic model for unconfined compression of growth plate and chondroepiphysis. *Journal of biomechanical engineering*, 120(4), 491-496.
- Demetriades, D., Murray, J., Martin, M., Velmahos, G., Salim, A., Alo, K., Rhee, P., 2004. Pedestrians injured by automobiles: relationship of age to injury type and severity. *Journal of the American College of Surgeons*, 199(3), 382-387.
- DiMaggio, C., Durkin, M., 2002. Child pedestrian injury in an urban setting descriptive epidemiology. *Academic emergency medicine*, 9(1), 54-62.
- Dong, L., Li, G., Mao, H., Marek, S., Yang, K.H., 2013. Development and validation of a 10-year-old child ligamentous cervical spine finite element model. *Annals of biomedical engineering*, 41(12), 2538-2352.
- EEVC, 1998. EEVC Working Group 17 Report. Improved Test Methods to Evaluate Pedestrian Protection Afforded by Passenger Cars, in: Committee, E.E.V.-s. (Ed.).
- Esteco, S., 2014. ModeFRONTIER 2014 User's Manual.

- Farzaneh, S., Pasetta, O., Gómez-Benito, M., 2014. Multi-scale finite element model of growth plate damage during the development of slipped capital femoral epiphysis. *Biomechanics and modeling in mechanobiology*, 1-15.
- Fildes, B., Gabler, H., Otte, D., Linder, A., 2004. Pedestrian impact priorities using real-world crash data and harm. *Proceedings of International Research Council on Biomechanics of Injury*. Graz, Austria.
- Fishkin, Z., Armstrong, D.G., Shah, H., Patra, A., Mihalko, W.M., 2006. Proximal femoral physis shear in slipped capital femoral epiphysis-a finite element study. *Journal of Pediatric Orthopaedics*, 26(3), 291-294.
- Flynn, J.M., Skaggs, D.L., Waters, P.M., 2014. *Rockwood and Wilkins' Fractures in Children*, 8th ed. Lippincott Williams & Wilkins.
- Franklyn, M., Peiris, S., Huber, C., Yang, K.H., 2007. Pediatric material properties: a review of human child and animal surrogates. *Critical Reviews™ in Biomedical Engineering*, 35(3-4), 197-342.
- Froimson, M.I., Ratcliffe, A., Gardner, T.R., Mow, V.C., 1997. Differences in patellofemoral joint cartilage material properties and their significance to the etiology of cartilage surface fibrillation. *Osteoarthritis and cartilage / OARS, Osteoarthritis Research Society*, 5(6), 377-386.

- Fujii, T., Takai, S., Arai, Y., Kim, W., Amiel, D., Hirasawa, Y., 2000. Microstructural properties of the distal growth plate of the rabbit radius and ulna: biomechanical, biochemical, and morphological studies. *Journal of Orthopaedic Research*, 18(1), 87-93.
- Gómez-Benito, M., Moreo, P., Pérez, M., Paseta, O., García-Aznar, J., Barrios, C., Doblaré, M., 2007. A damage model for the growth plate: application to the prediction of slipped capital epiphysis. *Journal of biomechanics*, 40(15), 3305-3313.
- Goulding, A., Gold, E., Cannan, R., Williams, S., Lewis-Barned, N.J., 1996. Changing femoral geometry in growing girls: a cross-sectional DEXA study. *Bone*, 19(6), 645-649.
- Guillemot, H., Besnault, B., Robin, S., Got, C., Le Coz, J., Lavaste, F., Lassau, J.-P., 1997. Pelvis Injuries in Side Impact Collisions : A Field Accident Analysis and Dynamic Tests on Isolated Pelvis Bones. SAE Technical Paper (No. 973322).
- Guse, R.J., Connolly, J.F., Alberts, R., Lippiello, L., 1989. Effect of aging on tensile mechanical properties of the rabbit distal femoral growth plate. *Journal of Orthopaedic Research*, 7(5), 667-673.
- Hallquist, J.O., 2007. LS-DYNA keyword user's manual. Livermore Software Technology Corporation, 970.
- Heeg, M., Visser, J., Oostvogel, H., 1988. Injuries of the acetabular triradiate cartilage and sacroiliac joint. *Journal of Bone & Joint Surgery, British Volume*, 70(1), 34-37.
- Hewitt, J., Guilak, F., Glisson, R., Vail, T.P., 2001. Regional material properties of the human hip joint capsule ligaments. *Journal of Orthopaedic Research*, 19(3), 359-364.

Humanetics. Q-Series Child Dummies. <http://www.humaneticsatd.com/crash-test-dummies/children/q-series> (accessed, March 2014).

Irwin, A.L., Mertz, H.J., 1997. Biomechanical basis for the CRABI and Hybrid III child dummies. SAE Technical Paper (No. 973317).

Irwin, A.L., Mertz, H.J., Elhagediab, A.M., Moss, S., 2002. Guidelines for assessing the biofidelity of side impact dummies of various sizes and ages. *Stapp Car Crash Journal*, 46, 297-319.

Ito, O., Okamoto, M., Takahashi, Y., Mori, F., 2009. Validation of an FE Lower Limb Model for a Child Pedestrian by Means of Accident Reconstruction. *SAE International Journal of Passenger Cars-Mechanical Systems*, 1(1), 971-984.

Ivarsson, B.J., Crandall, J.R., Longhitano, D., Okamoto, M., 2004. Lateral Injury Criteria for the 6-year-old Pedestrian-Part II: Criteria for the Upper and Lower Extremities. SAE Technical Paper (No. 2004-01-1755).

Ivarsson, B.J., Crandall, J.R., Okamoto, M., 2006. Influence of age-related stature on the frequency of body region injury and overall injury severity in child pedestrian casualties. *Traffic injury prevention*, 7(3), 290-298.

Iwamoto, M., Nakahira, Y., Tamura, A., Kimpara, H., Watanabe, I., Miki, K., 2007. Development of advanced human models in THUMS. Proc. 6th European LS-DYNA Users' Conference. Gothenburg, Sweden.

- Jarrett, K., Saul, R., 1998. Pedestrian injury-analysis of the PCDS field collision data. Proceedings of the 16th International Technical Conference on the Enhanced Safety of Vehicles (ESV) (No. 98-S6-O-04). Windsor, Ontario, CA.
- Jebaseelan, D.D., Jebaraj, C., Yoganandan, N., Rajasekaran, S., 2010. Validation efforts and flexibilities of an eight-year-old human juvenile lumbar spine using a three-dimensional finite element model. *Medical & biological engineering & computing*, 48(12), 1223-1231.
- Jiang, B., Cao, L., Mao, H., Wagner, C., Marek, S., Yang, K.H., 2014. Development of a 10-year-old paediatric thorax finite element model validated against cardiopulmonary resuscitation data. *Computer methods in biomechanics and biomedical engineering*, 17(11), 1185-1197.
- Jin, X., 2009. Biomechanical response and constitutive modeling of bovine pia-arachnoid complex. Doctoral dissertation, Wayne State University.
- Kalra, A., Gupta, V., Shen, M., Jin, X., Chou, C.C., Yang, K.H., 2016. Pedestrian safety: an overview of physical test surrogates, numerical models and availability of cadaveric data for model validation. *International Journal of Vehicle Safety*, 9(1), 39-71.
- Kandzierski, G., Matuszewski, L., Wojcik, A., 2012. Shape of growth plate of proximal femur in children and its significance in the aetiology of slipped capital femoral epiphysis. *International orthopaedics*, 36(12), 2513-2520.
- Kerrigan, J.R., Drinkwater, D.C., Kam, C.Y., Murphy, D.B., Ivarsson, B.J., Crandall, J.R., Patrie, J., 2004. Tolerance of the human leg and thigh in dynamic latero-medial bending. *Int J Crashworthines*, 9(6), 607-623.

- Kikuchi, Y., Takahashi, Y., Mori, F., 2006. Development of a finite element model for a pedestrian pelvis and lower limb. SAE Technical Paper (No. 2006-01-0683).
- Kikuchi, Y., Takahashi, Y., Mori, F., 2008. Full-scale validation of a human FE model for the pelvis and lower limb of a pedestrian. SAE Technical Paper (No. 2008-01-1243).
- Kim, J.E., Hsieh, M.H., Soni, B.K., Zayzafoon, M., Allison, D.B., 2013. Childhood Obesity as a Risk Factor for Bone Fracture: A mechanistic study. *Obesity*, 21(7), 1459-1466.
- Kim, J.E., Li, Z., Ito, Y., Huber, C.D., Shih, A.M., Eberhardt, A.W., Yang, K.H., King, A.I., Soni, B.K., 2009. Finite element model development of a child pelvis with optimization-based material identification. *Journal of biomechanics*, 42(13), 2191-2195.
- Kishida, H., Uesugi, M., 1987. Tests of the interface between sand and steel in the simple shear apparatus. *Geotechnique*, 37(1), 45-52.
- Konosu, A., Ishikawa, H., Tanahashi, M., 2001. Reconsideration of Injury Criteria for Pedestrian Subsystem Legform Test—Problems of Rigid Legform Impactor. Proceedings of the 17th International Technical Conference on the Enhanced Safety of Vehicles (ESV) (No. 01-S8-O-263). Amsterdam, the Netherland.
- Konz, R.J., Goel, V.K., Grobler, L.J., Grosland, N.M., Spratt, K.F., Scifert, J.L., Sairyo, K., 2001. The pathomechanism of spondylolytic spondylolisthesis in immature primate lumbar spines: in vitro and finite element assessments. *Spine*, 26(4), E38-E49.

- Lee, K.E., Pelker, R.R., Rudicel, S.A., Ogden, J.A., Panjabi, M.M., 1985. Histologic patterns of capital femoral growth plate fracture in the rabbit: the effect of shear direction. *Journal of Pediatric Orthopaedics*, 5(1), 32-39.
- Li, H., Jin, X., Zhao, H., Cui, S., Jiang, B., Yang, K.H., 2017. Reconstruction of Pediatric Occupant Kinematic Responses Using Finite Element Method in a Real-World Lateral Impact. *SAE Technical Paper* (2017-01-1462).
- Li, Z., Alonso, J.E., Kim, J.E., Davidson, J.S., Etheridge, B.S., Eberhardt, A.W., 2006. Three-dimensional finite element models of the human pubic symphysis with viscohyperelastic soft tissues. *Annals of biomedical engineering*, 34(9), 1452-1462.
- Li, Z., Kim, J.-E., Davidson, J.S., Etheridge, B.S., Alonso, J.E., Eberhardt, A.W., 2007. Biomechanical response of the pubic symphysis in lateral pelvic impacts: a finite element study. *Journal of biomechanics*, 40(12), 2758-2766.
- Liu, X., Yang, J., 2002. Development of child pedestrian mathematical models and evaluation with accident reconstruction. *Traffic injury prevention*, 3(4), 321-329.
- Maeno, T., Hasegawa, J., 2001. Development of a finite element model of the total human model for safety (THUMS) and application to car-pedestrian impacts. *Proceedings of the 17th international Technical Conference on the Enhanced Safety of Vehicles (ESV) (No. 494)*. Amsterdam, the Netherland.

Mao, H., Holcombe, S., Shen, M., Jin, X., Wagner, C.D., Wang, S.C., Yang, K.H., King, A.I., 2014.

Development of a 10-Year-Old Full Body Geometric Dataset for Computational Modeling.

Annals of biomedical engineering, 42(10), 2143-2155.

Mao, H., Yang, K.H., 2011. Investigation of brain contusion mechanism and threshold by

combining finite element analysis with in vivo histology data. International Journal for

Numerical Methods in Biomedical Engineering, 27(3), 357-366.

Matsui, Y., Ishikawa, H., Sasaki, A., Kajzer, J., Schroeder, G., 1999. Impact response and

biofidelity of pedestrian legform impactors. Proceedings of the International Research

Council on the Biomechanics of Injury conference (IRCOBI). Sitges, Spain.

Mertz, H.J., Jarrett, K., Moss, S., Salloum, M., Zhao, Y., 2001. The Hybrid III 10-Year-Old Dummy.

Stapp Car Crash Journal, 45, 319-328.

Mizuno, K., Iwata, K., Deguchi, T., Ikami, T., Kubota, M., 2005. Development of a three-year-old

child FE model. Traffic injury prevention, 6(4), 361-371.

Mizuno, Y., Ishikawa, H., 2005. Summary of IHRA pedestrian safety WG activities-proposed test

methods to evaluate pedestrian protection afforded by passenger cars. Proceedings of the

19th International Technical Conference on the Enhanced Safety of Vehicles (ESV) (No.

05-0138). Washington DC, US.

Moen, C.T., Pelker, R.R., 1984. Biomechanical and histological correlations in growth plate failure.

Journal of Pediatric Orthopaedics, 4(2), 180-184.

Moore, K.L., Agur, A.M.R., Dalley, A.F., 2011. Essential clinical anatomy, 4th ed. Lippincott Williams & Wilkins, Baltimore, MD.

NHTSA, 2013. Traffic Safety Facts 2011 data - Children. Government Report (DOT HS 811 767). Washington, DC.

NHTSA, 2014. Traffic Safety Facts 2012 data - Pedestrian. Government Report (DOT HS 811 888). Washington, DC.

Noble, J., Diamond, R., Stirrat, C., Sledge, C., 1982. Breaking force of the rabbit growth plate and its application to epiphyseal distraction. *Acta Orthopaedica*, 53(1), 13-16.

Ogden, J.A., 2000. *Skeletal injury in the child*, 3rd ed. Springer, New York.

Okamoto, M., Takahashi, Y., Mori, F., Hitosugi, M., Madeley, J., Ivarsson, J., Crandall, J.R., 2003. Development of finite element model for child pedestrian protection. Proceedings of the 18th International Technical Conference on the Enhanced Safety of Vehicles (ESV) (No. 151). Nagoya, Japan.

Ouyang, J., Zhu, Q., Zhao, W., 2003a. Biomechanical character of extremity long bones in children and its significance. *Chinese Journal of Clinical Anatomy*, 21(6), 620-623.

Ouyang, J., Zhu, Q., Zhao, W., Xu, Y., Chen, W., Zhong, S., 2003b. Experimental cadaveric study of lateral impact of the pelvis in children. *Academic Journal of the First Medical College of PLA*, 23(5), 397-401, 408.

- Pailler-Mattei, C., Bec, S., Zahouani, H., 2008. In vivo measurements of the elastic mechanical properties of human skin by indentation tests. *Medical engineering & physics*, 30(5), 599-606.
- Peterson, C.A., Peterson, H.A., 1972. Analysis of the incidence of injuries to the epiphyseal growth plate. *Journal of Trauma and Acute Care Surgery*, 12(4), 275-281.
- Peterson, H.A., 2007. *Epiphyseal growth plate fractures*. Springer, Heidelberg.
- Puso, M.A., Weiss, J.A., 1998. Finite element implementation of anisotropic quasi-linear viscoelasticity using a discrete spectrum approximation. *Journal of biomechanical engineering*, 120(1), 62-70.
- Ribble, T.G., Santare, M.H., Miller, F., 2001. Stresses in the growth plate of the developing proximal femur. *Journal of applied biomechanics*, 17(2), 129-141.
- Rigoni, E., 2003. Bounded BFGS. Technical Report 2003-007, Esteco.
- Roudsari, B.S., Mock, C.N., Kaufman, R., 2005. An evaluation of the association between vehicle type and the source and severity of pedestrian injuries. *Traffic injury prevention*, 6(2), 185-192.
- Sairyo, K., Goel, V.K., Masuda, A., Vishnubhotla, S., Faizan, A., Biyani, A., Ebraheim, N., Yonekura, D., Murakami, R.-I., Terai, T., 2006. Three-dimensional finite element analysis of the pediatric lumbar spine. Part I: pathomechanism of apophyseal bony ring fracture. *European Spine Journal*, 15(6), 923-929.

- Salter, R.B., Harris, W.R., 1963. Injuries involving the epiphyseal plate. *The Journal of Bone & Joint Surgery*, 45(3), 587-622.
- Scheuer, L., Black, S., Cunningham, C., 2000. *Developmental juvenile osteology*. Academic Press.
- Sergerie, K., Lacoursiere, M.O., Levesque, M., Villemure, I., 2009. Mechanical properties of the porcine growth plate and its three zones from unconfined compression tests. *Journal of biomechanics*, 42(4), 510-516.
- Serre, T., Lalys, L., Bartoli, C., Christia-Lotter, A., Leonetti, G., Brunet, C., 2010. Child pedestrian anthropometry: evaluation of potential impact points during a crash. *Accident Analysis & Prevention*, 42(6), 1943-1948.
- Shen, M., Mao, H., Jiang, B., Zhu, F., Jin, X., Dong, L., Ham, S.J., Palaniappan, P., Chou, C.C., Yang, K.H., 2016. Introduction of Two New Pediatric Finite Element Models for Pedestrian and Occupant Protections. *SAE Technical Paper (No. 2016-01-1492)*.
- Shen, M., Zhu, F., Jiang, B., Sanghavi, V., Fan, H., Cai, Y., Wang, Z., Kalra, A., Jin, X., Chou, C.C., Yang, K.H., 2015a. Development and a Limited Validation of a Whole-Body Finite Element Pedestrian and Occupant Models of a 10-Year-Old Child. *Proceedings of the International Research Council on the Biomechanics of Injury conference (IRCOBI)*. Lyon, France.
- Shen, M., Zhu, F., Mao, H., Fan, H., Mone, N., Sanghavi, V., Kalra, A., Jin, X., Chou, C.C., Yang, K.H., 2015b. Finite element modelling of 10-year-old child pelvis and lower extremities

with growth plates for pedestrian protection. *International Journal of Vehicle Safety*, 8(3), 263-286.

Silber, J.S., Flynn, J.M., 2002. Changing patterns of pediatric pelvic fractures with skeletal maturation: implications for classification and management. *Journal of Pediatric Orthopaedics*, 22(1), 22-26.

Snyder, R., Schneider, L., Owings, C., Reynolds, H., Golomb, H., Schork, A., 1977. Anthropometry of Infants, Children, and Youths to Age 18 for Product Safety Design. Final Report. Consumer Product Safety Commission Report (No. UM-HSRI-77-17). Ann Arbor Michigan.

Sylvestre, P. L., Villemure, I., Aubin, C. É., 2007. Finite element modeling of the growth plate in a detailed spine model. *Medical & biological engineering & computing*, 45(10), 977-988.

Takahashi, Y., Kikuchi, Y., 2001. Biofidelity of test devices and validity of injury criteria for evaluating knee injuries to pedestrians. *Proceedings of the 17th International Technical Conference on the Enhanced Safety of Vehicles (ESV) (No. 373)*. Amsterdam, the Netherland.

Takahashi, Y., Kikuchi, Y., Konosu, A., Ishikawa, H., 2000. Development and validation of the finite element model for the human lower limb of pedestrians. *Stapp Car Crash Journal*, 44, 335-355.

TASS International. MADYMO Utilities Manual Release 7.2. <https://www.tassinternational.com/software-support> (accessed March, 2014).

- Tschegg, E., Celarek, A., Fischerauer, S., Stanzl-Tschegg, S., Weinberg, A., 2012. Fracture properties of growth plate cartilage compared to cortical and trabecular bone in ovine femora. *Journal of the mechanical behavior of biomedical materials*, 14, 119-129.
- United Nations, 2012. Uniform provisions concerning the approval of motor vehicles with regard to their pedestrian safety performance, ECE Regulation No. 127.
- Untaroiu, C., Darvish, K., Crandall, J., Deng, B., Wang, J.T., 2005. A finite element model of the lower limb for simulating pedestrian impacts. *Stapp Car Crash Journal*, 49, 157-181.
- Untaroiu, C.D., Crandall, J.R., Takahashi, Y., Okamoto, M., Ito, O., Fredriksson, R., 2010. Analysis of running child pedestrians impacted by a vehicle using rigid-body models and optimization techniques. *Safety Science*, 48(2), 259-267.
- Untaroiu, C.D., Yue, N., Shin, J., 2013. A finite element model of the lower limb for simulating automotive impacts. *Annals of biomedical engineering*, 41(3), 513-526.
- Van Rooij, L., Bhalla, K., Meissner, M., Ivarsson, J., Crandall, J., Longhitano, D., Takahashi, Y., Dokko, Y., Kikuchi, Y., 2003. Pedestrian crash reconstruction using multi-body modeling with geometrically detailed, validated vehicle models and advanced pedestrian injury criteria. *Proceedings of the 18th International Technical Conference on the Enhanced Safety of Vehicles (ESV) (No. 468)*. Nagoya, Japan.
- Van Rooij, L., Meissner, M., Bhalla, K., Crandall, J., Takahashi, Y., Dokko, Y., Kikuchi, Y., 2004. A comparative evaluation of pedestrian kinematics and injury prediction for adults and children upon impact with a passenger car. *SAE Technical Paper (No. 2004-01-1606)*.

- Villemure, I., Stokes, I.A., 2009. Growth plate mechanics and mechanobiology. A survey of present understanding. *Journal of biomechanics*, 42(12), 1793-1803.
- Volgyi, E., Tylavsky, F.A., Xu, L., Lu, J., Wang, Q., Alen, M., Cheng, S., 2010. Bone and body segment lengthening and widening: a 7-year follow-up study in pubertal girls. *Bone*, 47(4), 773-782.
- Von Heyden, J., Hauschild, O., Strohm, P.C., Stuby, F., Südkamp, N.P., Schmal, H., 2012. Paediatric acetabular fractures. *Acta Orthopædica Belgica*, 78, 611-618.
- Wazana, A., Krueger, P., Raina, P., Chambers, L., 1997. A review of risk factors for child pedestrian injuries: are they modifiable? *Injury Prevention*, 3(4), 295-304.
- WHO, 2008. World report on child injury prevention. World Health Organization, Geneva.
- Williams, J.L., Do, P.D., Eick, J.D., Schmidt, T.L., 2001. Tensile properties of the physis vary with anatomic location, thickness, strain rate and age. *Journal of Orthopaedic Research*, 19(6), 1043-1048.
- Williams, J.L., Vani, J.N., Eick, J.D., Petersen, E.C., Schmidt, T.L., 1999. Shear strength of the physis varies with anatomic location and is a function of modulus, inclination, and thickness. *Journal of Orthopaedic Research*, 17(2), 214-222.
- Woods, W., Sherwood, C., Ivarsson, J., 2003. A review of pediatric injuries at a level I trauma center. Proceedings of the 18th International Technical Conference on the Enhanced Safety of Vehicles (ESV) (Vol. 809, p. 543). Nagoya, Japan.

- Wosu, R., Sergerie, K., Lévesque, M., Villemure, I., 2012. Mechanical properties of the porcine growth plate vary with developmental stage. *Biomechanics and modeling in mechanobiology*, 11(3-4), 303-312.
- Yao, J.F., Yang, J.K., Fredriksson, R., 2006. Reconstruction of head-to-hood impact in an automobile-to-child-pedestrian collision. *Int J Crashworthines*, 11(4), 387-395.
- Young, W.C., Budynas, R.G., 2002. *Roark's formulas for stress and strain*. McGraw-Hill New York.
- Yue, N., Shin, J., Untaroiu, C.D., 2011. Development and validation of an occupant lower limb Finite element model. SAE Technical Paper (No. 2011-01-1128).
- Zar, J.H., 2010. *Biostatistical analysis*, 5th ed. Pearson Education, Upper Saddle River, NJ.
- Zhu, F., Jiang, B., Hu, J., Wang, Y., Shen, M., Yang, K.H., 2015. Computational modeling of traffic related thoracic injury of a 10-year-old child using subject-specific modeling technique. *Annals of biomedical engineering*, 1-14.

ABSTRACT

DEVELOPMENT OF A FINITE ELEMENT PELVIS AND LOWER EXTREMITY MODEL WITH GROWTH PLATES FOR PEDIATRIC PEDESTRIAN PROTECTION

by

MING SHEN

August 2017

Advisor: Dr. King H. Yang

Major: Biomedical Engineering

Degree: Doctor of Philosophy

Finite element (FE) model is a useful tool frequently used for investigating the injury mechanisms and designing protection countermeasures. At present, no 10 years old (YO) pedestrian FE model has been developed from appropriate anthropometries and validated against limitedly available impact response data. A 10 YO child FE pelvis and lower extremities (PLEX) model was established to fill the gap of lacking such models in this age group. The baseline model was validated against available pediatric postmortem human subjects (PMHS) test data and additional scaled adult data, then the PLEX model was integrated to build a whole-body FE model representing a 10 YO pedestrian.

Additional investigations revealed that the immature tissues, growth plates (GPs), should be explicitly modeled because they have different mechanical properties than the surrounding bones.

Epidemiological data revealed that GP accounted for a large portion of pediatric fractures. To investigate the GP's material property for further advancement of the baseline PLEX FE model for simulating impact mechanical responses, a series of tensile and shearing experiments on porcine bone-GP-bone units were carried out. The GPs from the femoral head, distal femur, and proximal tibia of 20-weeks-old piglets were tested, under different strain rates. Randomized block ANOVA was conducted to determine the effects of anatomic region and strain rate on the material properties of GPs. By comparing the porcine experimental data to the limited data obtained from tests on human subjects reported in the literature, an optimal conversion factor was derived to correlate the material properties of 20-week-old piglet GPs and 10 YO child GPs.

A transversely isotropic hyperelastic material model (MAT_92 available in LS-DYNA) with added viscosity was adopted to mimic the GP tissues. After a series of optimization procedures, the material parameter sets needed for MAT_92 were determined to represent the GPs of a 10 YO child. To further explore the GP modeling techniques, a sub-model representing the proximal femur was extracted from the PLEX model. The femoral head GP in the sub-model was modeled using the geometry from CT scans and the material properties from early optimizations. FE simulations of femoral head shearing were conducted on the sub-model to determine other GP modeling settings. In the following technical application, similar GP modeling techniques were implemented to model the GPs at the hip and knee regions to update the baseline PLEX model, and further the whole-body model. An SUV-to-pedestrian impact scenario was simulated using the

updated whole-body model, the remarkable influences of the GPs on the stress distributions in the PLEX were quantitatively assessed.

AUTOBIOGRAPHICAL STATEMENT

MING SHEN

EDUCATION:

Ph.D.	Biomedical Engineering Wayne State University, Detroit, Michigan	2017
M.S.	Automotive System Engineering, RWTH Aachen, Germany	2007
M.S.	Mechanical Engineering, Tsinghua University, Beijing, China	2007
B.S.	Automotive Engineering, Tsinghua University, Beijing, China	2003

ACADEMIC HONORS:

Best Student Paper Awards of Stapp Car Crash Conference (co-author)	2015
Graduate Professional Travel Award	2015
Kales Endowed Scholars Fund	2014
Rumble Fellowship	2012

SELECTED PUBLICATIONS:

- Shen, M., Zhu, F., Mao, H., Fan, H., Mone, N., Sanghavi, V., Kalra, A., Jin, X., Chou, C. C. and Yang, K. H., 2015. Finite element modelling of 10-year-old child pelvis and lower extremities with growth plates for pedestrian protection. *International journal of vehicle safety*, 8(3), 263-286.
- Shen, M., Zhu, F., Jiang, B., Sanghavi, V., Fan, H., Cai, Y., Wang, Z., Kalra, A., Jin, X., and Chou, C. C. and Yang, K. H., 2015. Development and a limited validation of a whole-body finite element pedestrian and occupant models of a 10-year-old child. In *International Research Council on Biomechanics of Injury (IRCOBI)*. Lyon, France.
- Shen, M., Mao, H., Jiang, B., Zhu, F., Jin, X., Dong, L., Ham, S. J., Palaniappan, P. Chou, C. C. and Yang, K. H., 2016. *Introduction of Two New Pediatric Finite Element Models for Pedestrian and Occupant Protections*. SAE Technical Paper (No. 2016-01-1492).